SUPPRESSING THE NONRECIPROCAL ERRORS IN A FIBER OPTIC ROTATION SENSOR

A DISSERTATION SUBMITTED TO

THE GRADUATE SCHOOL OF ENGINEERING AND SCIENCE

OF BILKENT UNIVERSITY

IN PARTIAL FULFILLMENT OF THE REQUIREMENTS FOR

THE DEGREE OF

DOCTOR OF PHILOSOPHY

IN

PHYSICS

By

Tuğba Andaç

February 2024

SUPPRESSING THE NONRECIPROCAL ERRORS IN A FIBER OPTIC ROTATION SENSOR

By Tuğba Andaç

February 2024

We certify that we have read this dissertation and that in our opinion it is fully adequate, in scope and in quality, as a dissertation for the degree of Doctor of Philosophy.

Ekmel Özbay(Advisor)

Engin Durgun

Onur Tokel

Alpan Bek

İbrahim Tuna Özdür

Approved for the Graduate School of Engineering and Science:

Orhan Arıkan
Director of the Graduate School

ABSTRACT

SUPPRESSING THE NONRECIPROCAL ERRORS IN A FIBER OPTIC ROTATION SENSOR

Tuğba Andaç
Ph.D. in Physics
Advisor: Ekmel Özbay
February 2024

Among several other types of rotation sensors, interferometric fiber optic gyroscopes (IFOGs) shine out as they provide longer lifetime, quicker turn-on time, higher reliability, precision, and sensitivity. However, the fact that any environmental effects distorting the counter-propagating beams from travelling the identical path in a rotating loop induce phase differences apart from the Sagnac effect and cause error leaves them as an application which still needs to be improved. Therefore, we will start by paving the way with the studies we have conducted on the light source for improving its wavelength stability against temperature, and then we will steer our studies toward improving the quality of the fiber optic coil. Although IFOGs being a worldwide hot topic, most of the studies have been carried out by using quadrupole winding pattern, while only little is known when it comes to other winding patterns. Use of hexadecapole winding pattern paints a more promising picture and opens new doors in this research line. Being in the quest of finding a way to improve the performance of these sensors against such disturbing effects, we study and explore the thermal behaviours of the IFOGs built with fiber coils having different winding patterns. We demonstrate that the use of hexadecapole winding pattern overtowers the other winding patterns namely dipole, quadrupole, and octupole in the need of trimming as it presents lower absolute rate error; not only at a certain rate of temperature change but also under different rate of temperature changes. Moreover, we enrich our studies by further investigating the thermal behavior of these sensors, show the independency of Shupe effect in the direction of real rotation, and propose a novel method which eliminates the significance of the symmetry in fiber coil winding. We support our experimental findings with the simulations as well.

Keywords: bias error, fiber optic sensor, gyroscope, interferometry, nonreciprocity, Shupe, suppression, thermal.

ÖZET

BİR FİBER OPTİK DÖNÜ SENSÖRÜNDEKİ KARŞILIKSIZ HATALARIN BASTIRILMASI

Tuğba Andaç
Fizik, Doktora
Tez Danışmanı: Ekmel Özbay
Şubat 2024

İnterferometrik fiber optik dönüölçerler (İFODlar), daha uzun ömür, daha hızlı açılma süresi, daha yüksek güvenilirlik, kesinlik ve hassasiyet sundukları için diğer bir çok dönme sensöründen daha ön plandadır. Ancak karşılıklı hareket eden ışınların dönen bir döngüde aynı yolu izlemesini bozan herhangi bir çevresel etkinin, Sagnac etkisi dışında faz farklılıklarına neden olarak hata yaratması, bu dönüölçerlerin hâlâ geliştirilmesi gerektiğini göstermektedir. Bu sebeple, çalışmalarımıza kullanılan ışık kaynağının sıcaklığa bağlı dalgaboyu kararlılığını iyileştirme ile zemin hazırlayarak başlıyor ve daha sonra çalışmalarımızı fiber sarımın kalitesini arttırmaya doğru yönlendiriyoruz. İnterferometrik fiber optik dönüölçerler, dünya çapında popüler bir konu olmasına rağmen, haklarında yapılan çalışmaların çoğu dörtlü sarım modeli kullanılarak yürütülmekte ve diğer sarım modelleri konusunda daha az şey bilinmektedir. Burda onaltılı sarım modelinin kullanımı daha umut verici bir tablo çizmekte ve bu araştırma konusunda yeni kapılar açmaktadır. Bu tür rahatsız edici etkilere karşı bu sensörlerin performansını artırmanın bir yolunu bulma arayışı içinde, farklı sarım desenlerine sahip fiber sarımlarla oluşturulan dönüölçerlerin termal davranışlarını inceliyor ve araştırıyoruz. Onaltılı sarım modelinin kullanımının sadece belirli bir sıcaklık değişimi hızında değil, aynı zamanda farklı sıcaklık değişim hızlarında da, daha düşük mutlak oran hatası sunması sebebiyle, düzeltme ihtiyacında ikili, dörtlü ve sekizli sarım modellerini gölgede bıraktığını gösteriyoruz. Ayrıca, bu sensörlerin termal davranışlarını daha fazla araştırarak çalışmalarımızı zenginleştiriyor, Shupe etkisinin gerçek dönme yönünde bağımsızlığını gösteriyoruz ve fiber sarım deseninde simetrinin önemini ortadan kaldıran yeni bir yöntem öneriyoruz. Deneysel bulgularımızı simülasyonlarla da destekliyoruz.

Anahtar sözcükler: sabit kayma hatası, fiber optik sensör, dönüölçer, interferometri, karşılıklı olmama, Shupe, bastırma, termal.

Acknowledgement

To my five-year-old self...

Contents

List of Figures

Chapter 1

Introduction

'How would I go from a point to another?' is one of the most common questions of human beings since the beginning of history. We have come a long way to find answers to this so simple, yet so hard question which has formed the basis of inertial guidance and navigation. It has been a long journey, but now one can get quick and cheap answers thanks to the developments in these areas. Today, one of the easiest ways to find an answer for this question is to use global positioning system (GPS). However, GPS might not be reliable enough, because GPS signals can sometimes be jammed or even destroyed all together. Moreover, they can also be delayed or out of reach because of the physical obstructions such as tunnels or caves. That's why, it's safer to use inertial navigation systems as it is crucially important to get fast and accurate information when needed. There comes fiber optic rotation sensors, specifically interferometric fiber optic gyroscopes to the rescue. Having reached their maturity, nowadays IFOGs have become one of the most preferred inertial sensors used for navigation, guidance, control and stabilization in land, air, marine and even space, since they are used in inertial navigation systems which help to detect velocity and position without the need of GPS.

IFOGs being a worldwide hot topic, the variety of the areas that they are used in and the need for achieving higher sensitivity in performance have tempted us to study on this topic as well as the other scientists and the companies. Being aware of the fact that any environmental effects distorting the counterpropagating beams from travelling the identical path in a rotating loop induce phase differences apart from the Sagnac effect and cause error, trying to reduce these nonreciprocal errors and increasing the sensitivity of these rotation sensors will be the main aim of this thesis.

With this thesis, I mainly study the thermal nonreciprocal errors on fiber coils constructing an IFOG. After going over the review, the basic principles, and the componentry of IFOGs in the beginning of Chapter 2, basic configuration and errors sources of these rotation sensors will be introduced and explained in detail towards the end of the same chapter. Furthermore, the ways of suppressing these errors will be introduced as well.

Since we use light to calculate motion in the IFOGs, a way of constructing a thermally stable light source will be introduced in Chapter 3. The configuration of the light source and the improved test results obtained under varying temperature regarding wavelength and optical output power will be presented. Light will then be navigated further towards the fiber coil as it is in the real configuration.

Chapter 4 will explain the studies conducted in the aim of improving the quality of fiber coils constructing the IFOGs. The applications that we have already secured by patent and the ongoing patent applications will be presented here.

Then, we will pave our way towards our main experiments and simulations. By blending the information provided in the first four chapters, we will offer a new method in Chapter 5. This chapter will present the experimental study conducted on a special fiber coil and the information on it's production. Unlike most of the studies which have examined the fiber coils with quadrupole winding pattern at certain temperature rates, we will focus on investigating the thermal performance of the fiber coil with hexadecapole winding pattern at different temperature rates. Finally, we will also investigate and present the thermal performance of the same coil theoretically as well by conducting simulations in the pursuit of supporting our experimental findings. We show that how different types of fiber coil windings behave under different thermal rates and hexadecapole winding pattern outperforms dipole, quadrupole, and octupole winding patterns in the need of trimming both theoretically and experimentally even if tested under different temperature rates.

In the pursuit of richening our studies at a higher level, we stepped forward in Chapter 6 and developed a novel method for Shupe mitigation which has been also submitted to the journal of Scientific Reports. We kept on studying experimentally and theoretically on how different types of fiber coil winding methods behave under different rates of temperature change and developed a novel configured complete system.

In short, starting from the studies of the fiber optic rotation sensors, specifically IFOGs which have been developed in the light of the improvements for finding an answer to the navigation problems above, we ended up proposing a novel method that rules out the importance of the fiber optic coil winding symmetry epochally and the need of any extra treatment for the fiber coil to increase the thermal performance of the system.

Chapter 2

Review of the Interferometric Fiber Optic Gyroscopes

2.1 The Rocky Road to Building up an Interferometric Fiber Optic Gyroscope

1913 was a breakthrough in the history of the IFOGs thanks to the French scientist Georges Sagnac showing the experimental possibility of detecting rotation with respect to inertial space via a non-moving optical system for the first time. He pointed out the fact that a phase difference is induced in between two counter-propagating paths due to rotation [1]. However, the limited sensitivity of his original setup did not let him be the one who obtained the actual rotation rate measurements. Some more time had to pass for this to happen. 12 years later in 1925, thanks to the increased sensitivity that they achieved by building a 2010x1113 feet rectangular interferometer, Michelson and Gale were able to measure the Earth's rotation [2].

Unfortunately, the unreasonable size of a system to obtain useful performance has caused the effect which Sagnac unearthed not to attract considerable attention. On the other hand, the idea of having a gyroscope which has no moving parts instead of mechanical gyroscopes was too attractive to give up on the subject. And luckily, the discovery of He-Ne laser came to the rescue at the end of 1960 by being an ideal element for interferometry. This discovery has drawn the fading attention of the scientists interested in this area and speeded things up.

In 1962, Rosenthal came up with a propose of achieving a higher sensitivity by recirculating the counter-propagating waves many times in a ring laser cavity, unlike the original setup of Sagnac where the waves circulate the path once [3]. This proposal was realised by Macek and Davis one year after Rosenthal [4].

The developments in the other areas of science have led people to find other ways rather than using a ring laser to enhance the Sagnac effect and obtain higher sensitivity. For example; the improvements of low-loss optical fibers, solid-state semiconductor light sources and detectors have paved the wave for using a multi-turn optical fiber coil for the enhancement [5]. Pircher and Hepner's proposal of fiber optic rotation sensor was followed by Vali and Shorthill's experimental demonstration [6, 7] in 1976 with also the help of Brown's coil of optical fiber proposal [8]. Eventually, all these progressions ended up with the advent of IFOG, and IFOGs have become the apple of not only researchers but also companies eye by offering advantages for many useful applications.

The fact that IFOGs are solid-state devices and have no moving parts, the ease of achieving higher sensitivity by increasing the number of wraps in the fiber coil used, their tendency for miniature manufacturing, long lifetime, very quick turn-on time, high reliability and precision are just some of the advantages that have ensured them outdistance the other types of gyroscopes [9].

2.2 Bedrock of an Interferometric Fiber Optic Gyroscope

IFOG is a kind of sensor which uses the interference of light to detect rotation in a ring interferometer. The physical phenomenon that lies behind the operation of a fiber optic gyroscope is the Sagnac effect. This effect states that the light wave propagating in one direction in a rotating loop is not equivalent to the light wave propagating in the opposite direction due to the phase difference induced by the rotation.

In an ideal circular path made of fiber at rest, i.e. ring interferometer, two counter-propagating light waves will meet at the same point at the same time without any phase difference as shown in Figure 2.1.

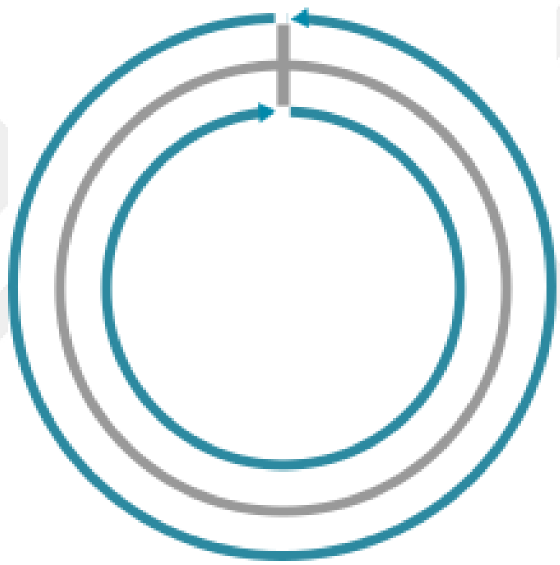

Figure 2.1: Schematic representation of two counter-propagating light waves meeting at the same point in a circular path at rest. Light beams moving in opposite directions in a non-moving circular path reach the same point at the same time without creating any phase difference.

However, if the ring interferometer rotates at a certain rate, for instance, in clockwise direction; the light waves moving in opposite directions will travel different lengths in different time intervals. The beam travelling against the rotation experiences a slightly shorter path than the other beam travelling in the same direction with the rotation. The beam travelling in the same direction with the rotation indicated with green experiences a slightly longer path than the other beam travelling against the rotation indicated with orange as shown in Figure 2.2.

If the interferometer rotates, for instance, at a rate of Ω angular velocity in clockwise direction, the length of the path that the wave propagating in clockwise direction becomes

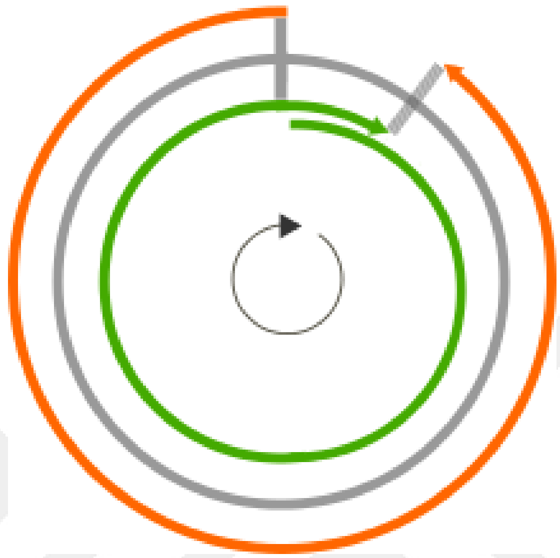

Figure 2.2: Schematic representation of two counter-propagating light waves creating a phase difference in a rotating circular path. Light beams moving in opposite directions in a rotating circular path will no longer reach the same point at the same time which cause the creation of phase shift.

$$L_{cw} = 2\pi R + R\Omega t_{cw} = ct_{cw} \tag{2.1}$$

and the length of the path that the wave propagating in counterclockwise direction becomes

$$L_{ccw} = 2\pi R - R\Omega t_{ccw} = ct_{ccw} \tag{2.2}$$

where R is the radius of ring interferometer, c is the speed of light. t_{cw} and t_{ccw} are the corresponding transit times of the travelling light waves in the corresponding directions which can be written as

$$t_{cw} = \frac{2\pi R}{c - R\Omega} \tag{2.3}$$

$$t_{ccw} = \frac{2\pi R}{c + R\Omega} \tag{2.4}$$

Under the assumption of $c^2 >> R^2\Omega^2$, the transit time difference Δt which is Δt = t_{cw} - t_{ccw} becomes

$$\Delta t = \frac{4\pi R^2 N\Omega}{c^2} \tag{2.5}$$

With the substitiuon of the loop diameter D=2R and the lenght L= 2πR, Δt becomes;

$$\Delta t = \frac{LD\Omega}{c^2} \tag{2.6}$$

So, Sagnac phase shift ΔΦ caused by a rotation of angular velocity Ω with the working wavelength of λ obtained as;

$$\Delta\Phi = \Omega t = \frac{2\pi c}{\lambda}\Delta t \tag{2.7}$$

$$\Delta\Phi = \Omega t = \frac{2\pi LD}{\lambda c}\Omega \tag{2.8}$$

As can be seen from the equation as well, Sagnac effect depends on the rotation rate Ω, working wavelength λ, the diameter D, and the length L of the fiber loop. By having multiple wraps on the fiber coil or by designing a fiber coil with a larger diameter, one can improve the sensitivity of a gyroscope since it will increase the the diameter D and the length L of the fiber [10].

Another important parameter for determining the quality of the IFOG is the scale factor which is basically indicated by the relation proportionality constant between Sagnac phase shift ΔΦ and angular velocity Ω. It can be written as follows

$$SF = \Omega t = \frac{2\pi LD}{\lambda c} \tag{2.9}$$

Considering the fact that IFOGs take the advantage of the phase shift between the counter-propagating waves induced by rotation, one has to ensure that the phase difference is due to the rotation only in order to have high accuracy. An ideal IFOG should be able to measure only Sagnac phase shift. However, the Sagnac effect is not the only source of measurable phase shift in practice. Environmental effects such as temperature [11], magnetic field [12] or vibration [13] creating differences in the optical paths can cause some undesired nonreciprocal phases apart from Sagnac phase shift. Because of the difficulty of distinguishing the real Sagnac phase shift from the other nonreciprocal phase shifts, reducing these nonreciprocal errors caused by the environmental effects becomes a necessity and the quality of these fiber optic rotation sensors are eventually determined by how much we are successful in the reduction of the errors [14, 15].

All the needs mentioned above makes a reciprocal configuration a must in an IFOG which means that the counter-propagating beams should travel the same optical paths so that the errors coming from the beam travelling in the clockwise direction will cancel the errors coming from the beam travelling in the counterclockwise direction and provide a highly accurate measurement at the end.

2.3 Componentry of an Interferometric Fiber Optic Gyroscope

Light source, multifunctional integrated optical chip (MIOC) and fiber coil are the main components forming an IFOG. Since light forms the base of the creation of these sensors, everything related to light becomes a key parameter to keep in mind.

The light source is the component which produces the light in an IFOG. Since the way of building an IFOG with high performance passes through a high performance

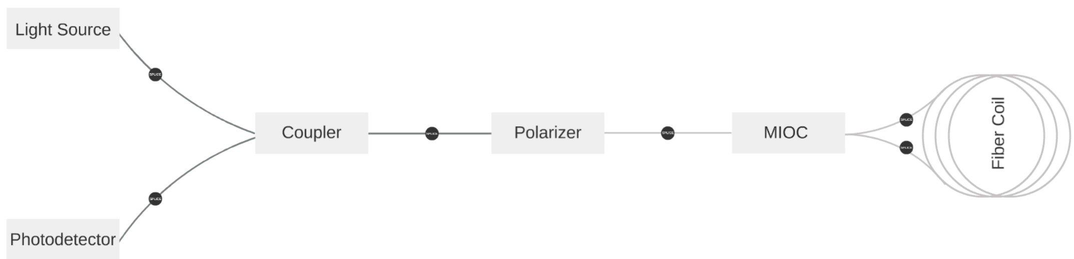

Figure 2.3: Schematic representation of an IFOG with basic configuration including MIOC. The light is produced in the light source, will be guided through a coupler, into a polarizer and get polarized, reach to MIOC, splitted here into two towards the fiber coil, then return back by following the similar path and reach out the photodetector.

light source, constructing a light source with high performance is a key parameter. Choosing to use broadband light sources improves the performance of the light source by eliminating optical Kerr effect, back-reflection and scattering [8]. Superluminescent diodes (SLDs) and amplified spontaneous emission (ASE) light sources are the two types of broadband light sources which are widely used in IFOGs. However, ASE light sources are preferred over SLDs because they have better wavelength stability with varying temperature and provide higher output power. As stated above in equation 2.9, scale factor is inversely proportional with wavelength, hence having a light source with better wavelength stability improves the overall quality of the IFOG. In addition, as IFOGs can be designed single, two, three or more axis depending on the needs of the systems that they are used; it also important to have high output power sufficient to be detected if when divided into multiple axes which is possible with using ASE light sources [9].

ASE light sources are made by using rare-Earth-doped optical fiber such as Erbium (Er)-doped, Ytterbium (Yb)-doped fiber or neodymium,. They posses broadband spectrum and low coherence. Since ASE is generated in the fiber core, it can be coupled to a single mode fiber with a very low coupling loss. The output is inheritly unpolarized which will help us to reduce the polarization nonreciprocities. Since the emission from a rare-Earth-doped optical fiber is generally very broad, a light source with a very broadband can be easily constructed. Moreover, with their high output power, they will allow us to use the same light source for three gyro axes after using a 1x3 fiber optic coupler splitting the beam into three [16].

Since the way of building an IFOG with high performance passes through using a high performance light source as stated above, we carried out our work to construct a light source with better quality in terms of wavelength, output power and their stabilities over temperature as well in this thesis in Chapter 3.

Multifunctional integrated optical chip (MIOC) is another of the three important components that make IFOG. This component works as polarizer, a splitter/combiner and phase modulator which modulates the optical wave in order to obtain accurate, non-linearity free response. This hybrid element splits the polarized light into two branches with equal power, and changes the effective index that the optical wave faces by applying electric field [5, 16, 17].

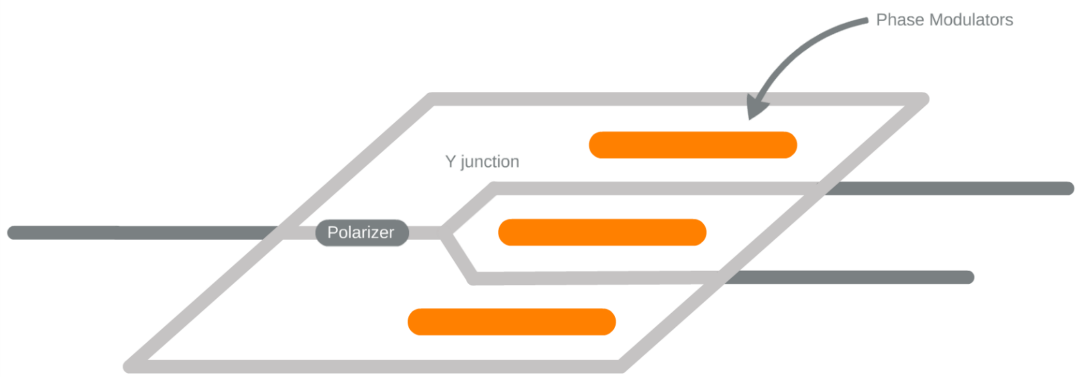

Figure 2.4: Schematic representation of the structure of a MIOC. Light guided through the MIOC is polarized, splitted into two in the Y junction and modulated.

Going through the MIOC, light will then reach to the heart of the IFOG which is the fiber coil. As the sensing element, fiber coil is the most important part of the IFOG. It should be carefully designed and wound in order to avoid the thermal and stress gradients which cause undesired nonreciprocal errors. Apart from the winding design of the fibers, the characteristics of the used fibers, the adhesives used during the production of the fiber coils, the material and the design of the spools on which the fiber coil is placed are also important parameters influencing the performance of the IFOGs.

To put it in a nutshell, the light is produced in the light source and guided towards the MIOC and finally the branched waves having the desired phase will close the loop by passing through the ends of the fiber coil.

2.4 More Room for Improvement of Interferometric Fiber Optic Gyroscopes

Of course interferometric fiber optic gyroscopes have eased so many things for the ones wanting to detect rotation with a small, non-moving optical system when considering the effort made to move forward on that rocky road. However, we still haven't reached the end of the road to build the perfect sensor fulfilling all the needs. We have a long way to go and there is still more room for improvement.

At this juncture comes the obstacles that we need to overcome, because an ideal interferometric fiber optic gyroscope should be able to measure only Sagnac phase shift, unfortunatelly in practice, the Sagnac effect is not the only source of measurable phase shift. Aside from the Sagnac phase shift, environmental factors that induce variations in the optical pathways might result in other undesirable nonreciprocal phases. Reducing these nonreciprocal errors brought on by environmental influences becomes essential due to the difficulty in differentiating between the real Sagnac phase shift and other nonreciprocal phase shifts. The effectiveness of this reduction ultimately dictates the quality of these fiber optic rotation sensors.

There are a variety of nonreciprocal parasitic effects in an IFOG. Some of them can be listed as backscatter, light source instabilities, polarization noise, electro-optic effects, magneto-optic effects, thermal and stress gradients, and electronic noise [5]. These will cause drift on the bias of the fiber optic gyroscope and degrade their performance. In order to get rid of the limitations and obtain best performance, the noise sources caused by the design of the gyroscope, the inherited properties of the fiber used and environmental effects should be minimized as much as possible.

Chapter 3

Let There Be Thermally Stable Light

3.1 Introduction

The aim of nipping in the bud lead us to start by focusing on the light source and try to construct the optimum configuration that works better under varying temperatures. One of the key parameter to delimitate the quality of an IFOG is the scale factor instability, ensuring it's stability means also ensuring the wavelength stability since it is directly related with the scale factor as can be also seen in Eqn. 2.9.

Considering the advantages mentioned in the previous chapter that they provide, amplified spontaneous emission (ASE) light sources are more widely used in IFOGs than superluminescent diodes (SLDs). The typical configuration of Erbium-doped fiber based ASE light source consists of a laser diode, erbium-doped fiber and a wavelength-division multiplexer (WDM).

Laser diodes are the electrically pumped semiconductor lasers in which the gain is generated by an electrical current flowing through a p-n junction or a p-i-n structure. They release energy portions as photons by the help of recombination of electrons and holes in these heterostructures. For the ease of combining the laser diodes with the other fiber-optic components and delivering the light where needed, the output of a laser diode can be coupled into an optical fiber. They have a specific wavelength and phase. They produce coherent laser beam with a narrow spectrum. The laser diodes used in these studies are drived by using a bench top laser diode thermoelectric cooling (TEC) controller controlling the laser diodes temperature in order to keep the wavelength as stable as possible and reduce the wavelength changes due to changing temperatures for eventually building a more efficient sensor.

Erbium-doped fiber is the gain medium of the ASE light source. As the name suggests, it is doped with different doping concentrations of Erbium which is a rare Earth metal. It is induced by the fiber coupled laser diode with the help of the last component of the ASE light source WDM where the light produced by the spontaneous emission is amplified with the stimulated emission optically [18].

Spontaneous emission occurs when an atom or a laser ion in a gain medium which is previously excited to a higher energy level by absorption of a photon is then spontaneously returns to a less stable lower energy level by releasing the energy in the form of a photon in some random direction. Stimulated emission occurs when a photon is incident on an atom or a laser ion in an excited state returns to a lower energy level by the emission of a second photon which has the same frequency, phase and direction as the original photon [19, 20, 21] .

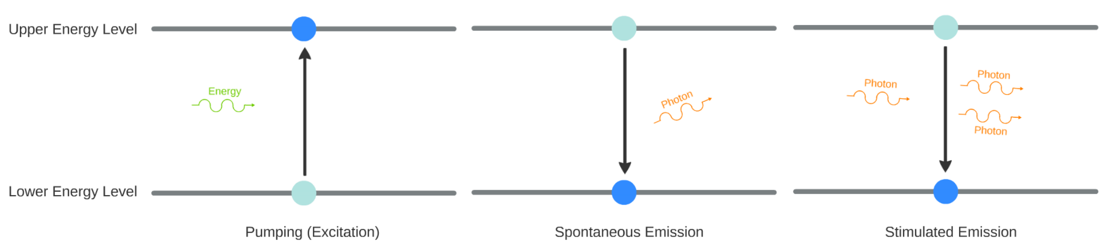

Figure 3.1: Schematic representation of spontaneous and stimulated emission. An atom absorbing a photon moves to an upper level, decays spontaneously to the lower level by emitting a photon in a random direction and phase; an incident photon causes an atom in the upper level to decay by emitting a stimulated photon with the same properties of the incident photon.

The occurrence of the stimulated emission depends on how strongly the gain medium is pumped and the creation of population inversion. On the other hand, spontaneous emission occurs regardless of the existence of the population inversion. So, for the laser amplification population inversion is required. It is the situation in which there are more atoms or molecules at an higher, excited state than in lower, unexcited states. Because of the unlikeliness of such situations in physical systems, it is called 'inversion' [20].

Two wavelengths are typically used to pump the Erbium-doped fiber amplifiers, shortly EDFAs such as 980 and 1480 nm. When an EDFA is pumped by a laser diode at which has 980 nm wavelength, Erbium ions absorb the pump light and get excited to an excited state(2). Since the lifetime of the excited state is relatively short, the excited ion immediately relaxed to lower excited state(1) by radiating heat. This relaxation creates a population inversion between the excited state(1) and ground state and amplification occurs at around 1550 nm [19, 22, 23].

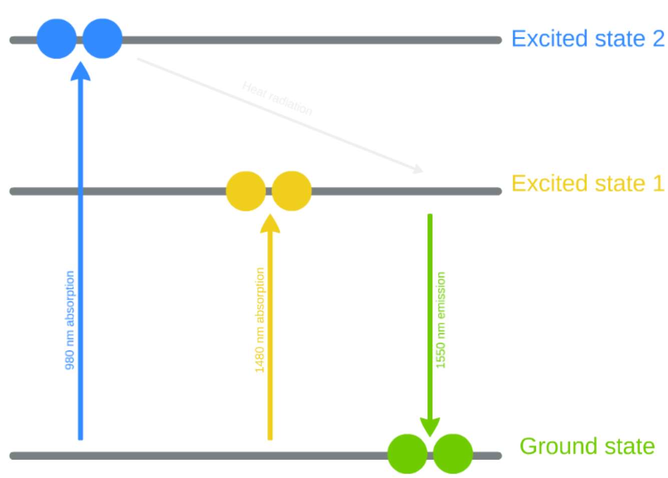

Figure 3.2: Energy diagram of Erbium. Amplification of Erbium takes placed at 1550 nm when pumped with two typical wavelengths namely 980 nm and 1480 nm.

Wavelength division multiplexers combine light signals coming from different fibers that have different wavelengths onto a single fiber. Here in our studies, this component is used to deliver the light pumped by the laser diode to the Erbium-doped fiber. We used a hybrid isolating WDM, or IWDM, which also has an isolating property to eliminate the unwanted backreflections and stabilize the signal as much as possible which again will help us to build a more efficient IFOG starting from the light source.

By using these components, one can build an ASE light source and pump the system in three different ways such as forward, backward and bidirectional. In forward pumping, the pump wave travels in the same direction as the signal wave. Vice versa, in the backward pumping the pump wave travels in the opposite direction as the signal wave and in the bidirectional pumping the system can be pumped simultaneously in both directions [24].

3.2 A Single Pass Backward Light Source

We started the tests with the conventional single pass backward light source pumped with a 980 nm LD of which schematics is given in Figure 3.3. The wavelength of the laser diodes in the typical light source configuration is chosen as 980 nm more importantly as it's one of the absorption wavelengths of Erbium doped fibers [25]. Besides, the fact that it is more up-to-date, cheap and easily purchased are the other advantages of choosing 980 nm as the wavelength of laser diodes here. The spectrum of the ASE light source obtained via an Anritsu Optical Spectrum Analyser (OSA) MS9740A at room temperature showed that the central wavelength was at 1548.9 nm with the bandwidth of 23.5 nm with 400 mA operating current as can be seen in Figure 3.4. The unused branch of the Erbium fiber was terminated by fusion splicing a certain length of coreless fiber optimized based on the length of the used Erbium fiber in order to eliminate the errors caused by the reflections. What is special about the coreless fiber it the fact that while a standard optical fiber has a core, a coreless fiber has just a glass rod without a distinct core as the name suggests.

This configuration exhibited a double-humped spectrum with a length of 10-m Erbium fiber used as the gain medium with a 1548.9 nm central wavelength and 23.5 nm bandwidth. The light source was tested over different temperatures changing in between -40°C and +85°C in a climatic chamber. The light source was placed in the climatic chamber, the output of the light source was connected to the OSA. A heat sensor was placed in the climatic chamber to measure the temperature changes in the climatic chamber. The data acquisition was done by using a laptop connected to both the heat sensor and the OSA assisted by a LabVIEW program as shown in Figure 3.5.

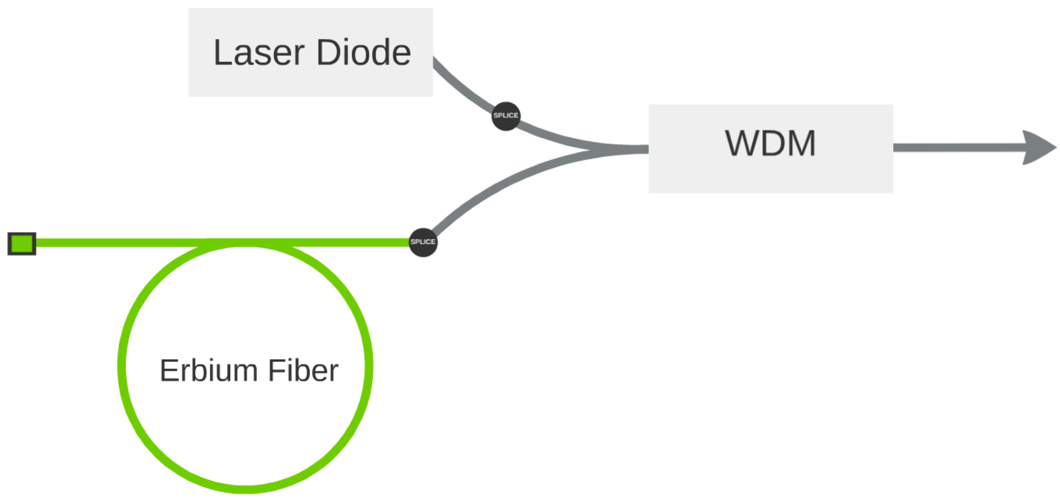

Figure 3.3: Schematic representation of the single pass backward light source. The simplest configuration of an ASE light source consists of a fiber integrated laser diode, a certain lenght of Erbium fiber and a WDM all of which are fusion spliced in a specific way.

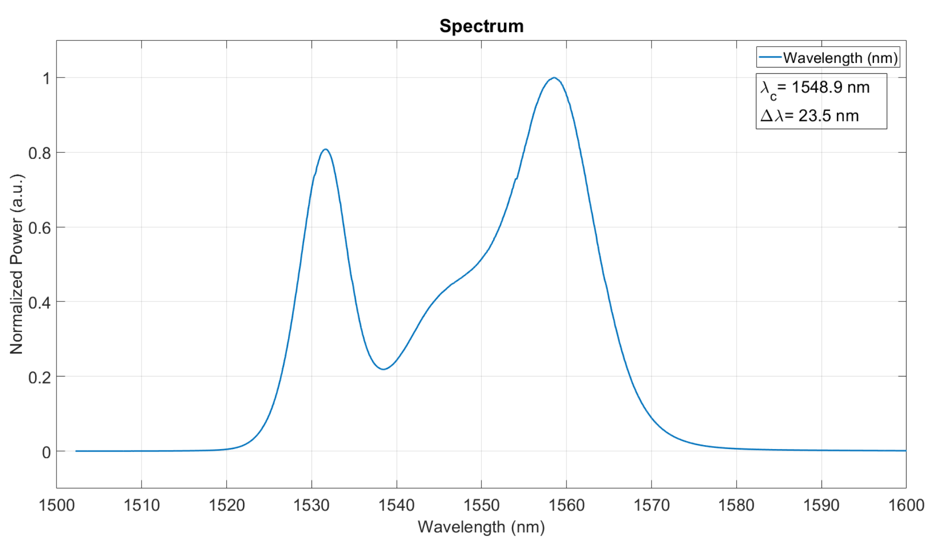

Figure 3.4: Spectrum of the single pass backward light source at room temperature obtained at 400 mA. The spectrum of a classical ASE light source represents a double-humped characteristic which can differ based on the operating current of the light source and the lenght of the Erbium fiber used.

Figure 3.5: The setup for testing the light source over different temperatures. The varying spectrum of the light source placed in the climatic chamber with respect to temperature is recorded and analyzed.

Temperature vs time, normalized power vs temperature, wavelength vs temperature, and wavelength stability vs temperature graphs are given in Figure 3.6, Figure 3.7, Figure 3.8 Figure 3.9 respectively. The results showed that the central wavelength of the light source was changed by 1.43 parts-per-million(ppm)/°C as shown in Figure 3.8. This shift caused 12 ppm instability in the wavelength Figure 3.9.

As already stated above, one can use 1480-nm LD to pump the Erbium-doped fiber amplifiers instead of 980-nm LD. Using the same configuration and by just changing the pump wavelength from 980 nm to 1480 nm, we kept running the tests at the same operating current of 400 mA with the coordinately changed WDM. The spectrum of the light source at the room temperature showed that we have shifted the central wavelength by 5.9 nm from 1548.9 nm to 1554.8 nm, we have narrowed down the bandwidth from 23.5 nm to 17.2 nm due to the drop of the peak of the first hump in the spectrum. The simulations made by using VPI-photonics [26] also supported the experimental results showing 1554.2 nm central wavelength and 17 nm bandwidth.

The light source was tested over different temperatures changing in between -40°C

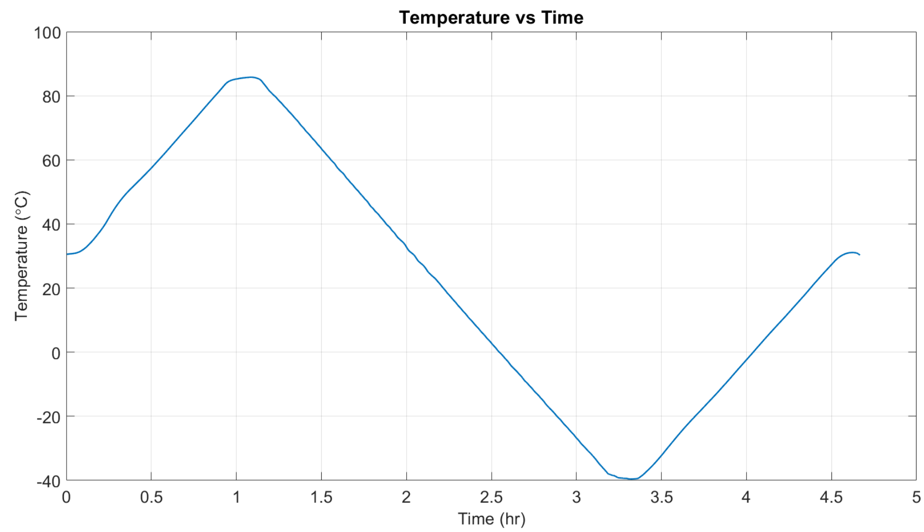

Figure 3.6: Temperature vs time graph of the single pass backward light source tested in the climatic chamber.

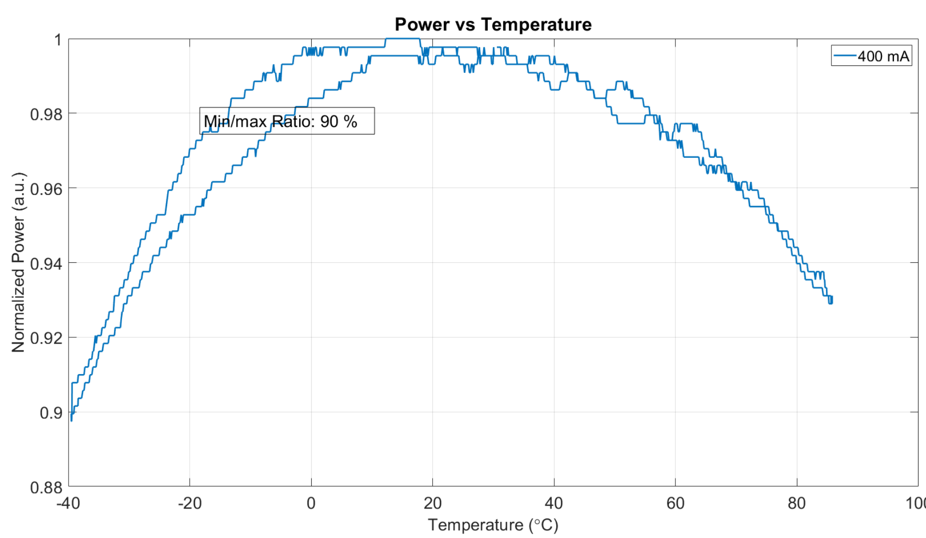

Figure 3.7: Normalized power vs temperature graph of the single pass backward light source tested in the climatic chamber.

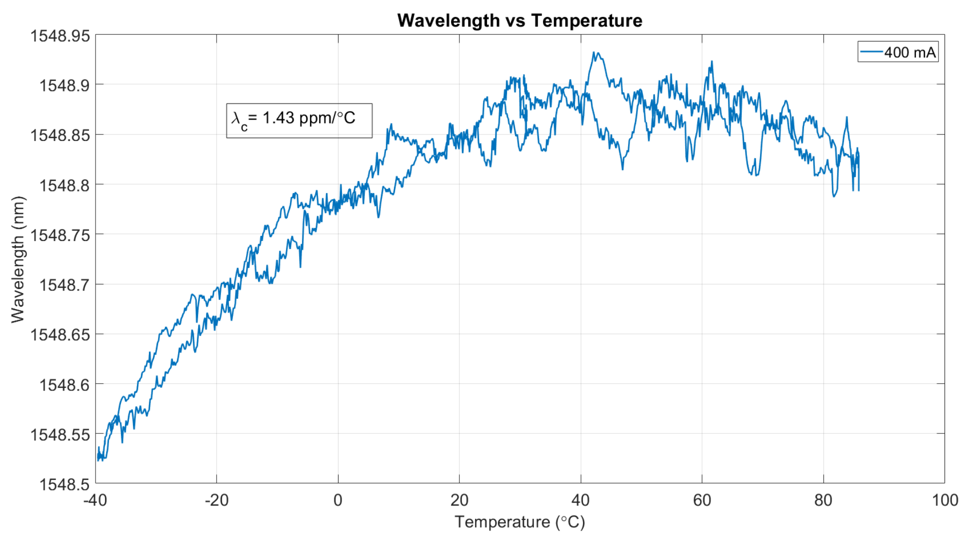

Figure 3.8: Wavelength vs temperature graph of the single pass backward light source tested in the climatic chamber.

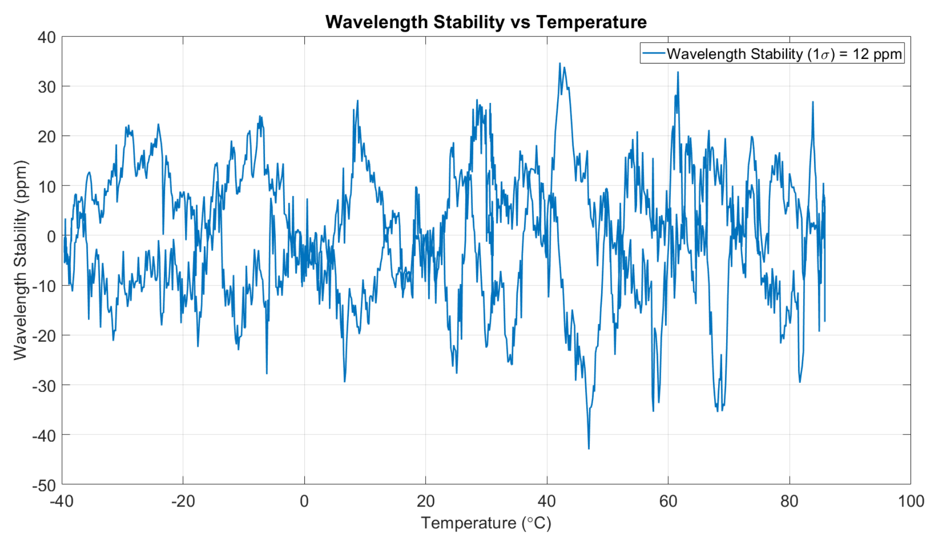

Figure 3.9: Wavelength stability vs temperature graph of the single pass backward light source tested in the climatic chamber.

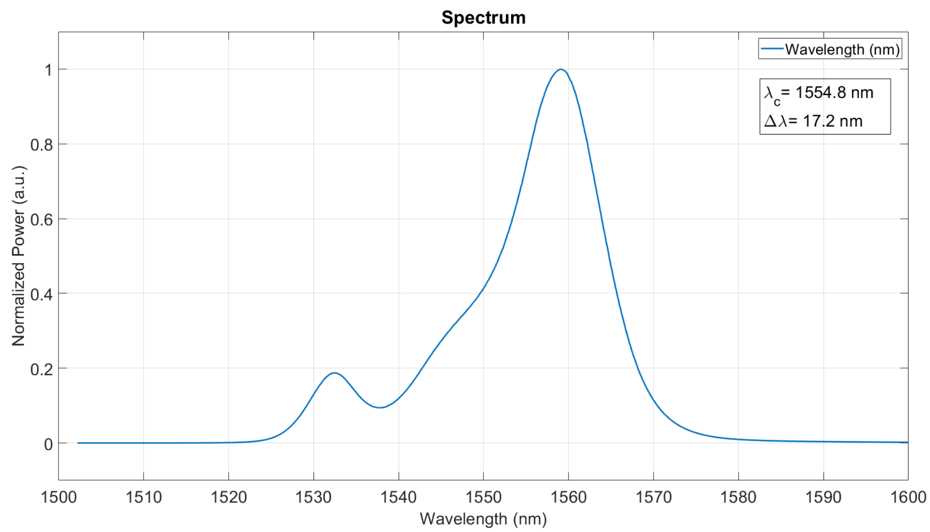

Figure 3.10: Spectrum of the single pass backward light source at room temperature obtained at 400 mA with 1480 nm LD.

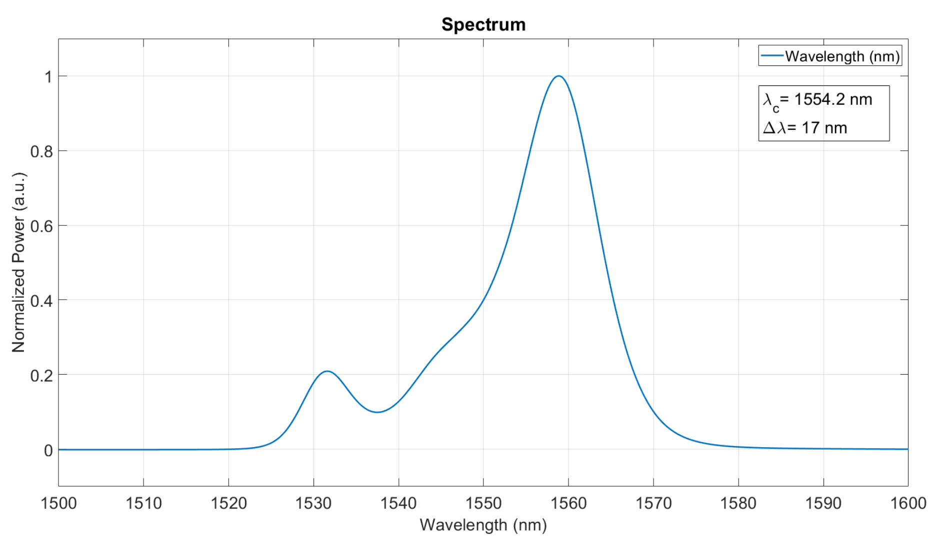

Figure 3.11: Simulated spectrum of the single pass backward light source at room temperature obtained at 400 mA with 1480 nm LD.

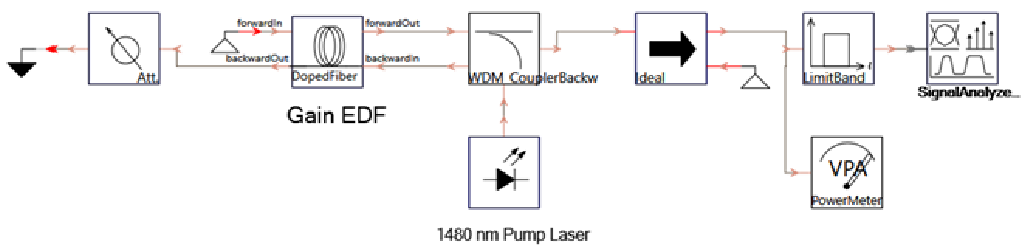

Figure 3.12: Schematic diagram of the single pass backward light source in VPI-photonics obtained at 400 mA with 1480 nm LD.

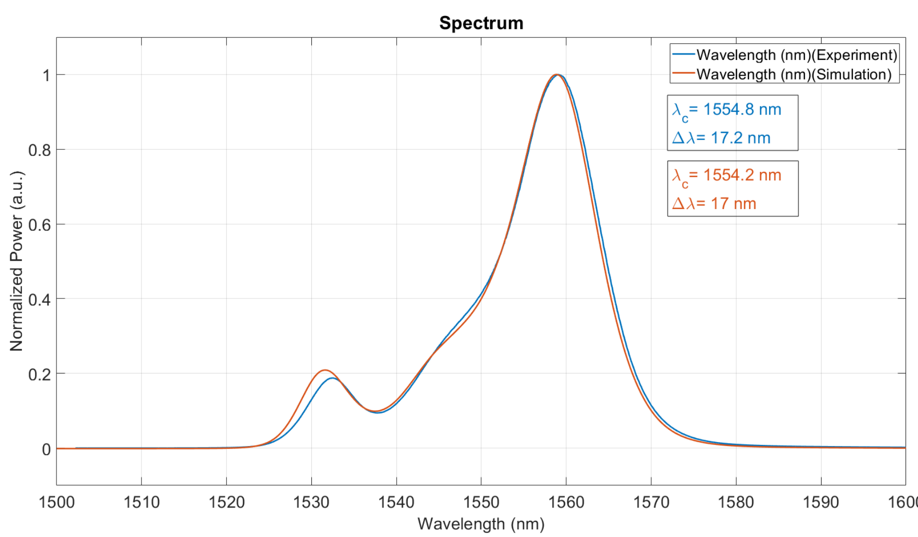

Figure 3.13: Comparison of the spectrums of the single pass backward light source at room temperature obtained at 400 mA with 1480 nm LD obtained from the experiment and simulation.

and +85°C in a climatic chamber with the same experimental setup and under the same conditions. Temperature vs time, normalized power vs temperature, wavelength vs temperature, and wavelength stability vs temperature graphs are given in Figure 3.14, Figure 3.15, Figure 3.16 Figure 3.17 respectively. The results showed that the central wavelength of the light source was changed by 14.3 parts-per-million(ppm)/°C as shown in Figure 3.16. This shift caused 6.7 ppm instability in the wavelength Figure 3.17. Although use of 1480-nm LD in constructing the light source narrowed down the bandwidth, the light source performed better under varying temperature in terms of wavelength stability. We traded of the bandwidth over a more thermally stable wavelength.

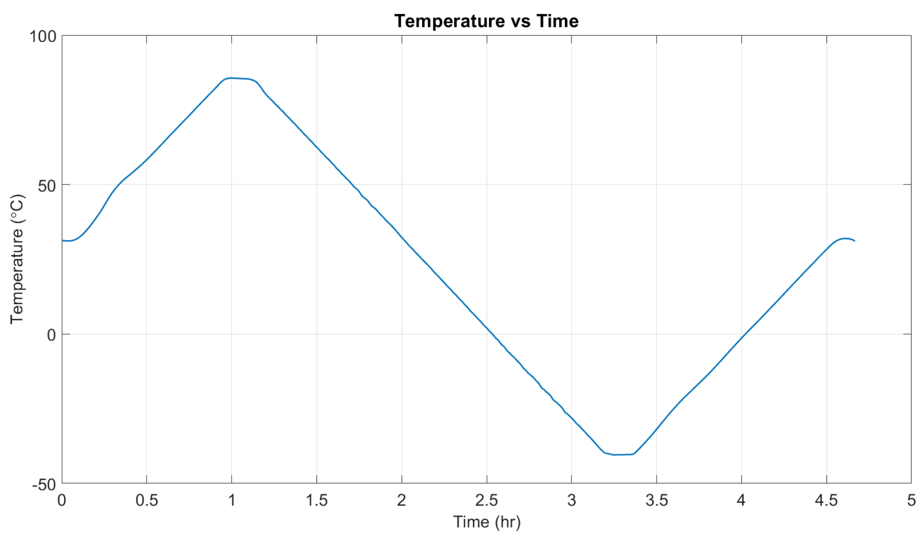

Figure 3.14: Temperature vs time graph of the single pass backward light source at room temperature obtained at 400 mA with 1480 nm LD tested in the climatic chamber.

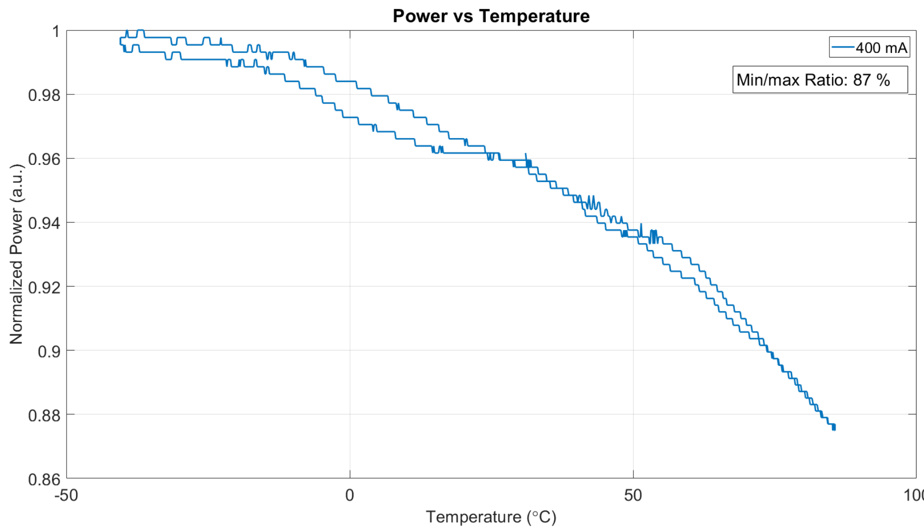

Figure 3.15: Normalized power vs temperature graph of the single pass backward light source at room temperature obtained at 400 mA with 1480 nm LD tested in the climatic chamber.

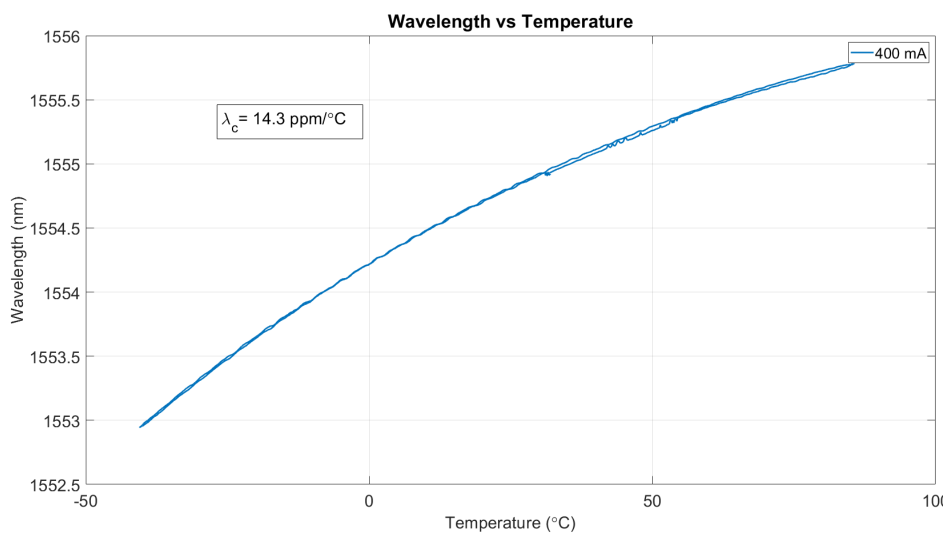

Figure 3.16: Wavelength vs temperature graph of the single pass backward light source at room temperature obtained at 400 mA with 1480 nm LD tested in the climatic chamber.

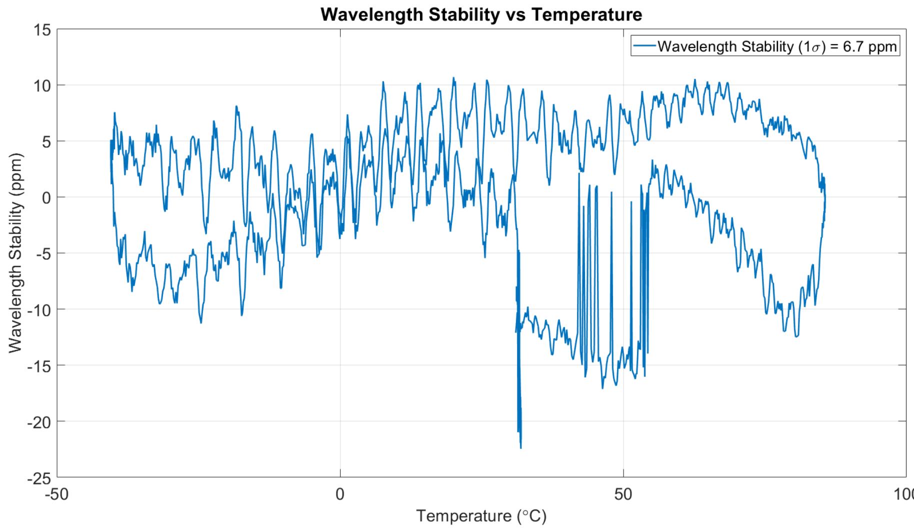

Figure 3.17: Wavelength stability vs temperature graph of the single pass backward light source at room temperature obtained at 400 mA with 1480 nm LD tested in the climatic chamber.

3.3 A Double Pass Bidirectional Light Source

Using LDs with different pump wavelengths individually went a long way in terms of the wavelength stability under varying temperature which directly affects the thermal performance of the IFOGs. However, those configurations should still be improved when considering the needs of the platforms that these rotation sensors are used. Taking a major step forward in the configuration, we used these LDs at the same time to pump the Erbium fiber, moreover we added a certain length of Erbium fiber working as a filter and a Faraday Mirror turning the configuration to double pass. The operating currents of the LDs, the lenght of the gain Erbium fiber and the filter Erbium fiber were chosen based on the spectrum and the output power [27, 28].

The schematics of the double pass bidirectional ASE light source is given in Figure 3.18. This configuration was subjected to the same experimental procedures starting from the measurements obtained at the room temperature and under the varying temperature conditions.

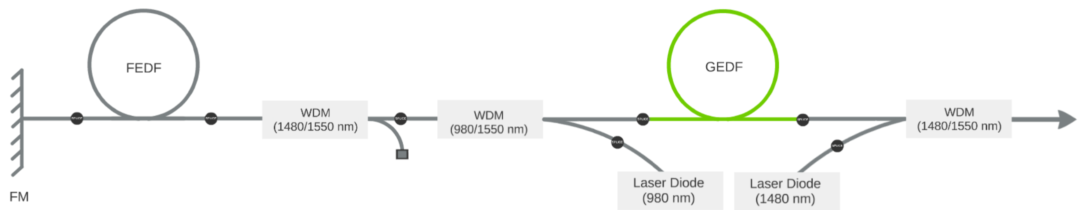

Figure 3.18: Schematic representation of the double pass bidirectional light source.

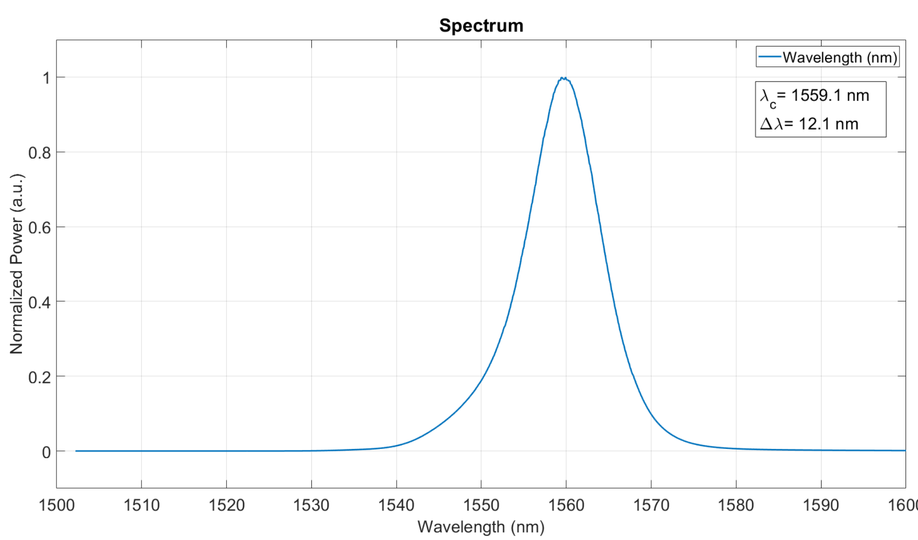

Figure 3.19: Spectrum of the double pass bidirectional light source at room temperature obtained at 400 mA.

The spectrum of the double pass bidirectional ASE light source is given in Figure 3.19. First hump in the spectrum was eliminated with the addition of the Faraday Mirror into the configuration, making the spectrum Gaussian with a central wavelength of 1559.1 nm and bandwidth of 12.1 nm. This experimental result is also verified with the simulation conducted via VPI-photonics. The shape of the simulated spectrum matches with the experimentally obtained spectrum with a central wavelength of 1559.5 nm and bandwidth of 12 nm.

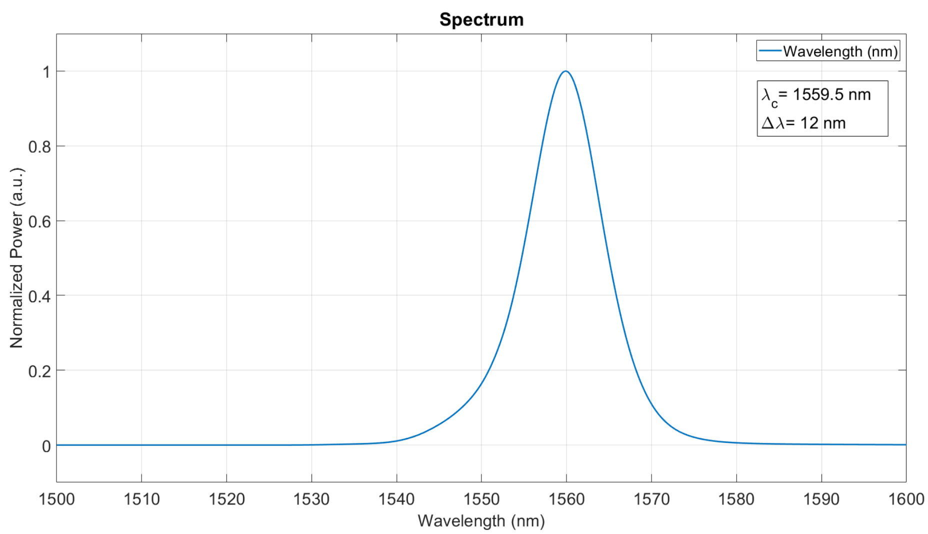

Figure 3.20: Simulated spectrum of the double pass bidirectional light source at room temperature obtained at 400 mA in VPI-photonics.

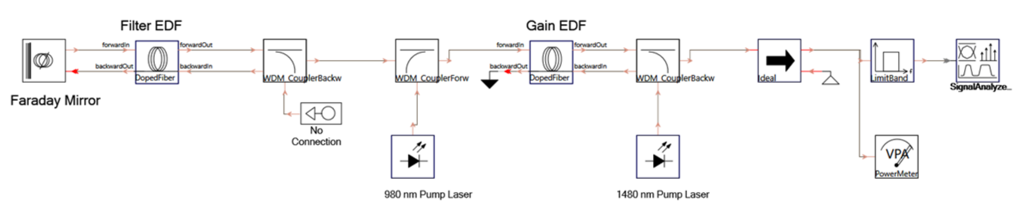

Figure 3.21: Schematic diagram of the double pass bidirectional light source in VPI-photonics obtained at 400 mA.

The light source was tested over different temperatures changing in between -40°C and +85°C in a climatic chamber with the same experimental setup and under the same conditions. Temperature vs time, normalized power vs temperature, wavelength vs temperature, and wavelength stability vs temperature graphs are given in Figure 3.23,

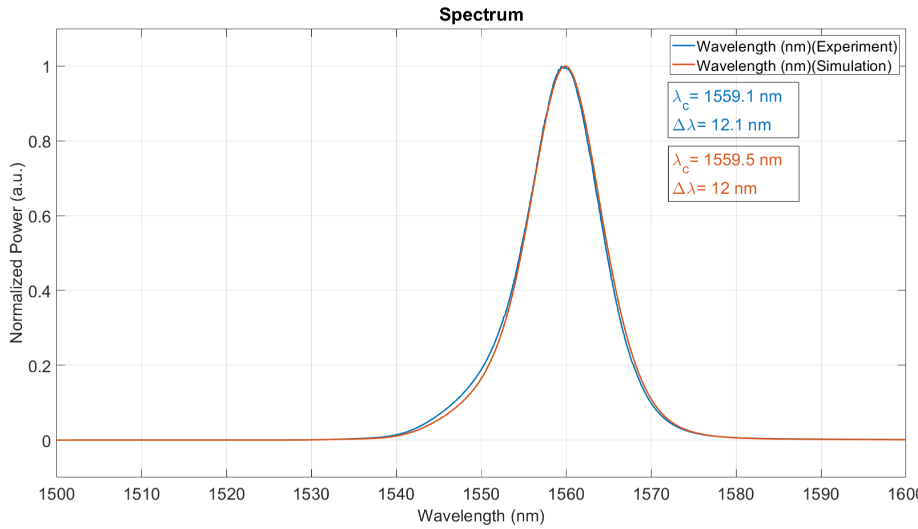

Figure 3.22: Comparison of the spectrums of the double pass bidirectional light source at room temperature obtained at 400 mA obtained from the experiment and simulation.

Figure 3.24, Figure 3.25 Figure 3.26 respectively. The results showed that the central wavelength of the light source was changed by -0.057 parts-per-million(ppm)/°C as shown in Figure 3.25. This shift caused 3.5 ppm instability in the wavelength Figure 3.26. Although we increased the number of optical components and complexity of the configuration in constructing the light source, the light source performed better under varying temperature in terms of wavelength stability. We traded of those over a more thermally stable wavelength.

To test the consistency of this configuration, we have built another light source with different optical components ruling out the individual effects of them. We have obtained similar results given in Figure 3.27, Figure 3.28, Figure 3.29, Figure 3.30 Figure 3.31 respectively, proving that one can use this configuration when a light source with thermally stabilised wavelength is needed.

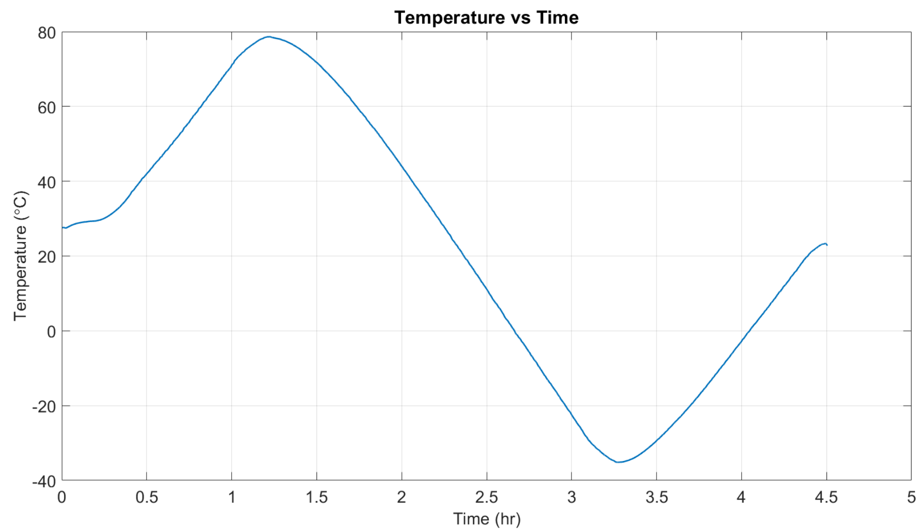

Figure 3.23: Temperature vs time graph of the double pass bidirectional light source tested in the climatic chamber.

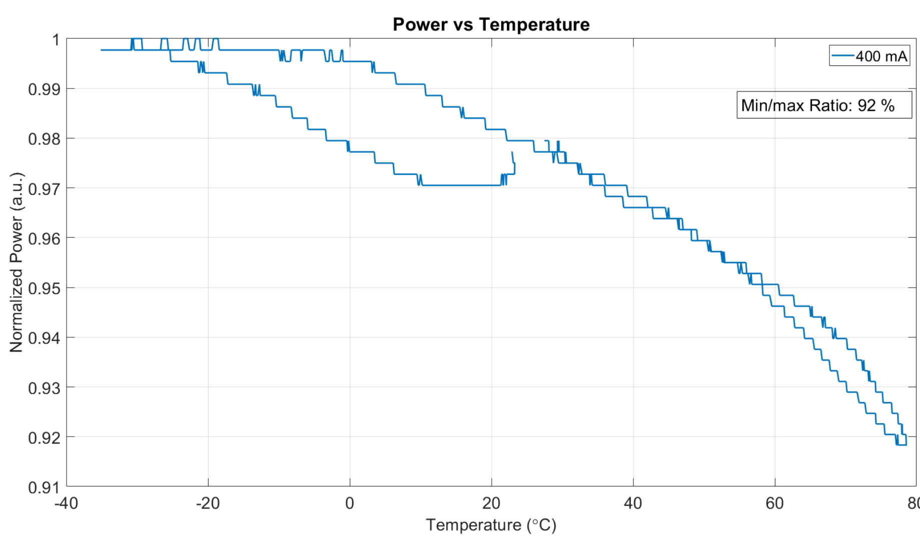

Figure 3.24: Normalized power vs temperature graph of the double pass bidirectional light source tested in the climatic chamber.

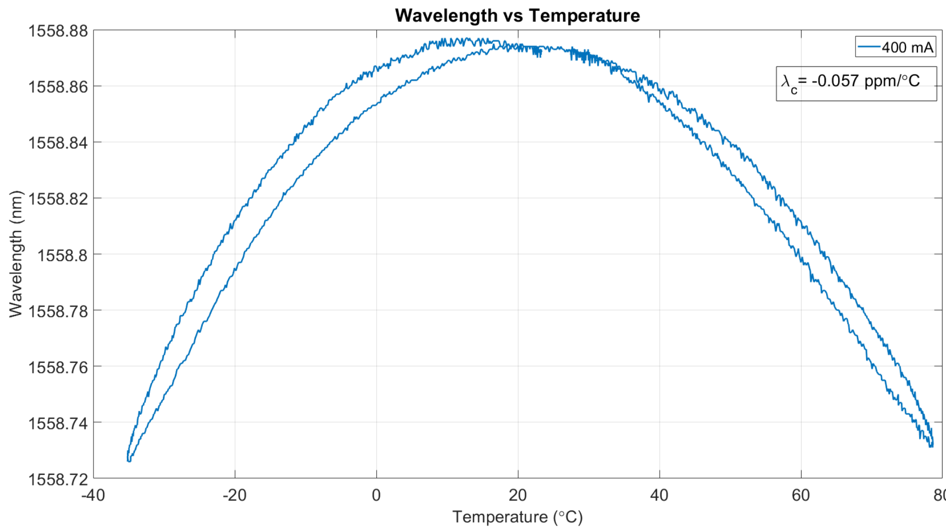

Figure 3.25: Wavelength vs temperature graph of the double pass bidirectional light source tested in the climatic chamber.

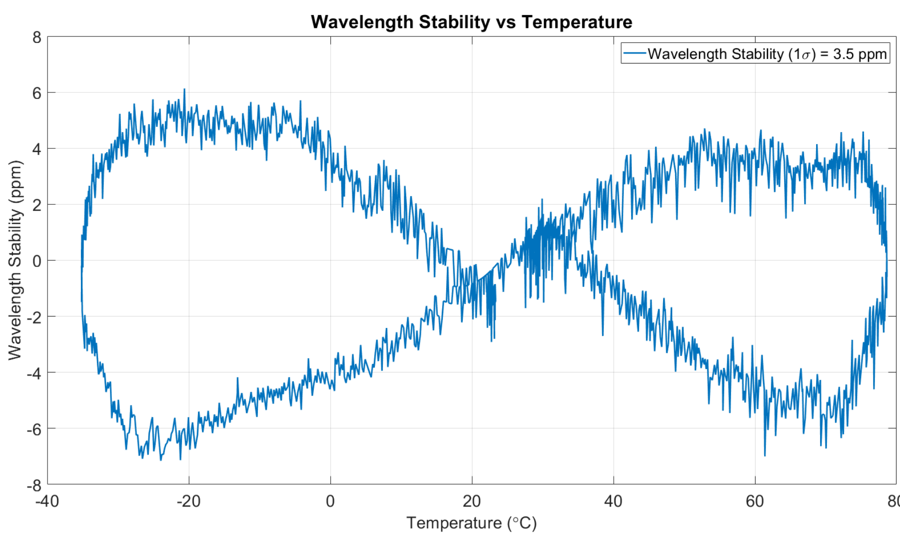

Figure 3.26: Wavelength stability vs temperature graph of the double pass bidirectional light source tested in the climatic chamber.

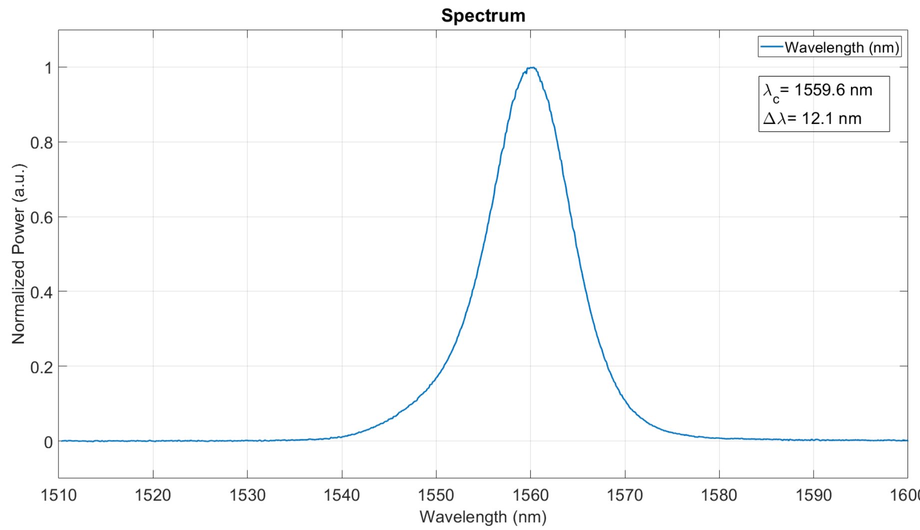

Figure 3.27: Spectrum of the double pass bidirectional light source at room temperature obtained at 400 mA.

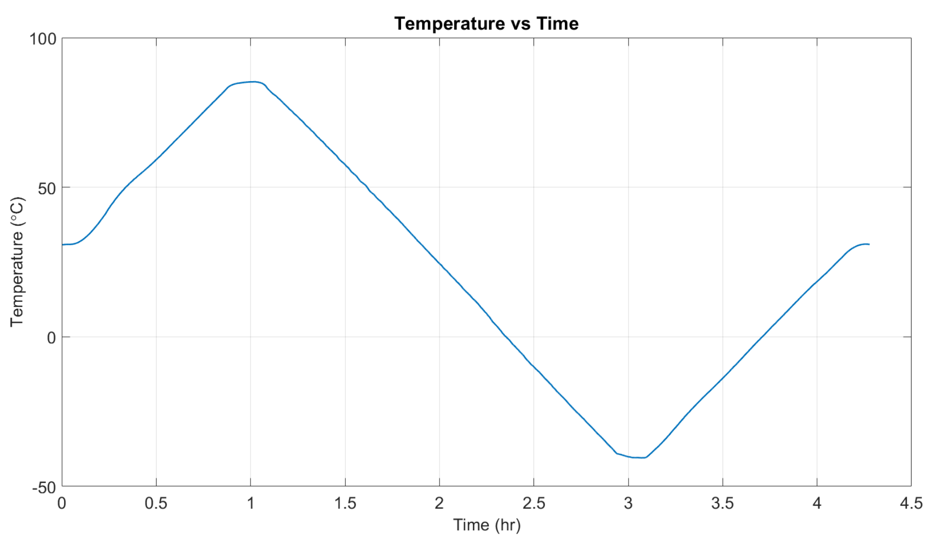

Figure 3.28: Temperature vs time graph of the double pass bidirectional light source tested in the climatic chamber.

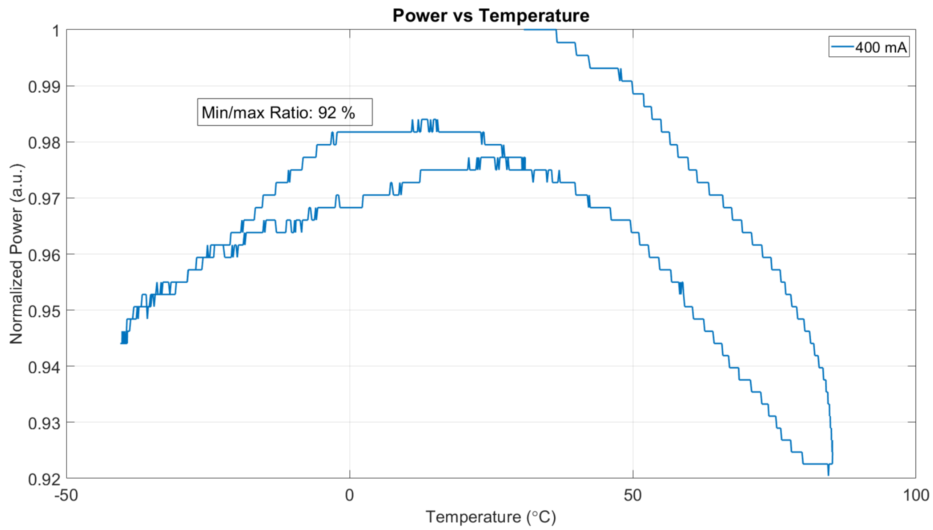

Figure 3.29: Normalized power vs temperature graph of the double pass bidirectional light source tested in the climatic chamber.

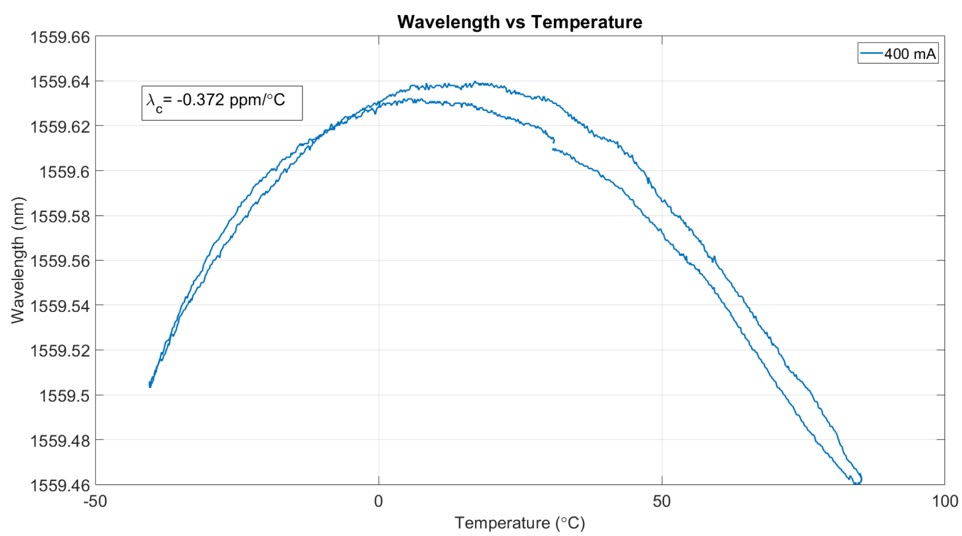

Figure 3.30: Wavelength vs temperature graph of the double pass bidirectional light source tested in the climatic chamber.

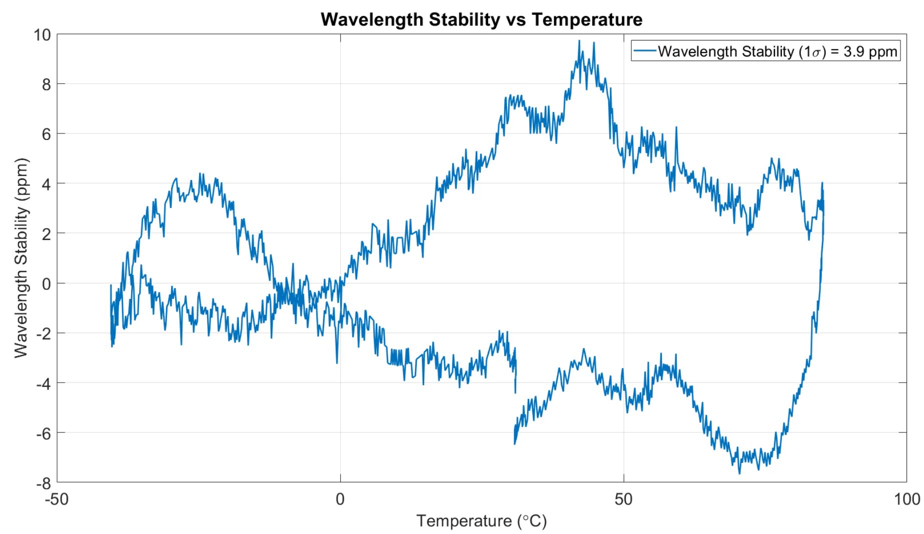

Figure 3.31: Wavelength stability vs temperature graph of the double pass bidirectional light source tested in the climatic chamber.

The range of applications of IFOGs are very wide from submarines to even spacecrafts. Reaching an almost record high thermally stable light source over a range of 125°C temperature change, we further analyzed the same configuration with different temperature ranges. The result in between -10°C and +60°C in a climatic chamber are given in Figure 3.32, Figure 3.33, Figure 3.34 Figure 3.35 respectively. This configuration hits its straps by providing a wavelength stability of 1.6 ppm over a range of 70°C temperature change which makes it a good candidate for serving the submarine applications for which the temperature exposure is not that harsh.

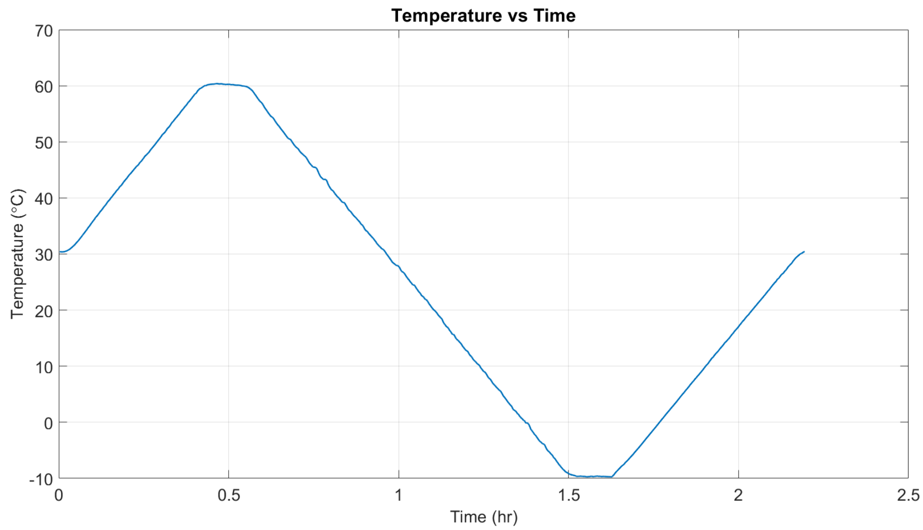

Figure 3.32: Temperature vs time graph of the double pass bidirectional light source tested in the climatic chamber.

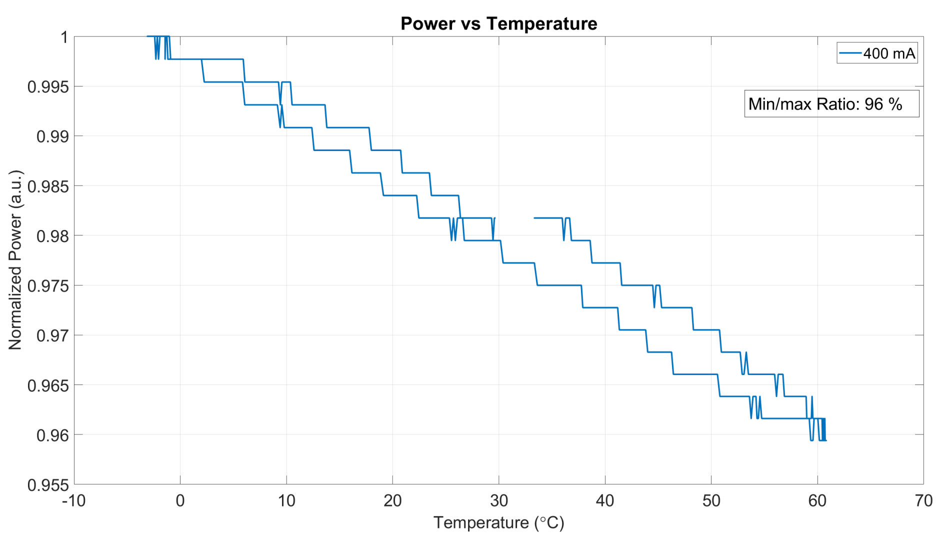

Figure 3.33: Normalized power vs temperature graph of the double pass bidirectional light source tested in the climatic chamber.

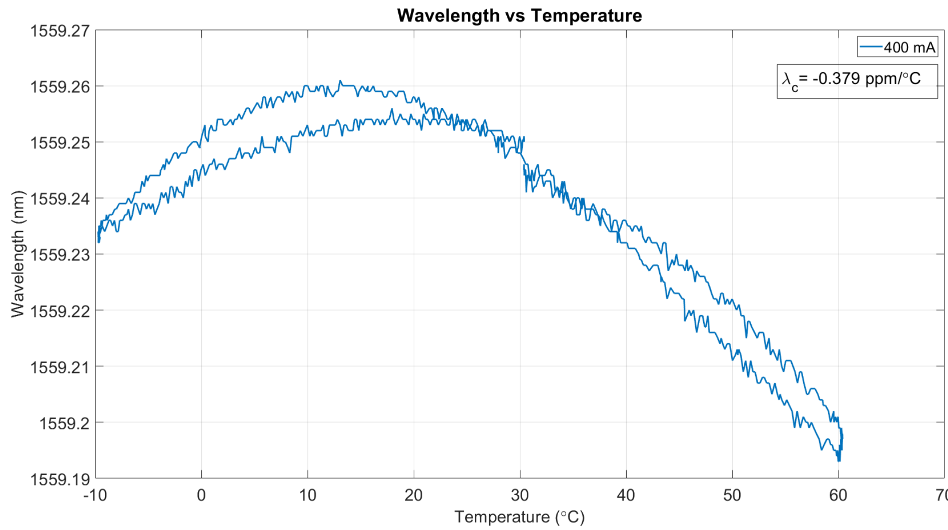

Figure 3.34: Wavelength vs temperature graph of the double pass bidirectional light source tested in the climatic chamber.

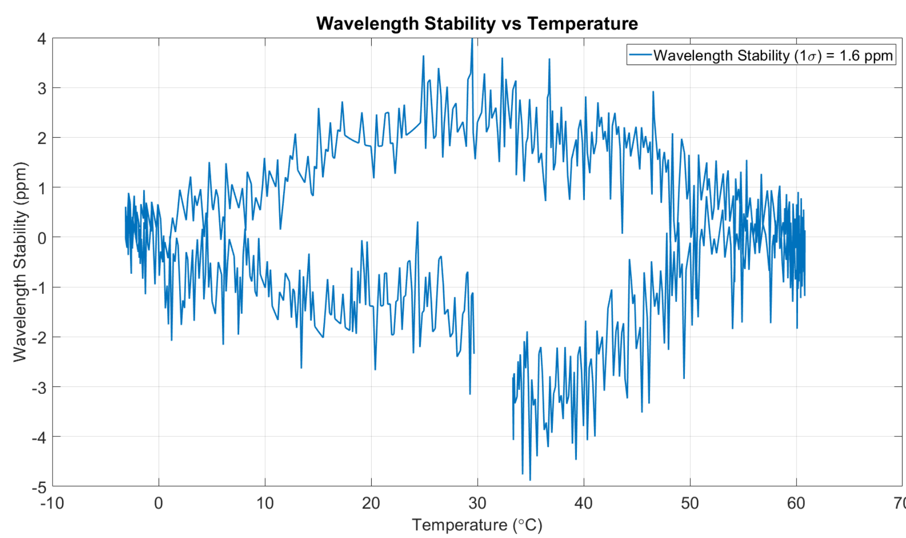

Figure 3.35: Wavelength stability vs temperature graph of the double pass bidirectional light source tested in the climatic chamber.

Chapter 4

Improving the Quality of the Fiber Coils

After launching the light from the source, it will pass from the multifunctional integrated optical chip and reach the sensing element of the rotation sensor which is the fiber optic coil.

As the sensing element of a fiber optic gyroscope, fiber coil is the hearth of an IFOG. It should be carefully designed, wound, and fixated in order to avoid the thermal and stress gradients which cause undesired nonreciprocal errors.

One of the largest error sources in an IFOG is the Shupe effect [11]. It occurs in the presence of time-varying spatial gradients arising from acoustic noise, vibration transients, thermal, and stress perturbations across the fiber optic sensing coil. These perturbations cause a time-varying refractive index change along the fiber.

Luckily, there are some ways of minimizing these errors. For example, one can use special winding techniques in order to minimize the Shupe effect due to thermal transients. Moreover, the problems caused by the time-varying stress gradients can be overcomed by cementing the fiber wraps in the coil [10].

Before coming to the special winding techniques used in the production of fiber coils, we will first focus on the things which we can improve before starting the winding of the fiber coil to help improving the quality of the fiber coils.

4.1 A Cleaning and Adhesive Application Apparatus for Optical Fiber

Nowadays, with the developing technology, fiber optic cables have begun to replace metal cables and have become widely used thanks to the advantages they provide. Fiber optic cables are generally used as windings of several hundred meters depending on the application in many sensors especially sensors such as IFOGs. The need to protect fiber optic cables due to their thin and delicate structure has led to develop new methods. Potting the optical fiber during the winding process, using adhesives or coatings are one of the most widely used and effective methods to meet this need, they ensure a good coil ruggedness and minimize the errors caused by vibrations as well [9].

Based on the research done in the prior art, there are several ways that make it possible to protect the fiber optic cables in windings. The integrity of the windings can be ensured by using different adhesive application methods such as applying the adhesive by spraying on the optical fiber surface, coating the optic fiber surface with a syringe type adhesive applicator, and smearing the adhesive to the unpotted winding under vacuum [29]. However, the adhesive can not be applied homogeneously to the fiber surface and each of the layers in the winding in these methods, so problems such as deterioration of the geometric integrity of the winding are encountered.

The obligation of using special symmetric winding patterns starting from the midpoint of the optical fiber, the challenge of controllability of the adhesive applied to the surface of the optic fiber, the difficulty of adhesion and the fact that the adhesion quality depends on the surface cleanliness motivated us to develop a new apparatus. This newly designed cleaning and adhesive application apparatus includes a cleaning compartment that cleans the surface of the optical fiber before the adhesive application, a bonding compartment that smears the adhesive to the clean surface of the optical fiber and a scraper slot that ensures controlled and homogeneous coating on the surface. Moreover, the number of compartments can be increased upon the different needs. For example, an extra adhesion enhancing agent compartment placed after the cleaning compartment can also increase the adhesion rate of the optical fiber to the adhesive material after the cleaning phase. Thanks to these, it provides a new and practical solution to the problems mentioned above and improves the quality of the fiber optic winding. The schematics of the cleaning and adhesive application apparatus for optical fiber are given in Figure 4.1, 4.2, 4.3, 4.4 respectively. The patent procedures for this study have been completed and the patent certificate was received with TR 2019 10878 B patent number [30].

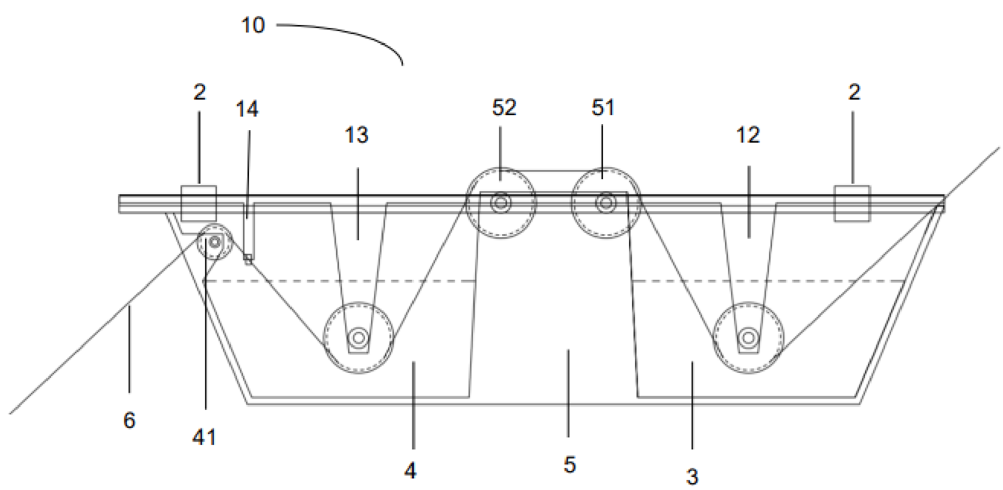

Figure 4.1: An exemplary cross-sectional view of the cleaning and adhesive application apparatus for optical fiber.

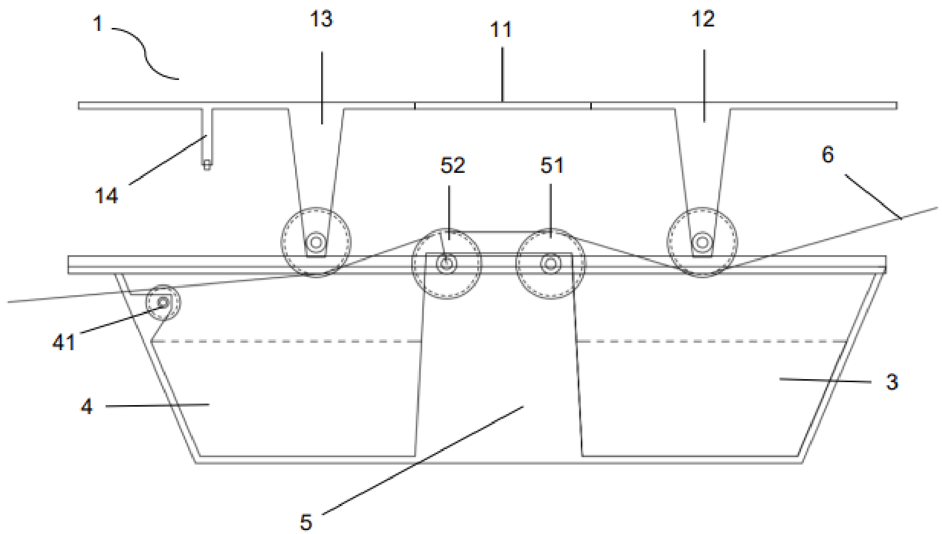

Figure 4.2: A sectional view of the cleaning and adhesive application apparatus for optical fiber before the lid is closed.

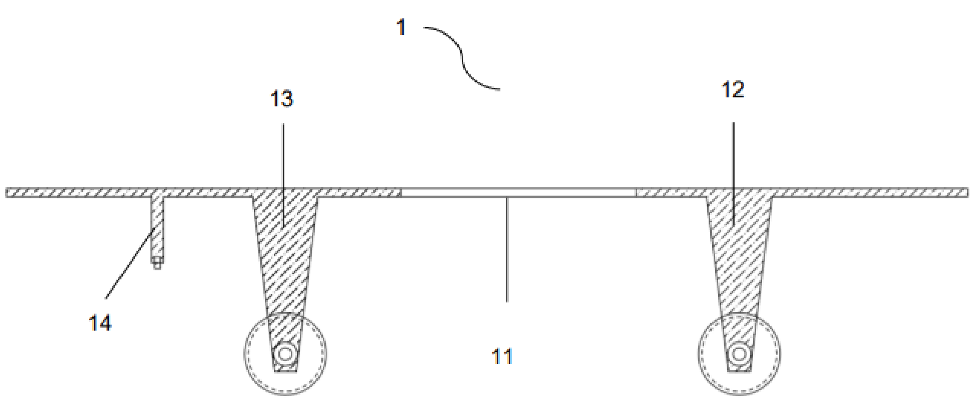

Figure 4.3: An exemplary cross-sectional view of the lid of the cleaning and adhesive application apparatus for optical fiber.

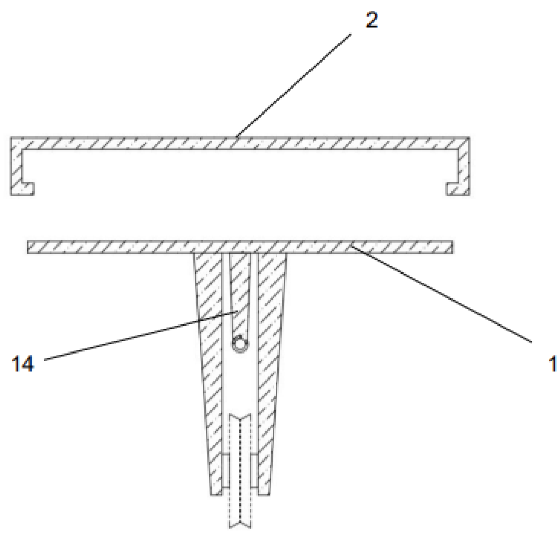

Figure 4.4: An exemplary cross-sectional view of the cover, clamp and scraper housing of the cleaning and adhesive application apparatus for optical fiber.

4.2 An Adhesive Applying Apparatus

When considering the variety of the adhesives used in the winding of fiber coils; we developed another adhesive application apparatus especially for the use of adhesives with high density, in cases where adhesives whose density increases over time or adhesives with short lifespan. This apparatus prevents accumulation-based clogging problems encountered during stripping of the excessive amount of the adhesive and eliminates the difference in the tension during the winding process which is a significant parameter for the performance of the fiber coil. It allows even stripping with the help of the stripping wheels and ensures a homogeneous adhesive coating on the surface of the optical fiber. The schematics of the adhesive applying apparatus for optical fiber are given in in Figure 4.5, 4.6, 4.7, 4.8, 4.9 respectively. The patent procedures for this study have been completed and the patent certificate was received with TR 2020 21883 B patent number [31].

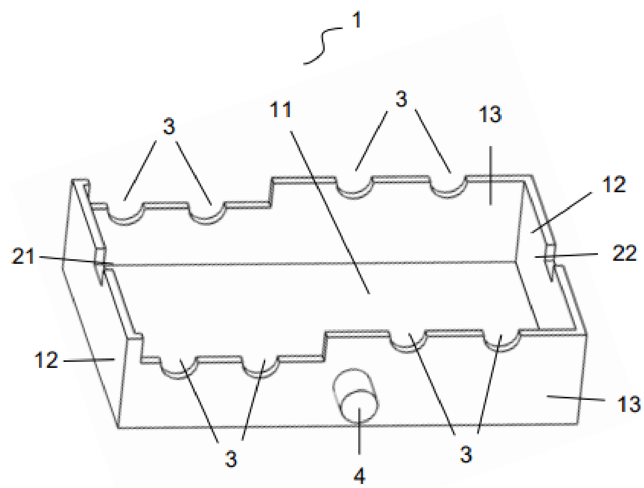

Figure 4.5: An exemplary axonometric view of the reservoir in the adhesive applying apparatus.

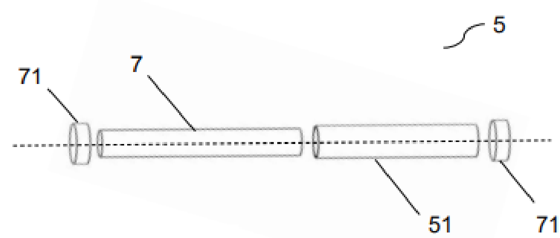

Figure 4.6: An exemplary exploded view of the application wheel.

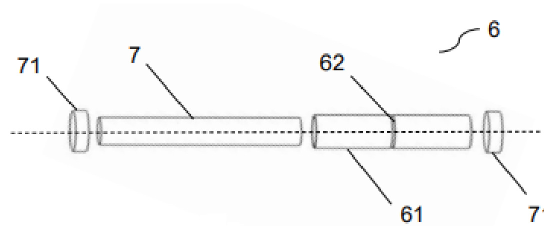

Figure 4.7: An exemplary exploded view of the scrapper wheel.

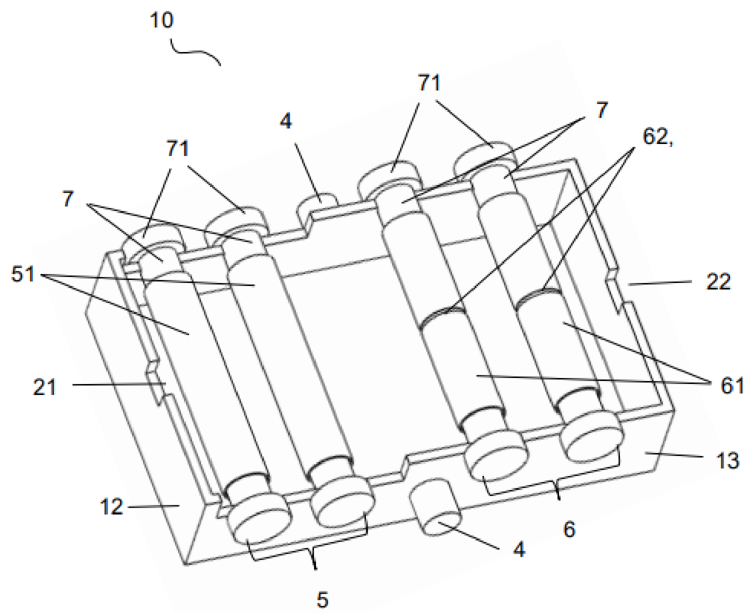

Figure 4.8: An exemplary axonometric view of the adhesive applying apparatus assembly.

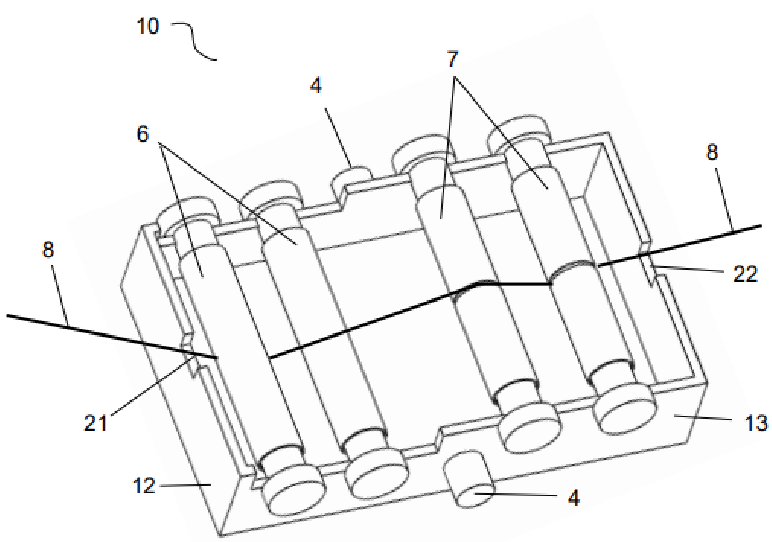

Figure 4.9: A sample view of the application of the adhesive applying apparatus.

4.3 An Adhesive Applying Apparatus for Optical Fiber

The compulsion of using adhesive in the production of the fiber coils encouraged us to keep working on improving the application of the adhesive in windings. We designed a new adhesive applying apparatus consisting of two identical elements in mirror symmetry of each other which reduces the contact of the adhesive material applied to the optical fiber with air, allows the optical fiber to be started from the desired point, enables controlled and homogeneous coating of the adhesive in a sealed closed environment, can be integrated into the fiber optic winding machine in the desired orientation and can be used continuously.

The primary aim of this invention is providing a practical adhesive application apparatus that helps to increase the performance of the devices in which the produced fiber coil is used against the environmental effects by applying homogeneous adhesive. It reduces the contact of the adhesive material used with air with it's sealed and closed structure. It reduces the operator-related errors, increases application speed, winding production speed and, thanks to the fiber exit groove it contains efficiency without the need of an external stripping guide. The apparatus allows the optical fiber surface to be stripped of excess adhesive in a controlled and homogeneous manner simultaneously without the need for an external stripping guide thanks to the fiber exit groove it contains, helps to collect the excess adhesive in the chamber after the optic fiber exits and saves adhesive material. It provides a continuous use during fiber optic winding production with the help of the adhesive feeding slot where adhesive material can be added at any time. The schematics of the cleaning and adhesive application apparatus for optical fiber are given in in Figure 4.10, 4.11, 4.12, 4.13, 4.14 respectively. The patent procedures for this study have been completed and the patent certificate was received with TR 2020 21576 B patent number [32].

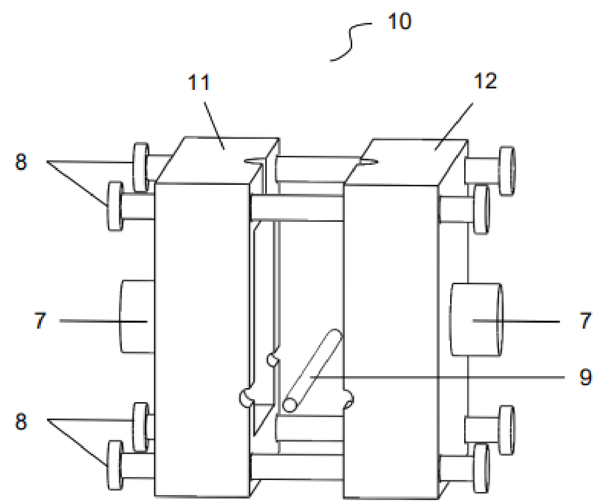

Figure 4.10: An exemplary exploded view of the adhesive applying apparatus for optical fiber.

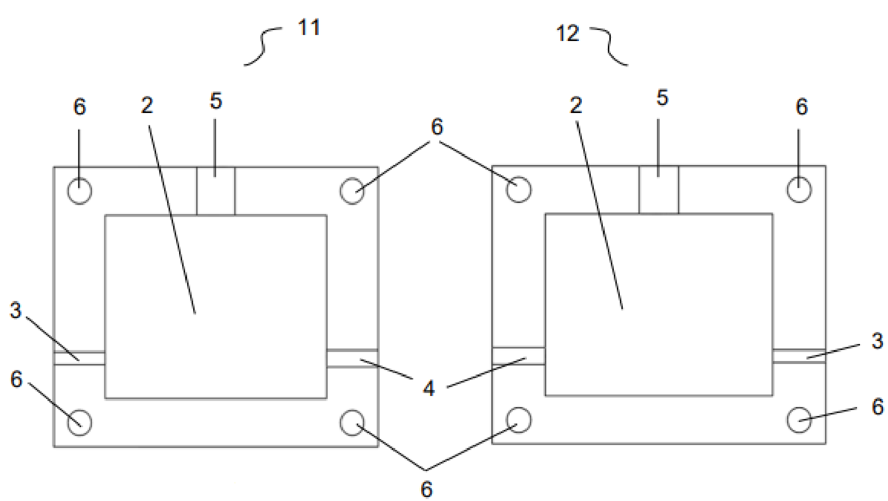

Figure 4.11: An exemplary front view of the left part and the right part the adhesive applying apparatus for optical fiber.

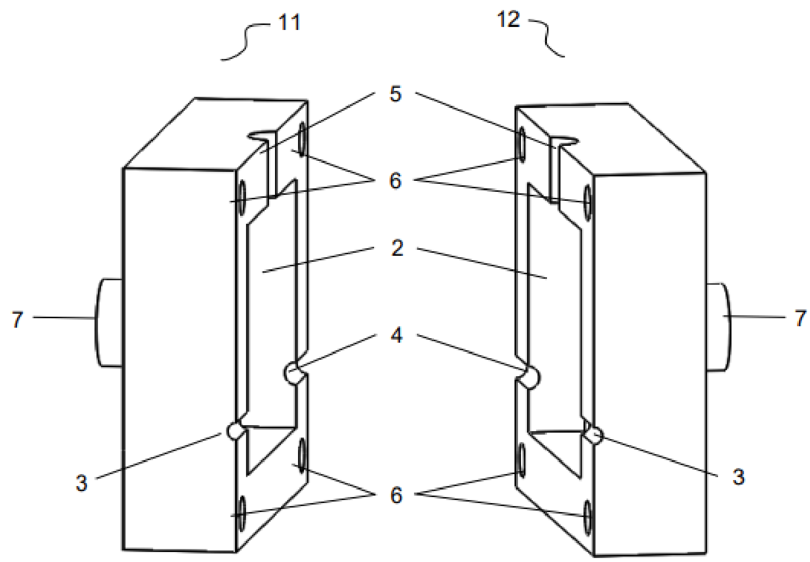

Figure 4.12: An exemplary side view of the left part and the right part of the adhesive applying apparatus for optical fiber.

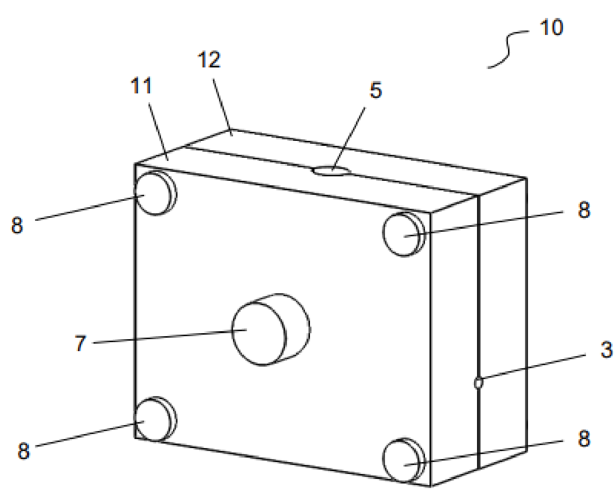

Figure 4.13: An exemplary axonometric post-assembled view of the adhesive applying apparatus for optical fiber.

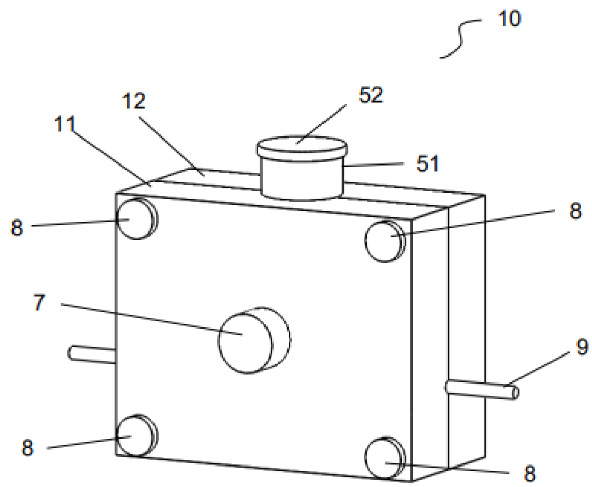

Figure 4.14: A sample view of the application of the adhesive applying apparatus for optical fiber.

4.4 A Fiber Optic Winding Spool

Apart from the applications ensuring the application of the adhesives on the optical fiber sensors, we kept working on improving the mechanic structure of the fiber optic winding and focused on the spool on which the winding is obtained. We developed a new spool on which fiber optic winding is obtained aimed to be used in IFOGs. This spool in particular containing a female part and a male part ensures the creation of a radial gap between the fiber optic winding and the relevant wall of the spool which reduces the temperature-related systematic errors caused by the thermomechanical incompatibility between the fiber optic winding and the material of the spool.

As already stated before, fiber optic coil is one of the most important subunits composing the IFOGs and it is obtained by winding the optical fiber of desired length around a spool in different numbers of turns and layers depending on the needs. The spools provide ease of holding the fiber optic winding together during the production of the fiber optic winding and are generally of a monolithic structure with a cylindrical core sandwiched between two flanges of the spool.

It is known that the fiber optic winding is negatively affected under temperature by the adhesive material used in the winding, the material of the spool on which the fiber optic winding is wound, and the spool structure. For this reason, the thermomechanical mismatch between the spool and the fiber optic winding must be reduced in order to reduce the temperature-related systematic errors in IFGOs. Today, the studies on the spools required to produce and integrate fiber optic windings continue with this object in mind.

There are many ways of reducing the stress on the fiber optic winding caused by the presence of the spool. Using spools with similar thermal expansion characteristics as the fiber used in the fiber optic winding instead of standard metal spools, creating a buffer zone around the side wall surface and the cylindrical core of the spool in contact with the fiber optic winding, producing the fiber optic winding with on a spool having a larger diameter than the original spool which will be used for fixing the fiber optic winding, then removing the fiber coil and then attaching it on the original spool can reduce the stress on the fiber optic winding, and accordingly, temperature-related systematic errors in the IFOGs in which the fiber coil is used. However, the use of a fiber optic winding with different radial and axial expansion characteristics on a double-walled reel with an isotropic expansion characteristic produced from a single material causes imbalance and causes systematic stress-induced errors on the fiber optic winding. Problems such as difficulty in matching the thermal and mechanical characteristics of fiber optic winding and the spool material and increased complexity of the spool design are encountered. Moreover, choosing to use additional buffer zones in the contact surfaces of the fiber optic coil and the spool adds more processing steps, causes implementation difficulties and increases the cost.

Taking into account all these, new and practical spool designs should be alternatively developed in order to eliminate difficulties such as using different materials on the inner surface of the spool which is in contact with the fiber optic winding itself and to rule out the need of creating an interface or buffer zone in between the fiber optic winding and the inner surface of the spool contacting the fiber optic winding.

In the cases of the fiber optic winding where the fiber optic coil is produced directly on the cylindrical core and sandwiched in between two flanges of the spool, the chance of facing the temperature-related systematic errors is increased due to the different thermal characteristics of the optical fiber itself, the adhesive used in the fiber optic winding and the material of the spool in contact with the fiber optic winding. This thermomechanical mismatch unfortunately worsens the thermal performance of the IFOG in which the fiber optic coil is used. In the use of the newly designed spool, the surface area which is axially in contact with the fiber optic winding is reduced by half by just using one flange at the bottom instead of two at the bottom and at the top. This newly designed spool further reduces the contact surface area by creating a radial gap in between the fiber coil and the spool the ruling out the radial contact of the fiber coil with the cylindrical core of the spool itself.

Thanks to these, this spool provides a new and practical solution to the problems mentioned above and improves the quality of the fiber optic winding. The schematics of the fiber optic winding spool are given in in Figure 4.15, 4.16, 4.17, 4.18, 4.15, 4.20, 4.21, and 4.22 respectively. The patent procedures for this study have been completed and the patent certificate was received with TR 2020 10982 B patent number [33].

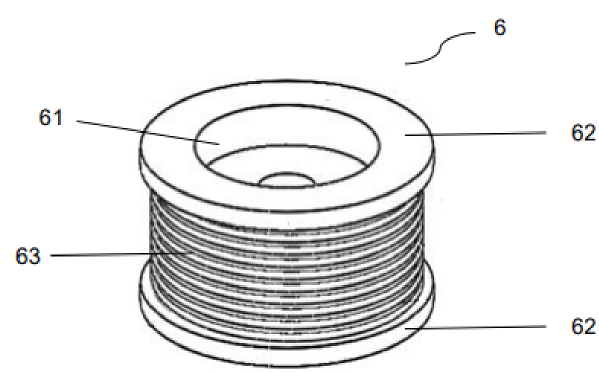

Figure 4.15: An exemplary view of the fiber optic winding spool in the prior art.

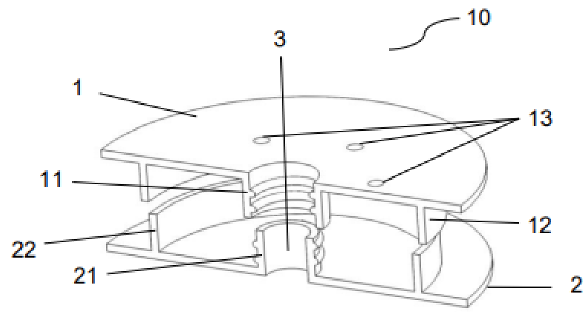

Figure 4.16: An exemplary exploded sectional view of the spool in the preferred application of the invention.

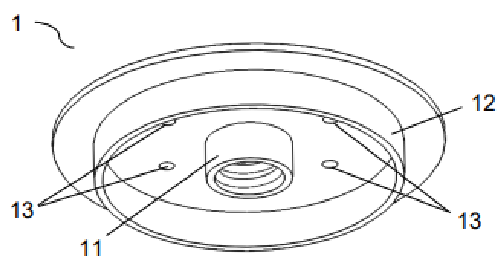

Figure 4.17: An exemplary view of the female part in the preferred application of the invention.

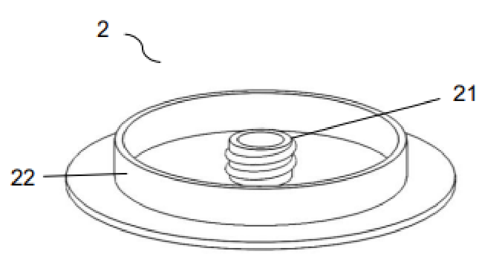

Figure 4.18: An exemplary view of the male part in the preferred application of the invention.

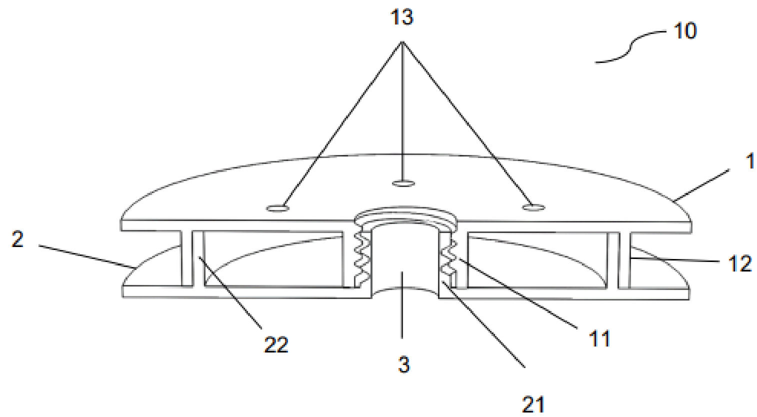

Figure 4.19: An exemplary sectional view of the assembled spool in the preferred application of the invention.

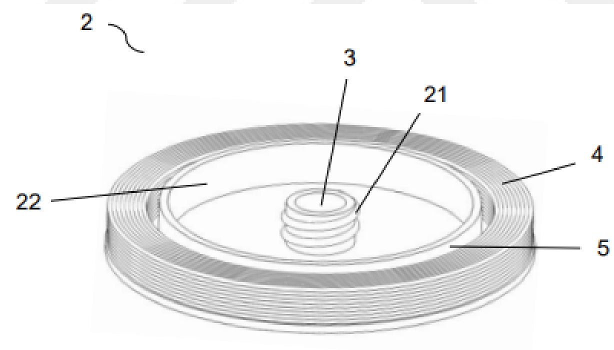

Figure 4.20: An example view of the fiber optic winding obtained on the male part in the preferred application of the invention.

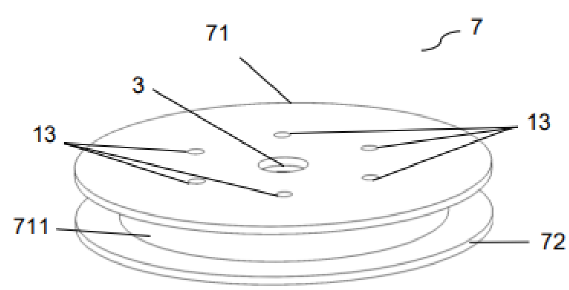

Figure 4.21: An exemplary cross-sectional view of the assembly of the winding spool in another embodiment of the invention.

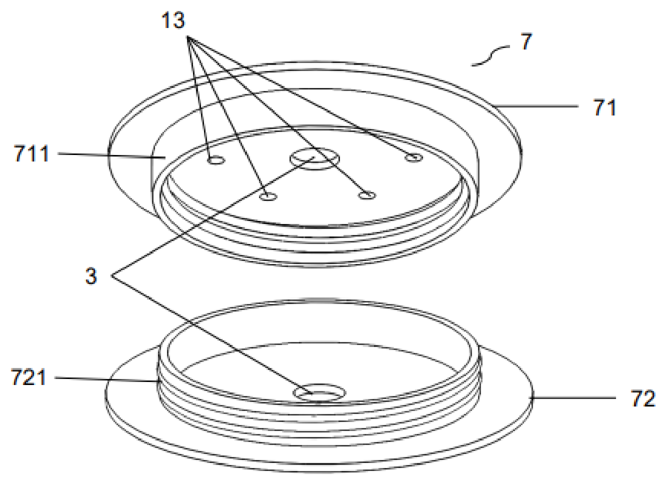

Figure 4.22: An example open view of the winding spool in another embodiment of the invention.

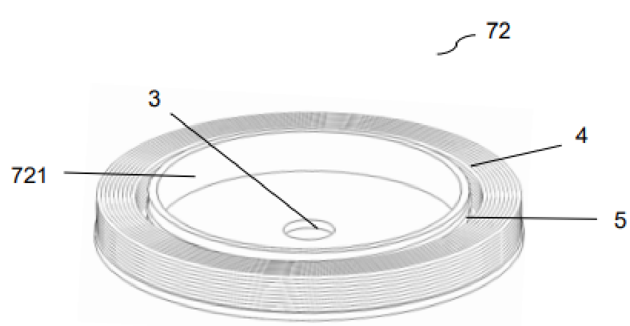

Figure 4.23: An example view of the fiber optic winding obtained on the lower part of the spool in another application of the invention.

4.5 A Method for Creating a Buffer Zone in an Interferometric Fiber Optic Gyroscope that Prevents Sudden Bias Deviations due to Temperature

IFOGs, which allow us to measure the rotation in moving systems is formed by the combination of three main subcomponents: a light source, a fiber optic winding and a MIOC. It can measure the rotation caused by the moving system thanks to the phase difference in the light traveling in opposite directions within the fiber optic winding. This phase difference changes depending on environmental factors such as magnetic field, vibration and temperature, and this change directly affects the system performance of the IFOG. To improve the magnetic field sensitivity of the system, magnetic shields made of high permeability alloys are used in the system. In order to improve vibration sensitivity, the optical fiber is coated with a high elasticity modulus adhesive during the production of the fiber optic coil. In order to improve temperature sensitivity, in addition to using special winding patterns in fiber optic winding production, methods such as doping the adhesive used in the production of fiber optic coil with different materials are also used. These environmental problems, which are outlined in general terms, are suppressed by the methods described here, but they cannot be completely eliminated. Studies to improve system performance are still ongoing.

The fiber pigtails of the fiber optic coil and the MIOC combined along with a light source forming the IFOG are brought together using special splicing techniques. After these special splicing processes, there are various alternatives such as using an adhesive tape or high elasticity modulus adhesive to fix the adhesive-free fibers. However, these methods can not provide sufficient fixation. Since it is often necessary to separate the fiber optic coil from the MIOC in order to eliminate an error occurring in the IFOG, these methods are not suitable for the use as they cause breakage or damage to the fiber during rework and because of the possibility of rendering the components unusable.

In addition to the studies of which their patent procedures have been completed, we have other studies of which their patent procedures are still going on. Our ongoing study is also related to improving the thermal performance of the fiber coil and the thermal performance of the IFOG in which the related fiber coil is used overall. This study explains the method of sandwiching the adhesive-free fiber pigtails of the fiber coil used for combining it with the MIOC to construct the IFOG. The method includes forming a thin layer of coating material with low modulus that can be cured with ultraviolet light on the radial surface of the fiber coil, winding the adhesive-free fiber pigtails between the fiber coil and the MIOC, applying the same coating material on the wound adhesive-free fibers, sandwiching and fixing them between the two layers of coating.

Although there are methods which includes buffer zones consisting of additional fiber layers that do not carry optical signals or buffers zones made of adhesives in order to enhance the thermal performance of the fiber coils, these buffer zones are used only to prevent or delay the penetration of heat into the fiber optic coil. These methods does not present any solution for the fixation of the adhesive-free fiber pigtails in between the fiber coil and the MIOC.

Creating a coating layer on the radial surface of the fiber coil and sandwiching the adhesive-free fiber pigtails of the fiber coil and the MIOC lowers the mechanical stress in between the fiber coil and the pigtails, it prevents the formation of different mechanical stress on the adhesion surface due to the fact that the adhesive used in the production of the fiber coil is different than the adhesive used to fix the adhesive-free pigtails under temperature changes. The fixability on the fiber optic coil is increased thanks to this method. The thermomechanical incompatibility between the fiber optic coil and the pigtails is reduced preventing the temperature-related errors and enhancing the rotation sensitivity of the IFOG in which the fiber coil is used.

This method is developed for the aim of producing a fiber optic coil and a MIOC package with improved performance by reducing temperature-dependent rotation sensitivity. It prevents sudden rotational deviations that may occur at random times and random amplitudes due to temperature changes in IFOGs. It further eliminates the inability to calibrate the IFOG by preventing those random errors that may occur. Using this method makes it possible to perform the separation process without damaging the fibers in cases where it is necessary to separate the fiber optic winding from the MIOC in order to eliminate an error occurring in the IFOG.

The rate vs temperature graphs obtained from the IFOGs built with the fiber optic coil and a MIOC package with and without using this method are given in Figure 4.24, 4.25, 4.26, and 4.27 respectively. Test 1 represents the data obtained from the IFOG in which this method is not used. As can be seen from the graphs, there are spikes in rate data with respect to temperature which degrade the performance of the system in total or make the system out of calibration. Test 2 represents the data obtained from the IFOG in which this method is used. As can be seen from these graphs, the use of this method eliminates the possibility of occurring sudden rate changes due temperature change and increases the thermal performance of the system. The patent procedure for this study is still going on.

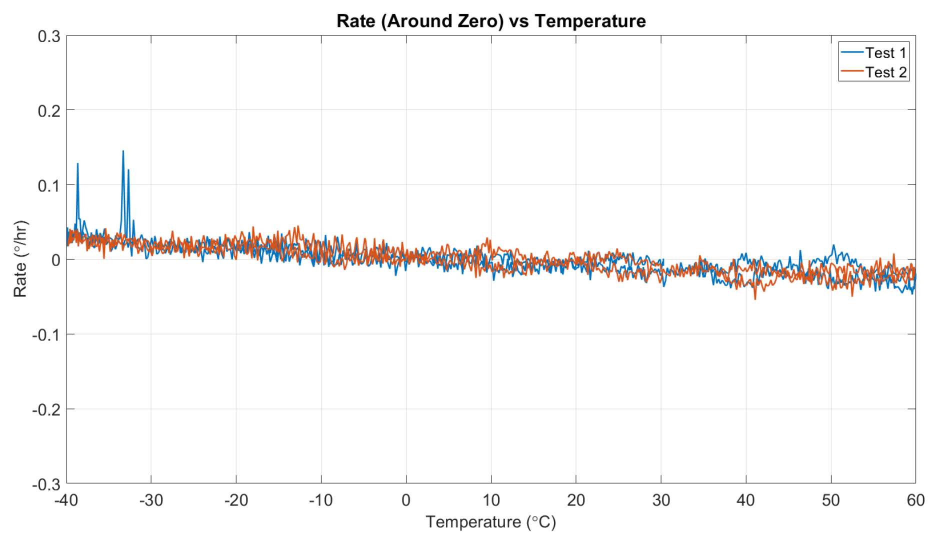

Figure 4.24: A comparison rate (around zero) vs temperature graph obtained from the IFOG built with and without the use of this method. Test 1 represents the data obtained without the use of the special method and test 2 represents the data obtained with the use of the special method. The use of this method eliminates the random spikes at the rate.

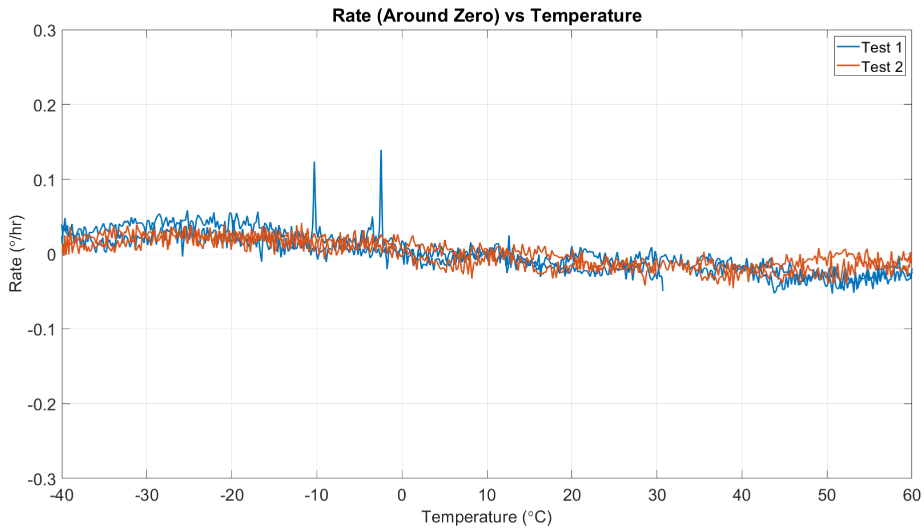

Figure 4.25: A comparison rate (around zero) vs temperature graph obtained from the IFOG built with and without the use of this method. Test 1 represents the data obtained without the use of the special method and test 2 represents the data obtained with the use of the special method. The use of this method eliminates the random spikes at the rate.

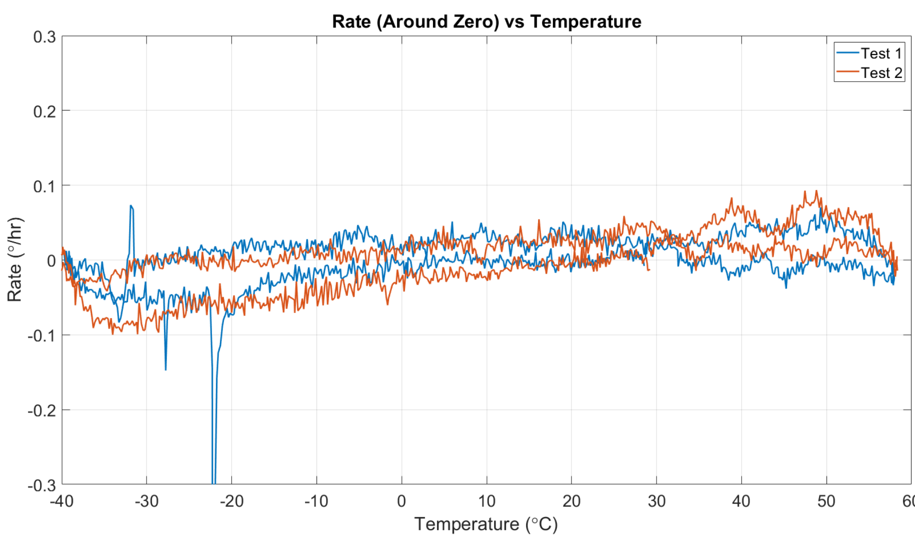

Figure 4.26: A comparison rate (around zero) vs temperature graph obtained from the IFOG built with and without the use of this method. Test 1 represents the data obtained without the use of the special method and test 2 represents the data obtained with the use of the special method. The use of this method eliminates the random spikes at the rate.

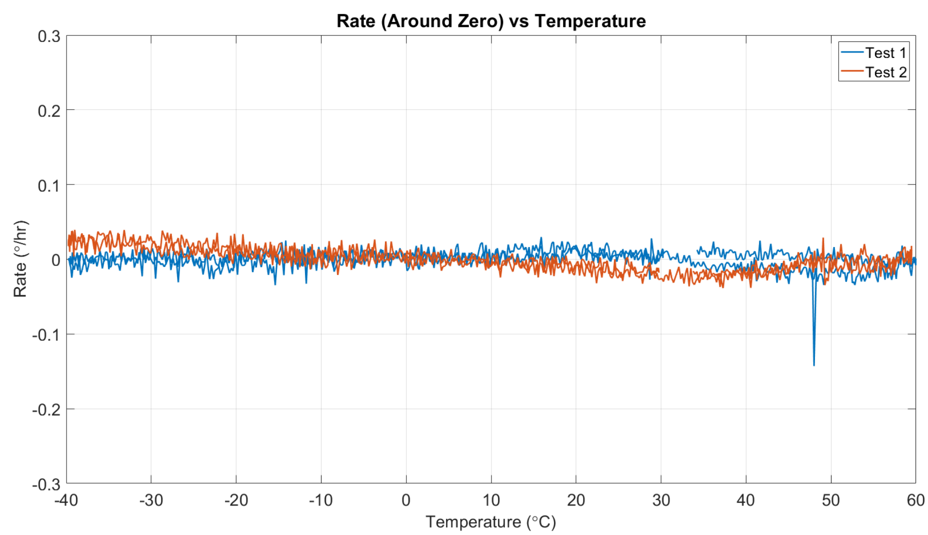

Figure 4.27: A comparison rate (around zero) vs temperature graph obtained from the IFOG built with and without the use of this method. Test 1 represents the data obtained without the use of the special method and test 2 represents the data obtained with the use of the special method. The use of this method eliminates the random spikes at the rate.

Chapter 5

Examining a Trimmed Hexadecapolar Fiber Sensing Coil Under Temperature Variations

5.1 Introduction

It is a well known fact that IFOGs are easily distorted by the thermal effects and the distortion results in degradation of the performance of these sensors. Changing the fiber coil geometry, increasing the winding symmetry and eliminating the need of trimming offer an alternative solution for preventing this degradation. This chapter investigates how different types of coil windings behave under different thermal rates and shows that hexadecapole winding pattern outperforms dipole, quadrupole and octupole winding patterns in the need of trimming both theoretically and experimentally even if tested under different temperature rates.

Here we study the thermal characteristics of fiber coils with different patterns theoretically and experimentally. We built up a numerical model and showed that the use of this winding method will help us to obtain the best thermal performance in an IFOG that consists of the respective fiber coil. We used the trimming method in addition to the usage of this special winding method for the very same purpose. We also verified the model experimentally with different rates of temperature change.

5.2 Symmetry in a Fiber Coil

As stated before, fiber coil works as the sensing element of an IFOG and carries the load of undesired nonreciprocal errors caused by the thermal and stress gradients along it.

One of the largest error sources in an IFOG is the Shupe Effect [11]. It occurs in the presence of time-varying spatial gradients arising from acoustic noise, vibration transients, thermal and stress perturbations across the fiber optic sensing coil. These perturbations cause a time-varying refractive index change along the fiber.

Luckily, there are some ways of minimizing these errors. For example, one can use special winding techniques in order to minimize the Shupe effect due to thermal transients. Moreover, the problems caused by the time-varying stress gradients can be reduced by cementing the fiber wraps in the coil [10].

Using symmetric winding techniques such as dipole, quadrupole, octupole or hexadecapole is one of the most common used techniques with a proven efficiency. It helps to reduce the nonreciprocity caused by the false rotation signal when the counter-propagating light waves encounter sections of fiber undergoing time-varying thermal gradients and no longer travel identical paths through the coil.

In symmetric winding, winding starts from the center of the optical fiber, shown with an arrow, supplied from two fiber supply spools each of which containing one-half of the full fiber length required for the whole fiber sensor coil as shown in Figure 5.1.

Special fiber winding machines are used to produce symmetrically wound fiber optic coils, because symmetric winding requires fiber optic layers to be wound in pairs which are at equal distance from the center of the coil. After the start of the winding, a precise pattern is followed in every turn and layer. Moreover, the tension applied to the

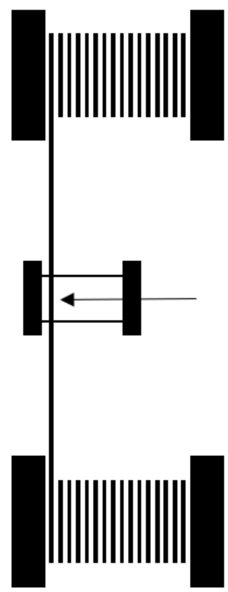

Figure 5.1: Schematic representation of how symmetric fiber winding starts. Fiber separated in two in length without any discontinuity to two fiber supply spools which become active alternately is wound on a product spool in symmetric winding.

fiber should be controlled and kept constant as much as possible during the winding. Each turn of the fiber should be in contact with the preceding and succeeding turn and each layer should lie in the grooves formed in between the two underlying fiber turns. The aim of using a symmetrical winding is to keep the counter propagating beams moving side by side as much as possible which means that they should encounter the same environmental effects at the same time and any faced environmental distortion should have a counter action which reduces the errors due to the reciprocity. That's why, IFOGs constructed with fiber coils having symmetric winding patterns are less prone to suffer from the temperature dependent errors.

There are several symmetric winding patterns. Let's use circles as the side views of the fiber to visualise this symmetric patterns and show how they look like. The clear and dark circles in Figure 5.2, Figure 5.3, Figure 5.4, and Figure 5.5 referring to dipole, quadrupole, octupole, and hexadecapole winding patterns respectively represent the fiber from two different supply spools. In these patterns, each layer pair begins with a fiber segment on the opposite side of the innermost layer from the preceding layer pair to position fiber segments an equal distance from the center. To put it more explicitly, after the first layer of any pair is wound, the winding direction reverses at the spool flange. The fiber wraps of the second layer of any pair lie in the grooves formed by the fiber wraps beneath, except at the fiber crossovers due to the reverse-winding fiber wraps moving one fiber diameter in the opposite direction. Alternating layer pairs are wound until the winding is complete. In dipole winding, pattern repeats itself in every two layers; in quadrupole winding, pattern repeats itself in every four layers; in octupole winding, pattern repeats itself in every eight layers; in hexadecapole winding, pattern repeats itself in every sixteen layers as the names suggest. During the winding, the sensor coil is potted in order to ensure a good coil ruggedness and minimize the errors caused by vibrations [9].

Figure 5.2: Schematic representation of dipole winding pattern. Clear and dark circles indicating the fiber turns fed from different supply spools repeat themselves in every two layers.

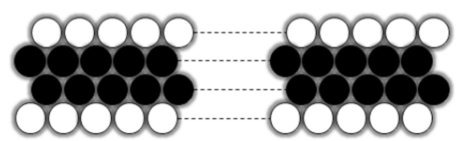

Figure 5.3: Schematic representation of quadrupole winding pattern. Clear and dark circles indicating the fiber turns fed from different supply spools repeat themselves in every four layers.

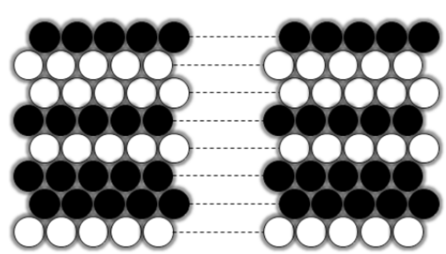

Figure 5.4: Schematic representation of octupole winding pattern. Clear and dark circles indicating the fiber turns fed from different supply spools repeat themselves in every eight layers.

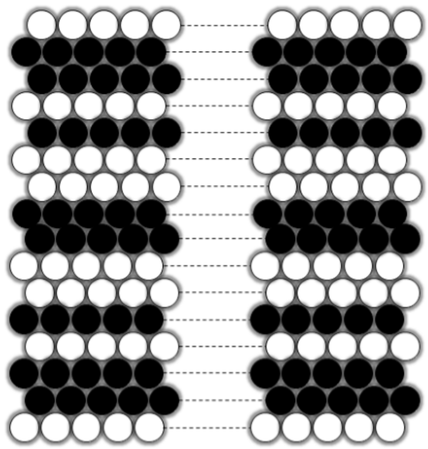

Figure 5.5: Schematic representation of hexadecapole winding pattern. Clear and dark circles indicating the fiber turns fed from different supply spools repeat themselves in every sixteen layers.

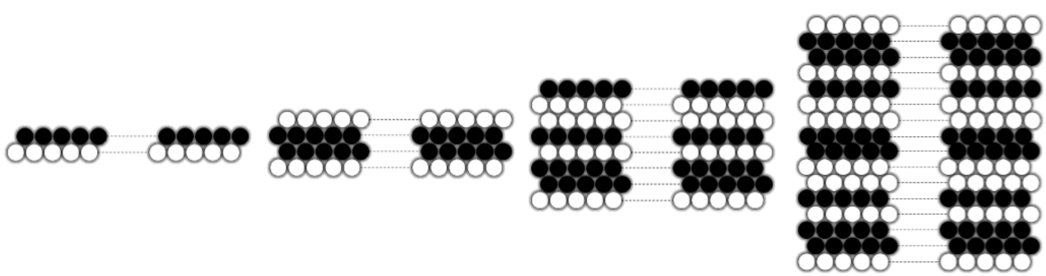

Figure 5.6: Schematic representation of dipole, quadrupole, octupole and hexadecapole winding pattern in ascending order. As the number of repeating layers increase, the symmetric pattern in the winding also increases.

Quadrupole winding is one of the most widely used techniques with proven performance [34]. It helps to reduce the nonreciprocity caused by the false rotation signal when the counterpropagating light waves do not follow the same paths through the fiber segments in the coil which are exposed to time-varying thermal gradients. However, since this winding model is no longer sufficient to meet the performance demands of the IFOGs, further work is required to increase the winding symmetry of the fiber coil and eventually improve the thermal performance of the IFOG. Changing the winding pattern form quadrupole to hexadecapole has a second string to bow. The hexadecapole winding technique is still an area that needs to be explored, unlike the quadrupole winding technique. Here in this chapter, we study the trimming method in addition to the usage of hexadecapole winding pattern which will help to obtain the better thermal performance of a fiber coil not only at a certain thermal rate but also at different rates. We support our experimental results theoretically as well.

5.3 Experimental Setup

In order to see how the gyroscope performance of fiber coils with different winding is affected by the temperature changes, we constructed an IFOG by splicing a three-in-one APE MIOC to the fiber coil which is also spliced to a broadband ASE light source with a central wavelength of 1550 nm coupled to a 3 dB optical coupler. APE MIOC was acting as $>$ 40 dB polarizer, a 3 dB coupler, and a phase modulator. We payed attention to the polarization and optic power consistency and check them in each step of all the splice procedures. Once the loop was completed, we implemented a photodetector to the system to convert the interfered optical signal. Tested coil was wound by using PM fiber with 80 µm cladding and 168 µm coating diameter on a spool with an average diameter of 85 mm. Only the fiber optic coil was packed and placed in the climatic chamber with a heat sensor in a magnetic shield to prevent nonreciprocal errors coming from magnetic field changes and tested over different temperatures. The photograph of the experimental setup is given in Figure 5.7.

We have started our tests by using fiber coil with dipole winding pattern at first and then repeated the tests with fiber coils having quadrupole, octupole, and hexadecapole

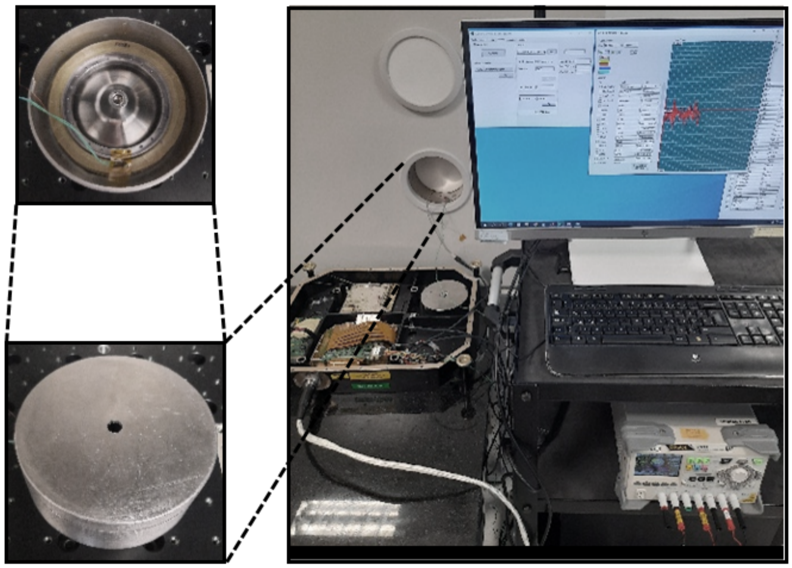

Figure 5.7: Photograph of the experimental setup. The tested fiber coil is placed in a climatic chamber with a heat sensor, rate data (around zero) and varying temperature data are read with the aid of a software.

winding patterns in turn. Each of which have the same number of layers of 48 and the same number of turns of 80 as stated before. We assessed the gyroscope performance of these coils between -40°C and +60°C operating temperature in a climatic chamber with 0.2°/min. rate. The rate data (around zero) are read with the aid of a software and presented as a function of temperature.

The fiber coil with dipole winding pattern shows 1.755°/h; the fiber coil with quadrupole winding pattern shows 0.356°/h; the fiber coil with octupole winding pattern shows 0.126°/h; and the fiber coil with hexadecapole winding pattern shows 0.021°/h absolute rate error experimentally when used in an IFOG. The corresponding graphs are given in Figure 5.8, Figure 5.9, Figure 5.10, and Figure 5.11 respectively.

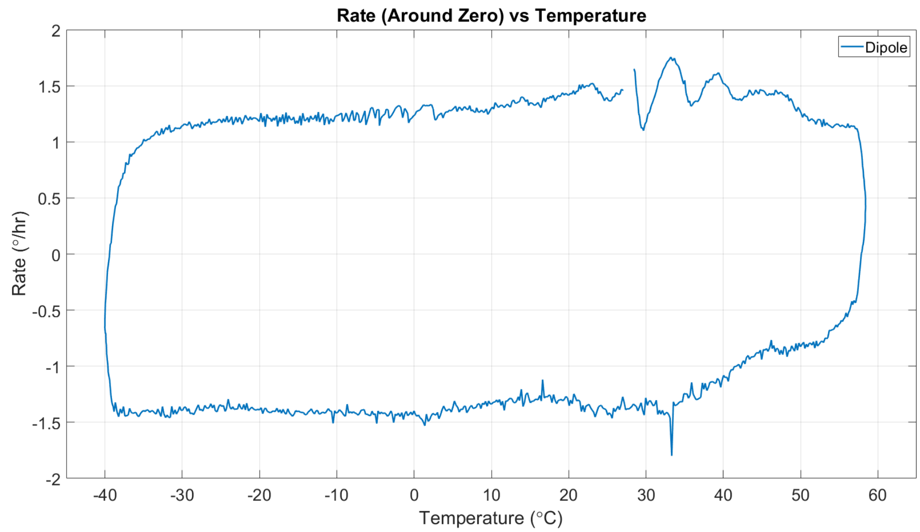

Figure 5.8: Rate (around zero) vs temperature graph of an IFOG comprising a fiber coil with dipole winding pattern.

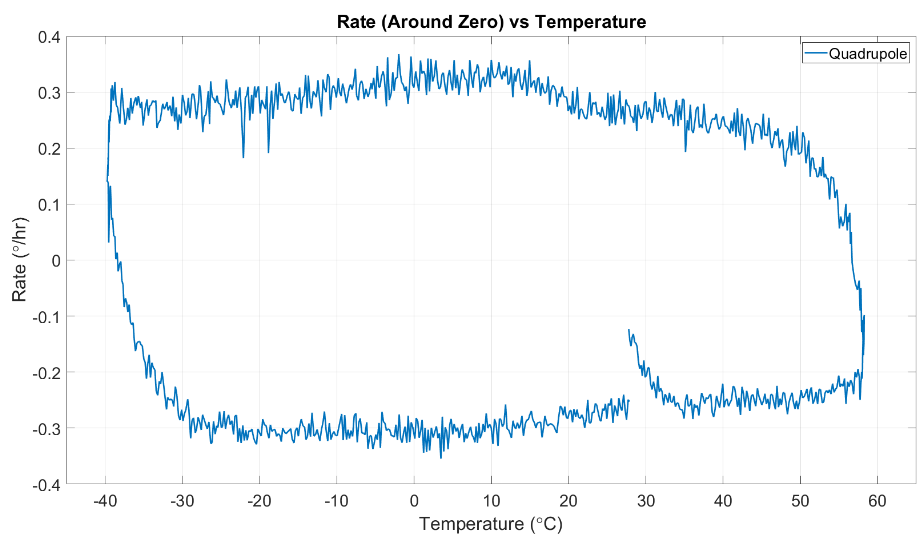

Figure 5.9: Rate (around zero) vs temperature graph of an IFOG comprising a fiber coil with quadrupole winding pattern.

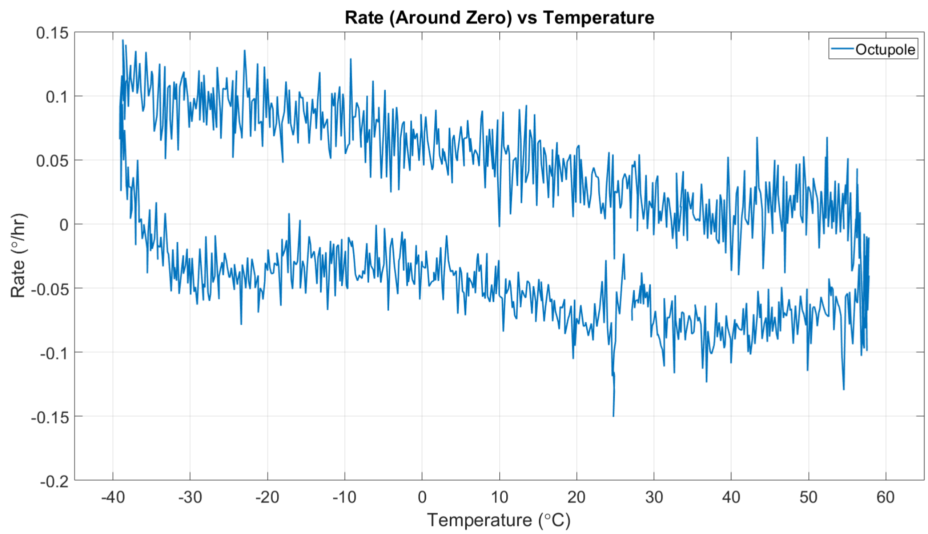

Figure 5.10: Rate (around zero) vs temperature graph of an IFOG comprising a fiber coil with octupole winding pattern.

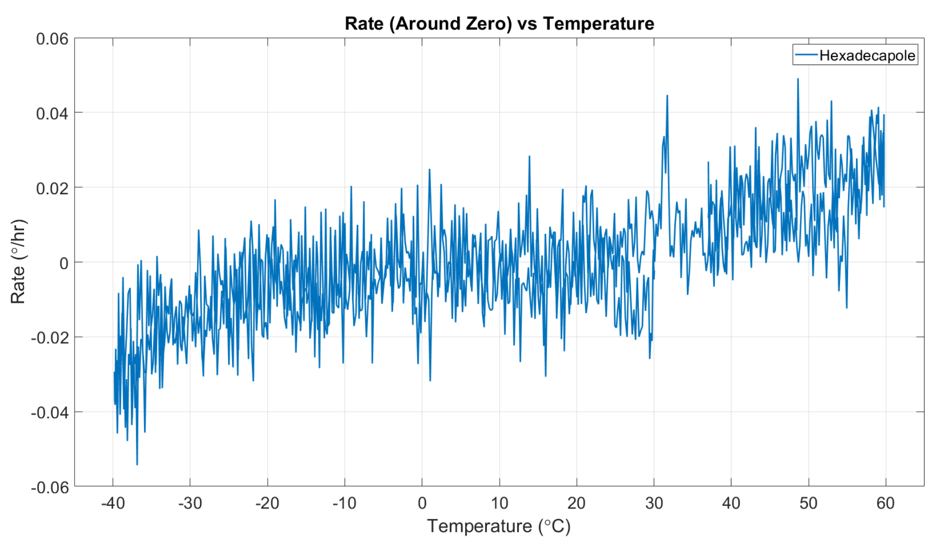

Figure 5.11: Rate (around zero) vs temperature graph of an IFOG comprising a fiber coil with hexadecapole winding pattern.

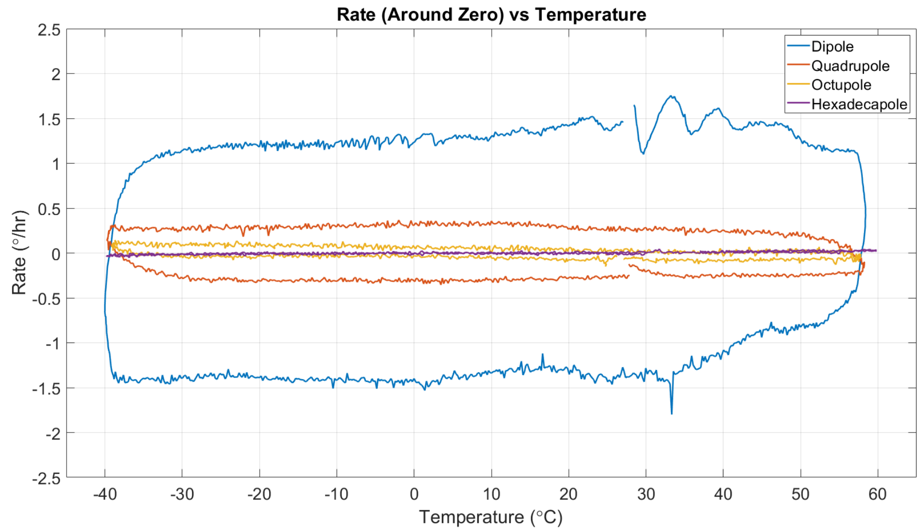

Figure 5.12: Comparison of the rate (around zero) vs temperature graphs of IFOGs comprising fiber coils with dipole, quadrupole, octupole, and hexadecapole winding patterns.

To sum up, Figure 5.6 shows the geometric illustrations of the portions of repetitive sections of the fiber coils with different winding patterns and Figure 5.12 the corresponding experimental results obtained from the IFOG comprising these fiber coils at a 0.2°C/min. rate of temperature change. In Figure 5.12 without trimming, 1.755, 0.356, 0.126, and 0.021°/h absolute rate errors were obtained from dipole (AB), quadrupole (ABBA), octupole (ABBABAAB) and hexadecapole (ABBABAABBAABABBA) winding patterns, respectively, at a 0.2°C/min. rate of temperature change, experimentally. The data here shows clearly the fact that the increase in the winding symmetry eventually results in the improvement of the thermal performance of the corresponding fiber coil used in the IFOG.

5.4 A Model to Analyze the Thermal Effects on a Fiber Coil

If a fiber coil experiences a temperature change over time, thermally triggered nonreciprocity arises because the two counter-propagating beams will pass through the same region of the coil at different times. The underlying reason for this effect is that when the fiber is exposed to thermal changes, the light propagation constant (β) in the fiber changes at different rates along the fiber.

Beams traveling uneven paths create undesirable nonreciprocal phase shifts along with the real phase shift coming from the rotation that is to be measured and by considering this phase shift, the angular error of thermally induced non-reciprocity for the IFOG can be calculated by [11]

$$\begin{aligned}\phi_{shupe}(t) = \quad & \frac{n_c}{4NA}(\frac{dn_c}{dT}+\alpha n_c)(\int_0^{L/2} dl(2l-L) \\ & \times[\Delta T(l,t)-\Delta T(l',t)]),\end{aligned} \tag{5.1}$$

where $n_c = 1.46$ is the refractive index of the fiber core, $N = 48$ is the number of turns in the coil, A is the area of the coil with a diameter of 10 cm, $dn_c/dT = 10^{-5}/°C$ is the temperature dependence of the refractive index of the fiber, $\alpha = 5x10^{-7}/°C$ is the coefficient of linear thermal expansion of fiberglass and $L = 1037m$ is the total length of the coil. Here, l and l' represent the locations of the two rotating beams at the same time and $\Delta T(l,t)$, and $\Delta T(l',t)$ represent the temperature differences between the locations l and l' simultaneously.

After the simplification for a coil which is symmetrically wound from its midpoint, the equation becomes

$$\begin{aligned}\phi_{shupe}(t) = \quad & \gamma\sum_{i=1}^{M/2}[\sum_{j=1}^{S}[\Delta T(A_{i,j},t)-\Delta T(B_{i,j},t)] \\ & \times\int_{(i-1)L/M/S}^{iL/M/S} dl(2l-L)],\end{aligned} \tag{5.2}$$

$$\gamma = \frac{n_c}{4NA}(\frac{dn_c}{dT}+\alpha n_c) \tag{5.3}$$

where $(A_{i,j},t)$ and $(B_{i,j},t)$ represent the clockwise and counterclockwise beam positions on the coil at the same time, $M = 48$ is the number of layers, and S is the number of dl section on each layer. This formula examines the temperature variations for each layer and each dl length corresponding to that layer. Here, since the 2D conduction thermal model is used for temperature distribution on the coil, S is taken as 80 and that also represents the number of turns for each layer of the fiber coil that is used in experiments.

With the numerical model that we built, we calculated the trimming lengths of the fiber coils with different winding patterns starting from dipole to hexadecapole first at 0.2°C/min. rate of temperature change and then at 4°C/min. rate of temperature change respectively.

When there is no trimming in a fiber coil wound with dipole winding pattern, we obtained 2.043°/h absolute rate error by numerically computing the results obtained based on the previous formula also shown in Figure 5.13.

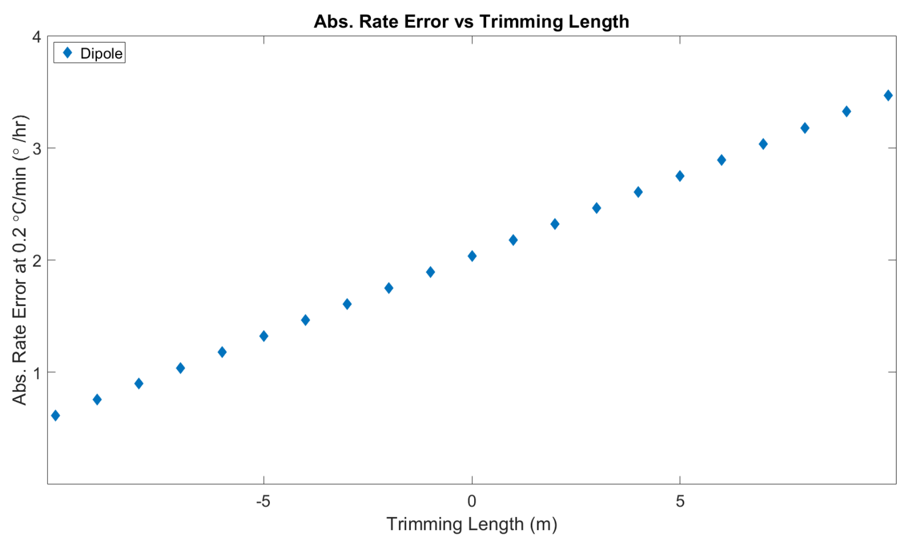

Figure 5.13: Absolute rate error vs trimming length graph of the IFOG comprising the fiber coil with dipole winding pattern at 0.2°C/min. rate of temperature change.

When there is no trimming in a fiber coil wound with quadrupole winding pattern, we obtained 0.353°/h absolute rate error by numerically computing the results obtained based on the previous formula also shown in Figure 5.14.

When there is no trimming in a fiber coil wound with octupole winding pattern, we obtained 0.100°/h absolute rate error by numerically computing the results obtained

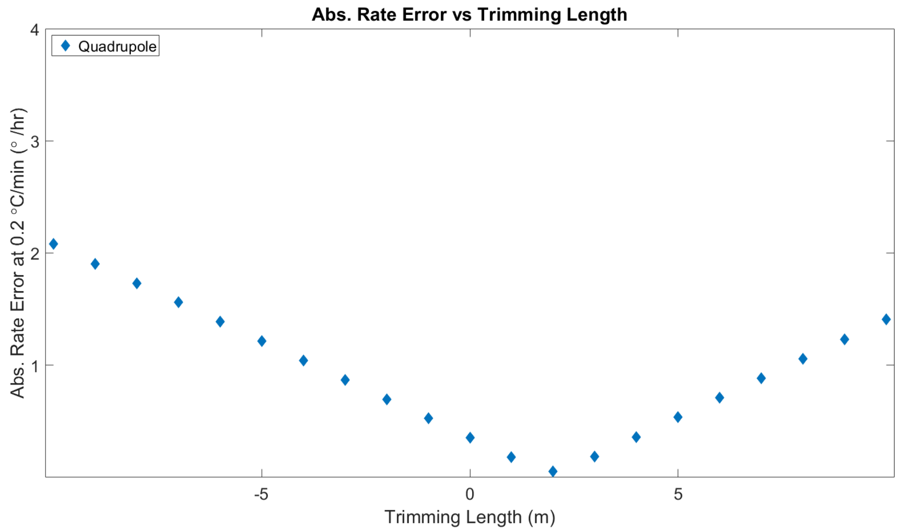

Figure 5.14: Absolute rate error vs trimming length graph of the IFOG comprising the fiber coil with quadrupole winding pattern at 0.2°C/min. rate of temperature change.

based on the previous formula also shown in Figure 5.15.

When there is no trimming in a fiber coil wound with hexadecapole winding pattern, we obtained 0.020°/h absolute rate error by numerically computing the results obtained based on the previous formula also shown in Figure 5.16.

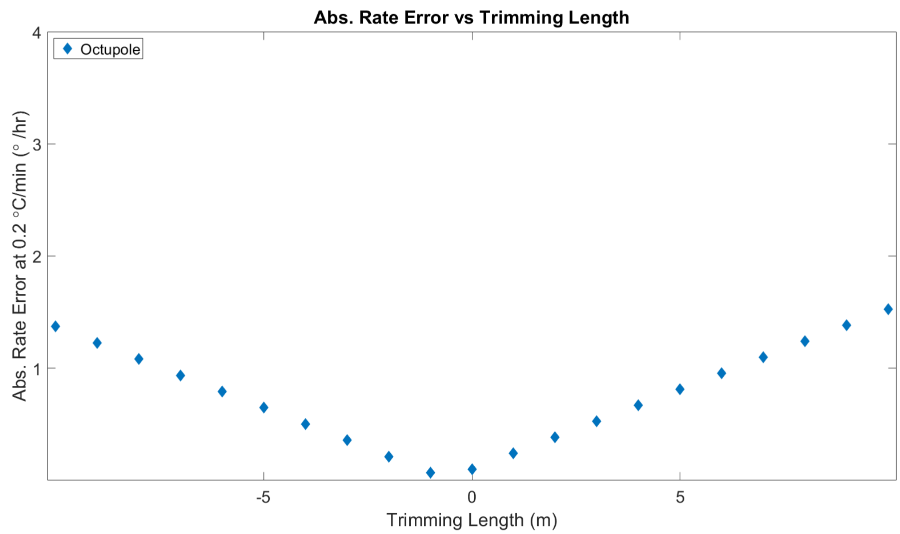

Figure 5.15: Absolute rate error vs trimming length graph of the IFOG comprising the fiber coil with octupole winding pattern at 0.2°C/min. rate of temperature change.

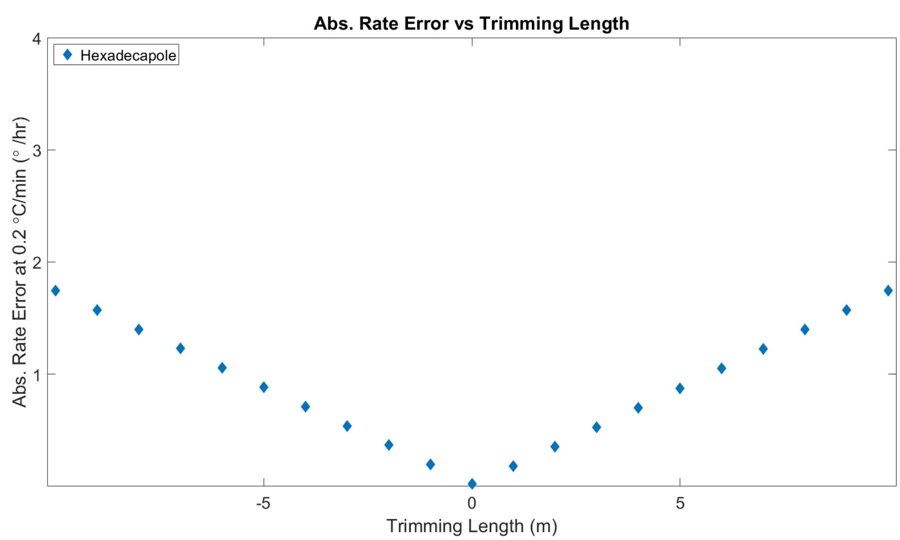

Figure 5.16: Absolute rate error vs trimming length graph of the IFOG comprising the fiber coil with hexadecapole winding pattern at 0.2°C/min. rate of temperature change.

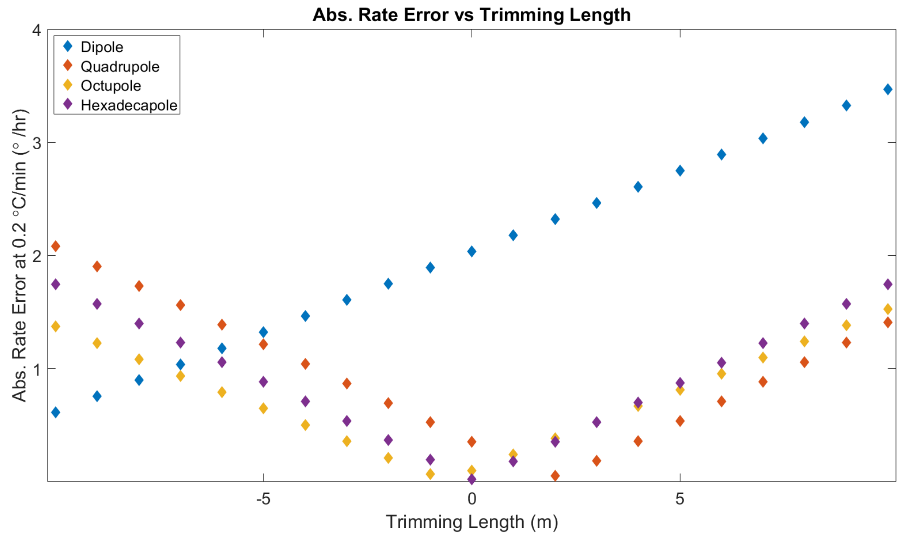

Figure 5.17: Absolute rate error vs trimming length graph of the IFOG comprising the fiber coils with different winding patterns at 0.2°C/min. rate of temperature change.

To summarize, Figure 5.17 shows the trimming needs obtained from the calculations at 0.2°C/min. rate of temperature change. 2.043, 0.353, 0.100, and 0.020°/h absolute rate errors were also obtained numerically computing the results obtained from each pattern showing a good agreement with the experiments. As can be seen here, the need of trimming gradually decreases as the symmetry of the fiber coil winding increases. It was observed that the hexadecapole pattern outperforms the others in terms of the need for trimming as it presents approximately 100, 15, and 5 times reduced absolute rate error than dipole, quadrupole, and octupole pattern when tested under a 0.2°C/min. rate of temperature change for both simulations and experiments.

We expanded our studies by increasing the rate of temperature change from 0.2 up to 4°C/min. and recalculate the absolute rate errors for each fiber coils with different winding patterns.

When there is no trimming in a fiber coil wound with dipole winding pattern, we obtained 23.81°/h absolute rate error by numerically computing the results obtained based on the previous formula also shown in Figure 5.18.

When there is no trimming in a fiber coil wound with quadrupole winding pattern, we obtained 6.57°/h absolute rate error by numerically computing the results obtained

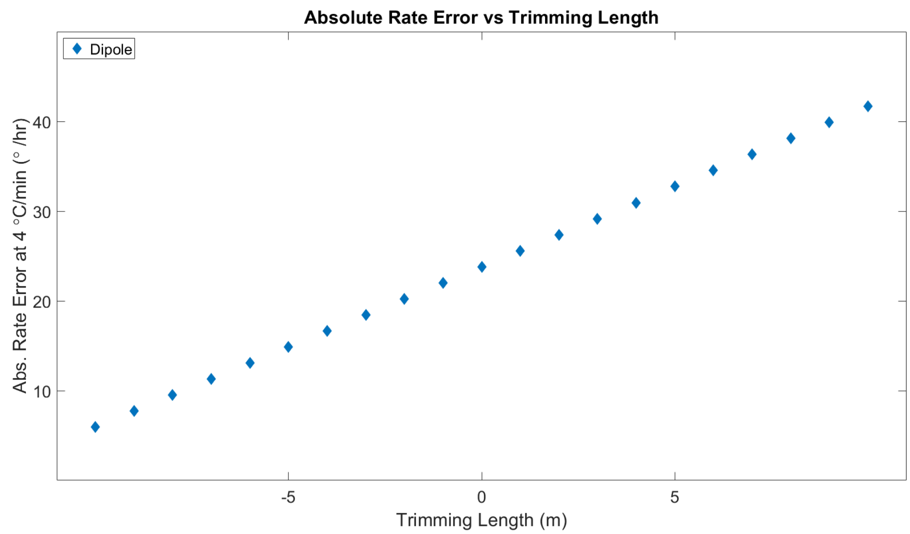

Figure 5.18: Absolute rate error vs trimming length graph of the IFOG comprising the fiber coil with dipole winding pattern at 4°C/min. rate of temperature change.

based on the previous formula also shown in Figure 5.19.

When there is no trimming in a fiber coil wound with octupole winding pattern, we obtained 2.30°/h absolute rate error by numerically computing the results obtained based on the previous formula also shown in Figure 5.20.

When there is no trimming in a fiber coil wound with hexadecapole winding pattern, we obtained 0.77°/h absolute rate error by numerically computing the results obtained based on the previous formula also shown in Figure 5.21.

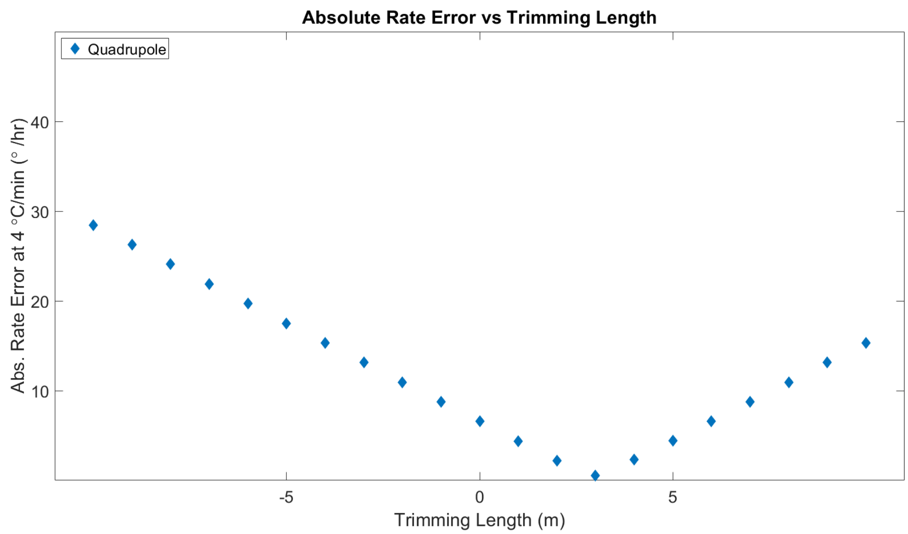

Figure 5.19: Absolute rate error vs trimming length graph of the IFOG comprising the fiber coil with quadrupole winding pattern at 4°C/min. rate of temperature change.

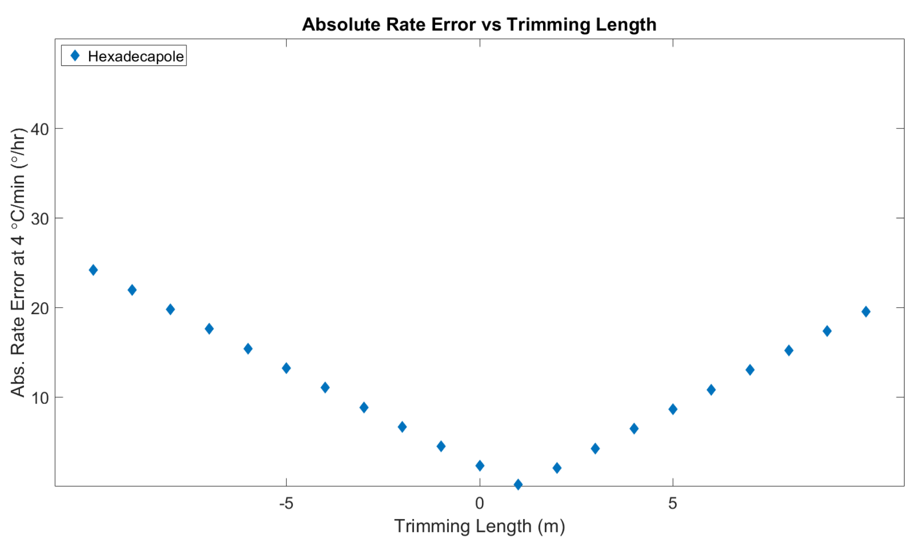

Figure 5.20: Absolute rate error vs trimming length graph of the IFOG comprising the fiber coil with octupole winding pattern at 4°C/min. rate of temperature change.

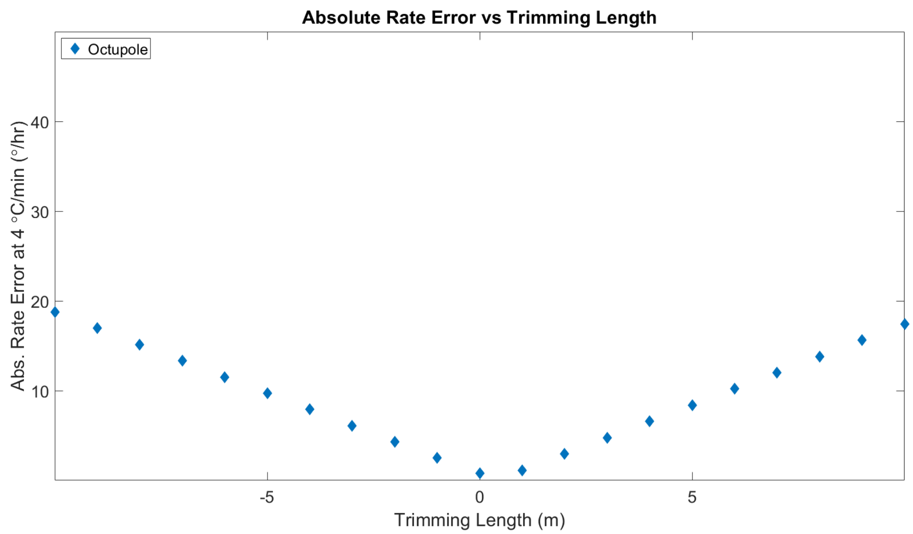

Figure 5.21: Absolute rate error vs trimming length graph of the IFOG comprising the fiber coil with hexadecapole winding pattern at 4°C/min. rate of temperature change.

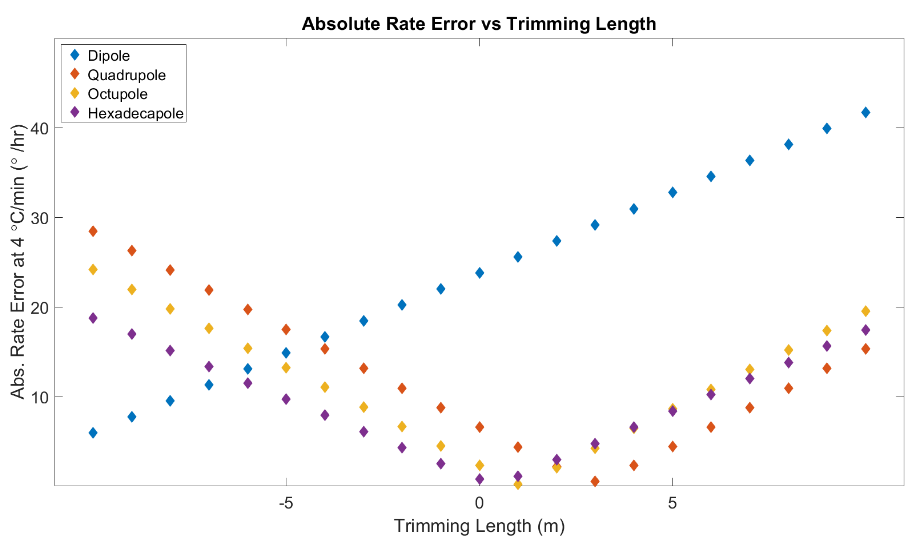

Figure 5.22: Absolute rate error vs trimming length graph of the IFOG comprising the fiber coils with different winding patterns at 4°C/min. rate of temperature change.

To summarize, Figure 5.22 shows the trimming needs obtained from the calculations at 4°C/min. rate of temperature change. 23.81, 6.57, 2.30, and 0.77°/h absolute rate errors were also obtained numerically computing the results obtained from each pattern. As can be seen here also, the need of trimming gradually decreases as the symmetry of the fiber coil winding increases. It was observed that the hexadecapole pattern outperforms the others in terms of the need for trimming when tested under also a 4°C/min. rate of temperature change.

5.5 Trimming as a Way of Restoring the Symmetry in a Fiber Coil

Although it was attempted to keep the winding method as symmetrical as possible, the nature of the fiber winding has a catch to it. Inevitable errors that come with the process itself such as the stress applied to the fiber during the winding, the change of the fiber length with temperature, the impurities, inhomogeneities, or the change of refractive index along the fiber [35] are always there. That is why, even if it is sought to produce a symmetrically wound fiber optic coil, the thermal performance of the fiber coil may still need to be improved at the end. Trimming is offered here as an auxiliary method to overcome this problem by basically shifting the midpoint of the fiber coil by adding or trimming a certain portion of the fiber ends [36]. In such a case, trimming shifts the midpoint of the fiber coil as $l_{eff}/2$ [37]. Then, the total angular error of thermally induced nonreciprocity including the asymmetry coming from this shift of the coil's midpoint can be calculated as

$$\begin{aligned}\phi_{shupe}(t) = \quad & \gamma\Bigg\{\sum_{i=1}^{M/2}[\sum_{j=1}^{S}[\Delta T(A_{i,j},t)-\Delta T(B_{i,j},t)] \\ & \times \int_{(i-1)L/M/S+\frac{l_{eff}}{2}}^{iL/M/S-\frac{l_{eff}}{2}} dl(2l-L)] \\ & + \sum_{i=1}^{M/2-1}[\sum_{j=1}^{S}[\Delta T(A_{i,j},t)-\Delta T(B_{i,j},t)] \\ & \times \int_{iL/M/S-\frac{l_{eff}}{2}}^{iL/M/S+\frac{l_{eff}}{2}} dl(2l-L)]\Bigg\} \qquad (5.4)\end{aligned}$$

The heat transfer method is used for a fixed coil geometry, material, and temperature profile to find ΔT. We use the explicit model of unsteady-state equation discretization by using a constant thermal diffusivity $\alpha = 5x10^{-9}m^2/s$ for fiberglass to calculate the temperature change in time [38].

$$\frac{\delta T}{\delta t} = \alpha(\frac{\delta^2 T}{\delta x^2} + \frac{\delta^2 T}{\delta y^2}) \qquad (5.5)$$

After the discretization of the equation, it becomes

$$\frac{T_M^{n+1} - T_M^n}{\Delta t} = \alpha(\frac{T_L - 2T_M + T_R}{\delta x^2} + \frac{T_T - 2T_M + T_B}{\delta y^2}) \qquad (5.6)$$

$$\{T_M^{n+1} = T_M^n + k_1(T_L - 2T_M + T_R)^n + k_2(T_T - 2T_M + T_B)^n\} \qquad (5.7)$$

where $k_1 = \alpha\Delta t/\Delta x^2$ and $k_2 = \alpha\Delta t/\Delta y^2$, T_L, T_T, T_M, T_B, T_R represent left, top, middle, bottom, and right boundary respectively if the conductivity $k_{1,2}$ were to be constant over the region.

The graphs of the rate of temperature changes inside the coil for 0.2°C/min. and 4°C/min. were also given in Figure 5.23 and Figure 5.24 with dashed lines.

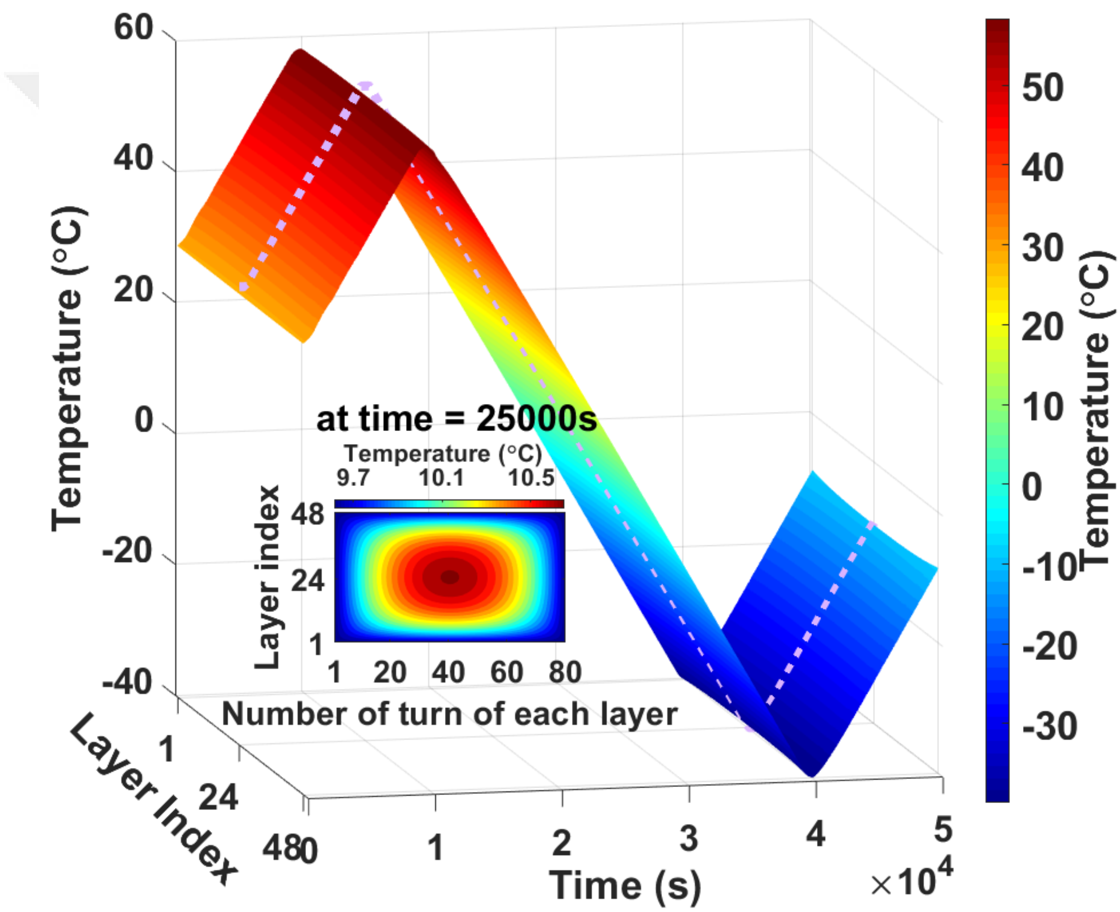

Figure 5.23: Temperature distribution curves on each layer of the fiber coil with respect to time at rate of temperature change 0.2°C/min. and heat transfers of the layers with respect to the number of turns of each layer at certain times. 0.2°C/min. rate of temperature change does not cause a dramatic difference between the set temperature and the temperature felt by the fiber coil.

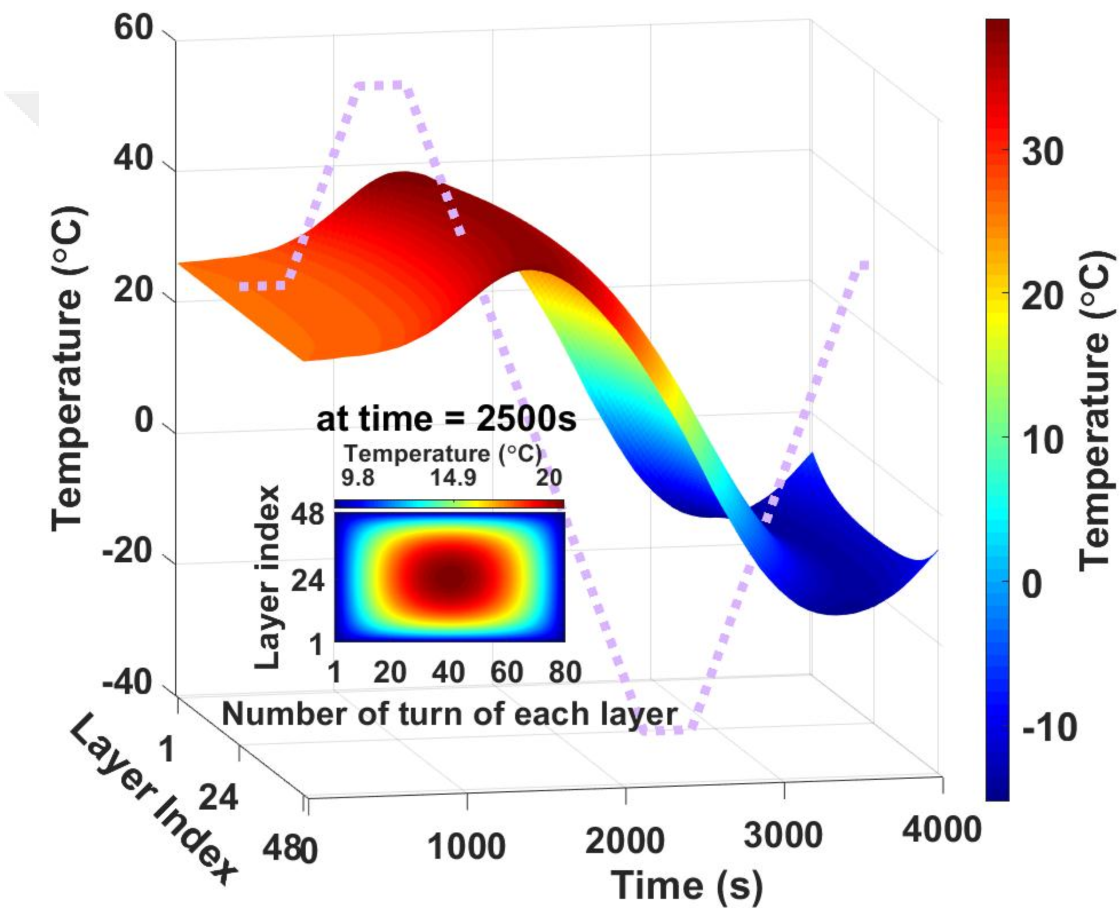

Figure 5.24: Temperature distribution curves on each layer of the fiber coil with respect to time at rate of temperature change 4°C/min. and heat transfers of the layers with respect to the number of turns of each layer at certain times. When the rate of temperature change increases up to 4°C/min., the fiber coil no longer feels the temperature properly and the temperature difference between the coldest and the hottest point of the fiber coil increases.

Figure 5.23 and Figure 5.24 show the temperature distributions on each layer of the fiber coil with respect to the time and layer index at different rates of temperature change. Dashed lines indicate the set temperature of the climatic chamber where the fiber coil is tested. The cross-sections of the layers and turns of the fiber coil at certain times are also given as a function of temperature. While the rate of temperature change is low, e.g., 0.2°C/min., the set temperature and the temperature felt by the coil almost match and the temperature difference between the coldest and the hottest point of the fiber coil becomes 1.1°C at t=25000s. However, when we increase the rate of the temperature change up to 4°C/min., the set temperature is no longer felt by the fiber coil properly and the temperature difference between the coldest and the hottest point of the fiber coil becomes 10.5°C at t=2500s. The temperature variation itself among the layers also varies upon different rates of temperature change.

We kept on studying with a fiber coil with hexadecapole winding pattern which is trimmed in one branch by 10 meters. We have conducted tests by using this coil under 0.2, 1, and 4°C/min. rates of temperature changes. The temperature vs time graphs recorded from the sensor on the tested fiber coil are given in Figure 5.25, Figure 5.26, Figure 5.27 respectively.

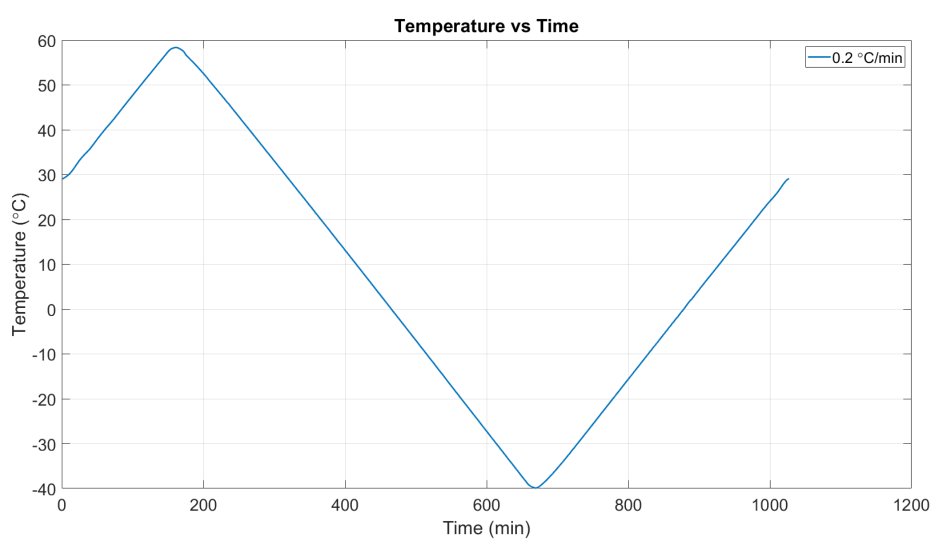

Figure 5.25: Temperature vs time graph recorded from the sensor on the fiber coil tested under 0.2°C/min. rate of temperature change.

Although same temperature range between -40 and +60°C was swept during the

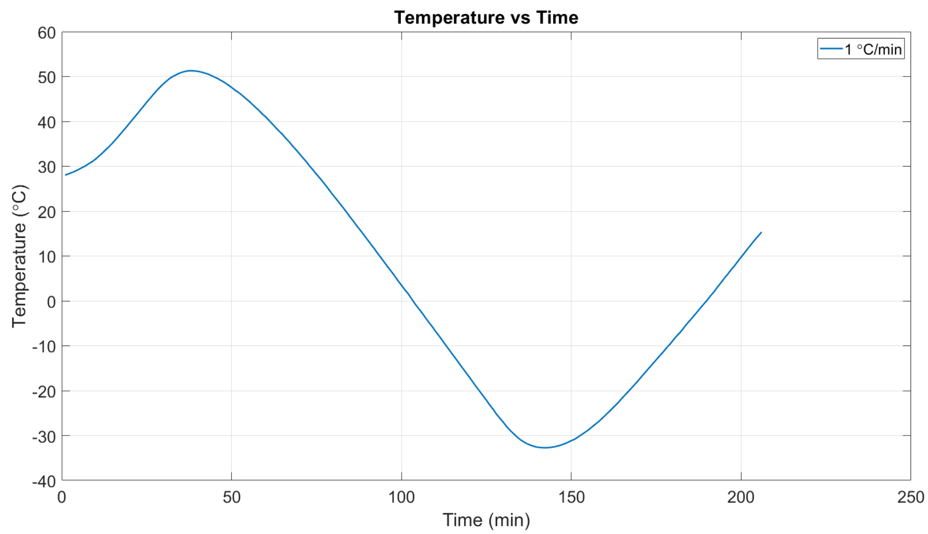

Figure 5.26: Temperature vs time graph recorded from the sensor on the fiber coil tested under 1°C/min. rate of temperature change.

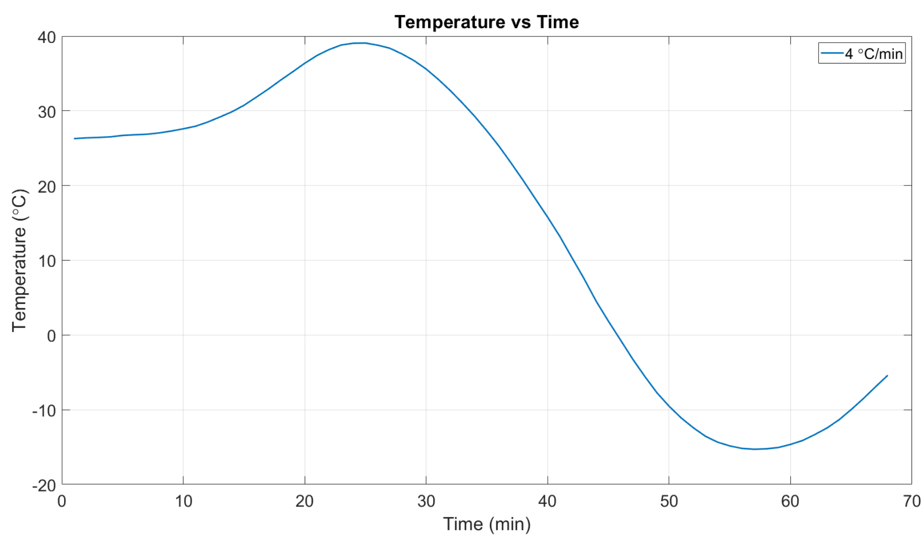

Figure 5.27: Temperature vs time graph recorded from the sensor on the fiber coil tested under 4°C/min. rate of temperature change.

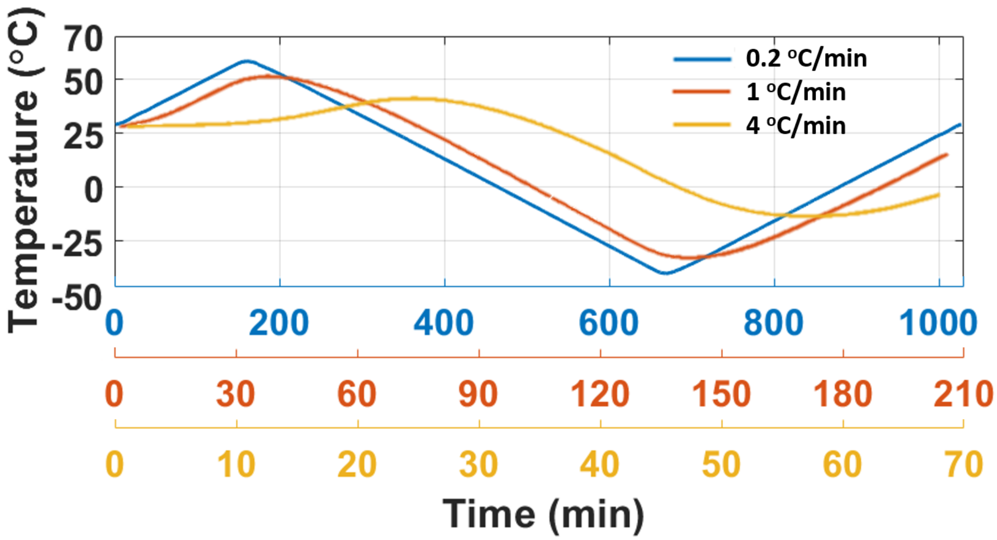

Figure 5.28: Comparison of the temperature vs time graphs recorded from the sensor on the fiber coil tested under 0.2, 1, and 4°C/min. rates of temperature change.

tests conducted with 0.2, 1, and 4 °C/min. rate of temperature changes; the temperature felt by the fiber coil was not reaching the lower and upper limits of this range due the difference in the rate of temperature changes. The time needed for temperature to diffuse in the fiber coil was also changing accordingly and increasing with the increased rate of temperature change as shown in Figure 5.28.

We have extended our studies on understanding the thermal behaviour of the 10 m trimmed hexadecapole fiber coil as well. We continued the experiments by following the same experimental setup under the same rate of temperature changes and observed how absolute rate error changes with respect to temperature. In addition to the experiments, we have simulated the correlated data theoretically with the thermal model that we introduced in the beginning of the chapter. Both the experimental results and the simulations match with each other as can be seen in Figure 5.29, Figure 5.30, and Figure 5.31 for 0.2, 1 and 4 °C/min. rate of temperature changes respectively.

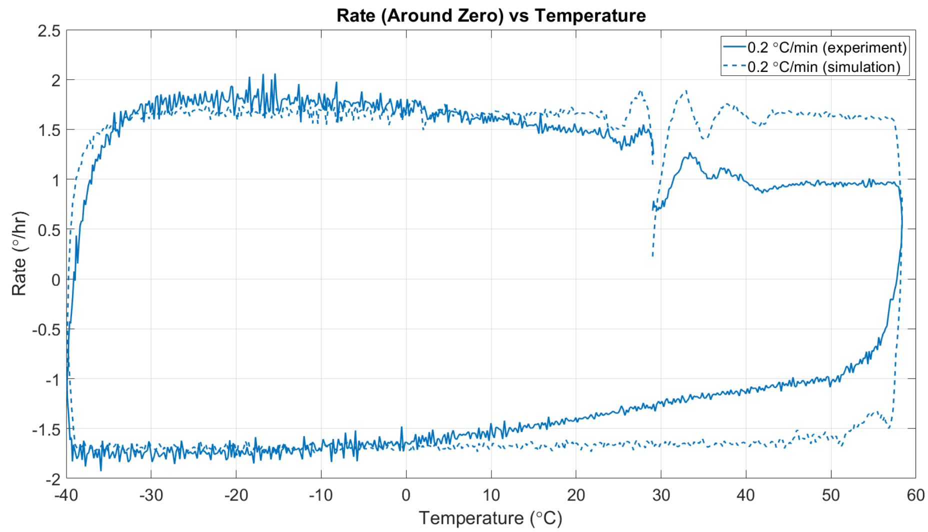

Figure 5.29: Comparison of the rate data (around zero) of the IFOG comprising the fiber coil with the hexadecapole pattern with 0.2 °C/min. rate of temperature change obtained from experiments (solid lines) and simulations (dashed lines) at a 10 m trimming length.

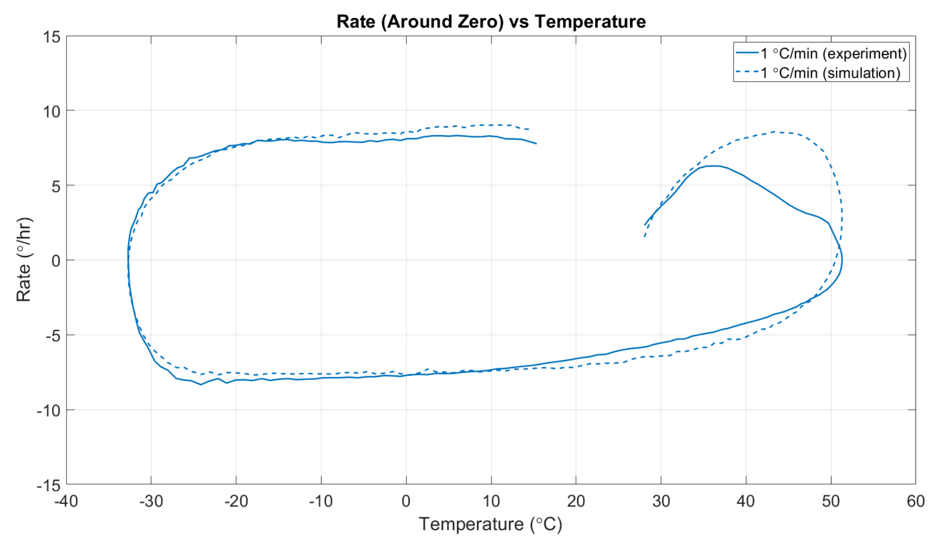

Figure 5.30: Comparison of the rate data (around zero) of the IFOG comprising the fiber coil with the hexadecapole pattern with 1 °C/min. rate of temperature change obtained from experiments (solid lines) and simulations (dashed lines) at a 10 m trimming length.

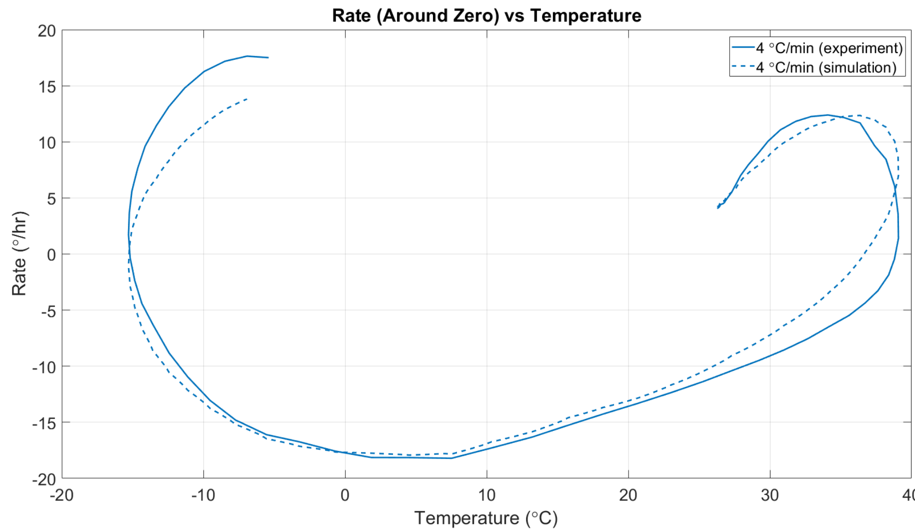

Figure 5.31: Comparison of the rate data (around zero) of the IFOG comprising the fiber coil with the hexadecapole pattern with 4 °C/min. rate of temperature change obtained from experiments (solid lines) and simulations (dashed lines) at a 10 m trimming length.

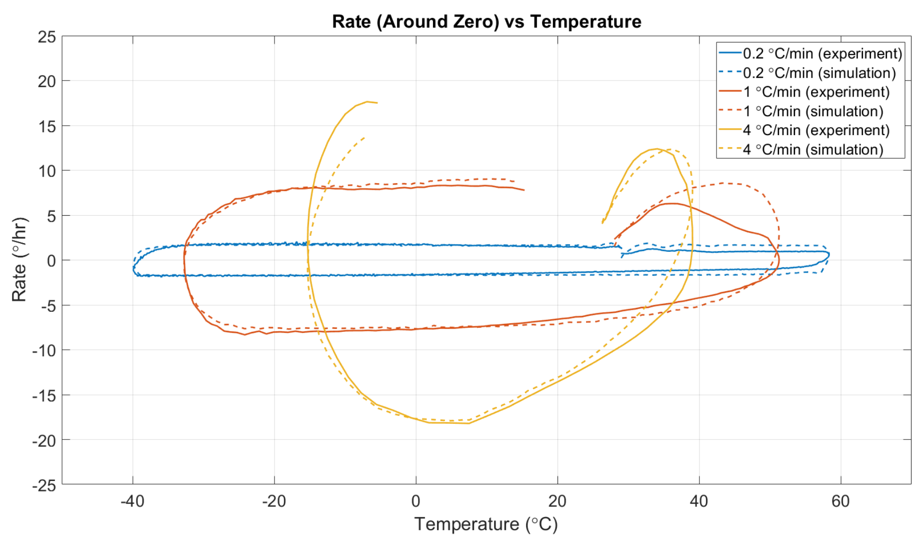

Figure 5.32: Comparison of the rate data (around zero) of the IFOG comprising the fiber coil with the hexadecapole pattern with 0.2, 1, and 4 °C/min. rate of temperature change obtained from experiments (solid lines) and simulations (dashed lines) at a 10 m trimming length.

All in all, Figure 5.32 shows the experimental and simulated absolute rate errors at three different rates of temperature change of 0.2, 1, and 4°C/min. at 10 m trimming length. 1.704°/h absolute rate error was measured at a rate of 0.2°C/min. temperature change with both experiments and simulations. 8.239°/h and 9.007°/h at a rate of 1°C/min., 17.99°/h and 18.15°/h at a rate of 4°C/min. temperature change with experiments and simulations, respectively.

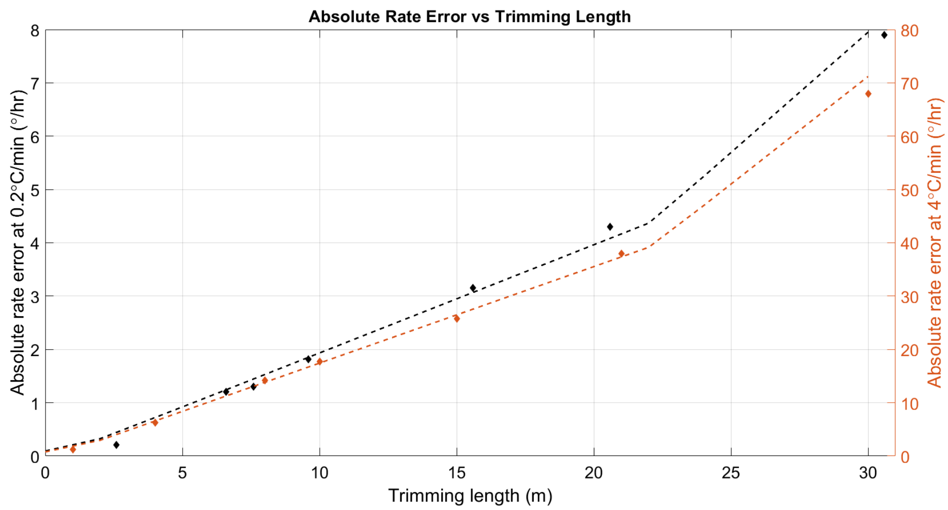

Figure 5.33: Comparison of the experimental (dots) and simulated (dashes) absolute rate errors at the rates of temperature change of 0.2°C/min. and 4°C/min. with respect to the trimming length.

The agreement of the simulated and experimental results at different rates of temperature changes supports the reliability of the thermal model that we used. Based on this, we investigated the effect of the trimming length of the fiber coil on the absolute rate error. We kept conducting the follow up experiments by changing the position of the middle of the same fiber coil by applying trimming at certain lengths and obtained the absolute rate error with respect to the trimming length that we applied at both 0.2°C/min. and 4 °C/min. rate of temperature changes. The relation between the absolute rate errors with respect to the trimming length of the fiber coil at different rates of temperature change is given in Figure 5.33. 0.023°/h absolute rate error was obtained with simulations indicated with dashed lines and 0.024°/h absolute rate error was obtained experimentally indicated with dots at the rate of temperature change of 0.2°C/min. Likewise, 0.023°/h absolute rate error was obtained with simulations and 0.035°/h absolute rate error was obtained experimentally at a rate of temperature change of 4°C/min. showing a good agreement with each other. In order to obtain these results, we still need to find and adjust the perfect trimming amount on the fiber coil at the order of 10 cm length. There, the trimming length is directly proportional to the absolute rate error. Therefore, increasing the trimming length in such coils worsens the thermal performance of the IFOG comprising the corresponding fiber coil as it increases the absolute rate error. In addition to this, as shown in Figure 5.33, there is a clear slope difference between shorter and longer trimming lengths at about 20 m and that is because the trimming length is longer than about 20 m that is longer than one layer of the coil that is used in the setup, causing a change in the symmetry of the hexadecapole pattern.

Although we have showed that the hexadecapole winding pattern has the upper hand over the other winding patterns mentioned above against temperature regarding the absolute rate error and the need of trimming is less for this winding pattern than the others shown both experimentally and theoretically; we still need to fine tune the trimming on the fiber coil and carefully adjust the right length in order to obtain better thermal performance on the IFOG in which we want to use the corresponding fiber coil. For this reason, we are still way beyond the finish line to have a better system that has improved bias stability as a function of temperature. This aim leads us to the next chapter.

Chapter 6

A Novel Method to Eliminate the Symmetry Dependence of Fiber Coils for Shupe Mitigation

6.1 Summary

It is a well-known fact that interferometric fiber optic gyroscopes (IFOGs) are easily distorted by thermal effects and distortion results in the degradation of the performance of these sensors. Changing the fiber coil geometry, increasing the winding symmetry, adding fiber buffer layers around the fiber coil, using different modulation methods for multifunctional integrated optic chips (MIOCs), and using special types of fibers, such as photonic crystal fibers (PCFs), are some alternative solutions for preventing this degradation. Here in this chapter, we theoretically and experimentally, investigate not only how different types of fiber coil winding methods behave under different rates of temperature change but also present a novel method, to the best of our knowledge, to eliminate the Shupe effect, without violating the simplest IFOG scheme. This method rules out the importance of the winding symmetry epochally and the need of any extra treatment for the fiber coil to increase the thermal performance of the system. Regardless of the symmetry of the fiber coil winding, the rate error due to the Shupe effect

can be reduced to about $\pm 0.05^\circ/\mathrm{h}$ for any rate of temperature change with this new method according to the experimental results.

6.2 Introduction

Applications, such as guidance, navigation, and control systems in air and land vehicles, both in industry and military fields, require compact, cost-effective, and reliable inertial navigation systems equipped with a highly sensitive gyroscope that uses the Sagnac Effect [1]. The effect that Sagnac unearthed led to the advent of IFOG with improvements of low-loss optical fibers, as well as solid-state semiconductor light sources and detectors [5]. Moreover, the fact that IFOGs are solid-state devices and have no moving parts, the ease of achieving higher sensitivity by increasing the number of wraps in the fiber coil used [16], their tendency for miniature manufacturing [39], long lifetime [10], very quick turn-on time [10], high reliability [16, 17, 40] and high precision are just some of the advantages that have ensured their outdistancing the other types of gyroscopes, e.g., ring laser gyroscopes (RLGs) [9, 10, 17, 41].

An ideal IFOG should be able to only measure the Sagnac phase shift. However, the Sagnac effect is not the only source of measurable phase shift in practice. Environmental effects such as temperature [11], magnetic field [12, 42], or vibration [13] create differences in the optical paths and can cause some undesired nonreciprocal phases apart from the Sagnac phase shift. Reducing these nonreciprocal errors brought on by environmental influences becomes essential due to the difficulty in differentiating between the real Sagnac phase shift and other nonreciprocal phase shifts. The effectiveness of this reduction ultimately dictates the quality of these fiber optic rotation sensors.

As the sensing element of the system, the fiber coil takes the lead in affecting its performance. In particular, the thermal sensitivity of the fiber coil reveals the sensitivity of the IFOG. Special winding methods have been proposed to overcome this performance limitation [34, 43, 44, 45]. The quadrupole winding pattern is one of the most widely used techniques with proven performance [34]. It helps to reduce the non-reciprocity caused by the false rotation signal when the counter-propagating light waves do not follow the same paths through the fiber segments in the fiber coil exposed to a different rate of temperature changes. However, quadrupole winding pattern fails to satisfy the performance needs of IFOGs any more. Therefore, more effort should be made for increasing the symmetry of the fiber coil and obtain thermally improved performance of the IFOG[46]. Apart from the winding methods, mechanical studies [47] and different modulation techniques [48, 49] have also been carried out to reduce the temperature effects. Using special types of fibers such as photonic crystal fibers (PCFs) in fiber coils to decrease the temperature dependency of the refractive index is also offered as an alternative to solve the problems caused by the environmental effects on IFOGs [50].

In this chapter, we study the rate errors due to the thermal characteristics of different types of fiber coils both theoretically and experimentally. We bring in the trimming method in addition to the usage of different winding methods for the very same purpose. We verify the model experimentally as well with different rates of temperature change. Furthermore, in noticing the rate error due to the Shupe effect behaving independently in the direction of the real rotation during the temperature analyses, we developed a novel method in which the Shupe effect can be easily measured and integrated into the IFOG systems independent of temperature variation and fiber coil winding symmetry.

The angular error of thermally induced non-reciprocity for the IFOG including the undesirable phase shifts created by the beams travelling uneven paths and the real phase shift coming from the rotation that is to be measured is already given in Chapter 5 by Eqn. (5.1). The simplified version of the equations, as the simulated and experimental works of thermal effects for the winding methods of four different fiber coils (dipole (AB), quadrupole (ABBA), octupole (ABBABAAB), and hexadecapole (ABBABAABBAABABBA)), are presented in Chapter 5 as well.

6.3 The Independency of Shupe Effect on the Direction of the Real Rotation

As seen in Eqn. (5.2) and Eqn. (5.3), the rate error due to the Shupe effect is an absolute error that is independent of the direction of the real rotation. The phenomenon of the Shupe effect being independent of real rotation allows us to easily calculate the rate error due to this effect by simply reversing the fiber coil axis horizontally, such as changing its axis from the +x to the -x. By considering a constant rotation such as the Earth's rotation applied to the system; the total phase shifts for the +x and -x axes can be shown as in Eqs. (6.1) and (6.2), respectively. When these phase shifts are added up to each other as shown in Eqn. (6.3), the twofold pure rate error due to the Shupe effect can be easily found.

$$\phi_{total}^{+x} = \phi_{rotation} + \phi_{shupe_1} \tag{6.1}$$

$$\phi_{total}^{-x} = -\phi_{rotation} + \phi_{shupe_1} \tag{6.2}$$

$$\phi_{total}^{+x} + \phi_{total}^{-x} = 2\phi_{shupe_1} \tag{6.3}$$

To prove this phenomenon experimentally, we used a hexadecapolar fiber coil wound by using PM fiber with 80 μm cladding and 168 μm coating diameter on a spool with an average diameter of 85 mm consisting of 48 layers in total and each layer had 80 turns of fiber as was also used in the model introduced in Chapter 5. The total length of the fiber coil was approximately 1037 m and was obtained by an optical time domain reflectometer (OTDR) measurement (YOKOGAWA AQ7270). We constructed an IFOG by splicing a three-in-one homemade multifunctional integrated optic chip (MIOC) fabricated with annealed proton exchange (APE) method to the fiber coil that was also spliced to a homemade broadband ASE light source with a central wavelength of 1537 nm coupled to a 3-dB optical coupler. APE-MIOC was acting as a >40-dB polarizer, a 3-dB coupler and a phase modulator. Once the loop was completed, we implemented a photodetector to the system to convert the interfered optical signal. We packed and placed only the fiber coil with a temperature sensor in a magnetic shield to prevent nonreciprocal errors coming from magnetic field changes.

The photograph of the experimental setup is given in Figure 5.7.

6.4 Experiments with a Hexadecapolar Fiber Coil

The experiments started with 0.2°C/min temperature change with an IFOG built with an hexadecapolar fiber coil. First, we ran the test while the fiber coil was horizontally placed in the +x axis over different temperatures in the climatic chamber. The rotation rate of Earth was measured as +9.6°/h in Ankara, Turkey via the constructed IFOG with horizontally placed fiber coil. The rate data were read with the aid of software by using a closed-loop modulation technique and presented as a function of temperature assessed between -40°C and +60°C operating temperature in the chamber with a 0.2°C/min. rate of temperature change. The experimental data is presented in Figure 6.1. As can be seen from the graph, the rate here is cumulatively obtained by the addition of the Earth rotation which is measured positive due to the change in the placement of the fiber coil in +x direction and the Shupe effect.

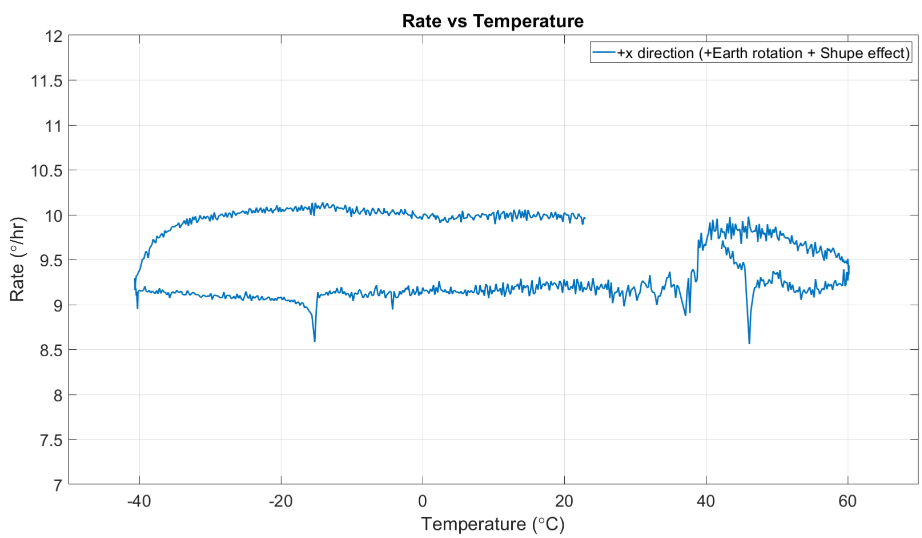

Figure 6.1: Rate vs. temperature graph of the IFOG comprising the fiber coil with the hexadecapole pattern obtained at a rate of 0.2°C/min temperature change horizontally placed in the +x direction.

The rotation rate of Earth was measured as +9.6°/h in Ankara, Turkey via the constructed IFOG with horizontally placed fiber coil and -9.6°/h via the constructed IFOG with horizontally reversed placed fiber coil. The rate data were read with the aid of software by using a closed-loop modulation technique and presented as a function of temperature assessed between -40°C and +60°C operating temperature in the chamber with a 0.2°C/min. rate of temperature change.

Then, we horizontally reversed the fiber coil and repeated the same test at the same rate of temperature change and in the same temperature range. The rotation rate of Earth was measured as -9.6°/h in Ankara, Turkey via the constructed IFOG with horizontally reversed placed fiber coil. The experimental data obtaned with this experiment is presented in Figure 6.2. As can be seen from the graph, the rate is here cumulatively obtained by the addition of the Earth rotation which is measured negative due to the horizontally reversed placed fiber coil in the -x direction and the Shupe effect.

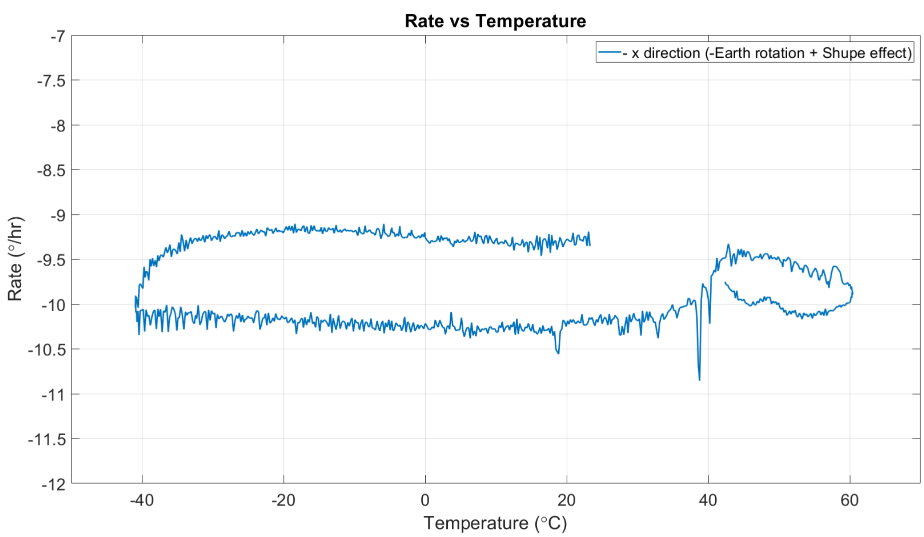

Figure 6.2: Rate vs. temperature graph of the IFOG comprising the fiber coil with the hexadecapole pattern obtained at a rate of 0.2°C/min temperature change horizontally reversed placed in the -x direction.

After completing the experiments in both +x and -x directions, we can easily calculate the total phase shift of the same IFOG relatively. The graph of the total phase shift of the related IFOG in both directions is given in Figure 6.3.

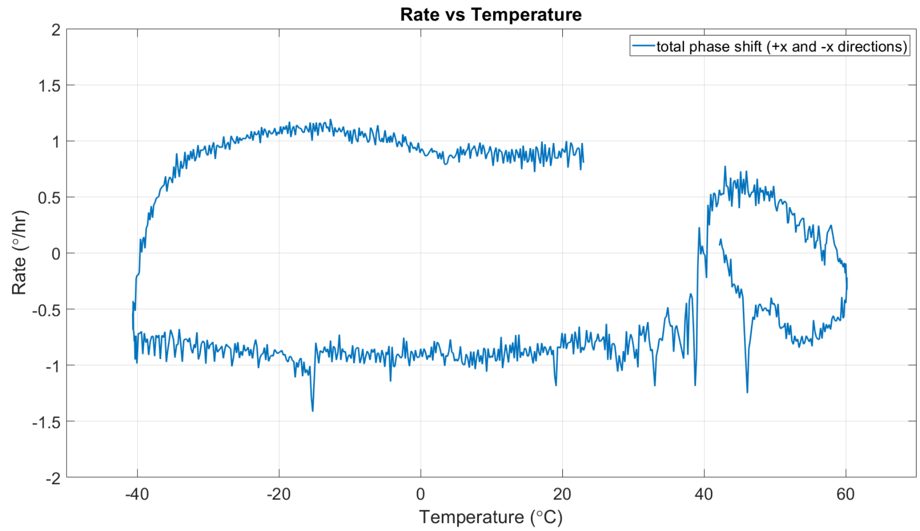

Figure 6.3: Total phase shift of the same IFOG in both directions.

To compare the rate errors due to the Shupe effect, the Earth rotation is subtracted from the real rates in both directions. Compensated absolute rate error in +x direction obtained from the IFOG at a rate of 0.2°C/min temperature change is given in Figure 6.4. Compensated absolute rate error in -x direction obtained from the IFOG at a rate of 0.2°C/min temperature change is given in Figure 6.5. In order to better see it, these two compensated results are compared with the result obtained from the IFOG comprising a perfectly trimmed hexadecapolar fiber coil of which result is provided in Figure 6.6.

Therefore, the compensated absolute rate errors that are reduced to $\pm 0.05^{\circ}/\mathrm{h}$ are presented with the result obtained from the IFOG comprising a perfectly trimmed hexadecapolar fiber coil in Figure 6.7. The comparison between these three results shows good agreement with each other.

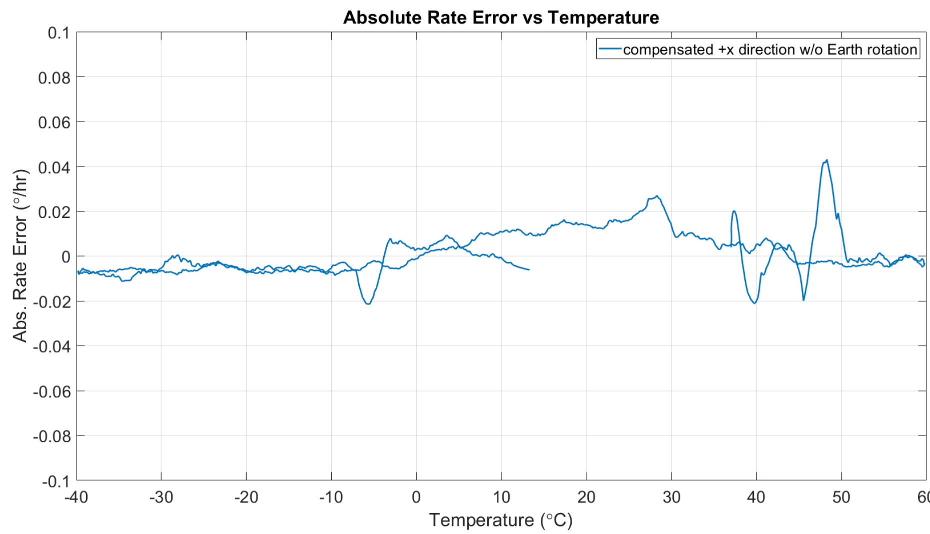

Figure 6.4: Compensated absolute rate errors the +x direction obtained from the IFOG at a rate of 0.2°C/min temperature change.

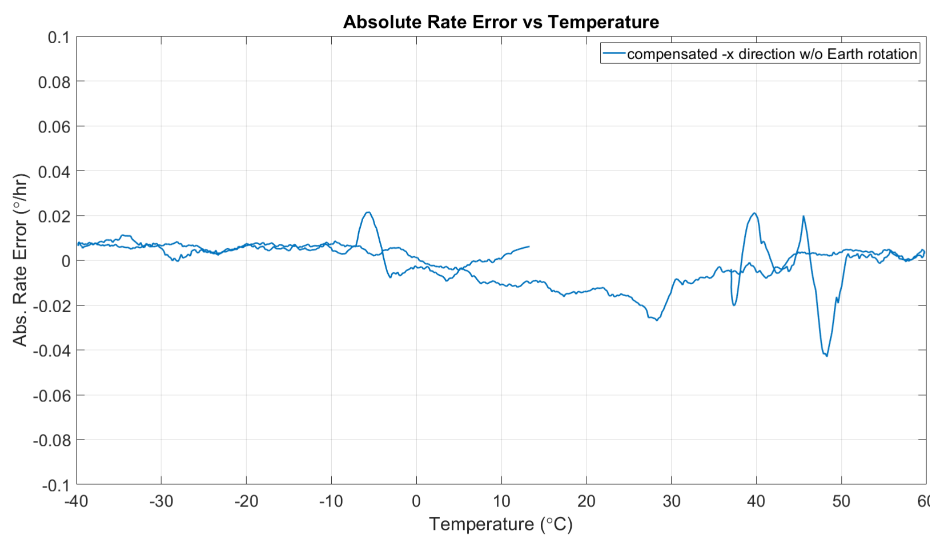

Figure 6.5: Compensated absolute rate errors the -x direction obtained from the IFOG at a rate of 0.2°C/min temperature change.

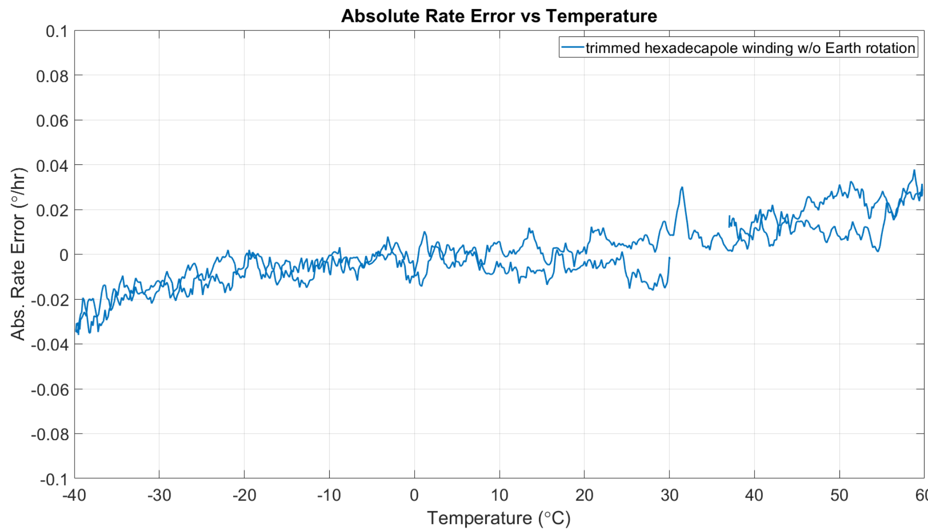

Figure 6.6: Absolute rate error obtained from the IFOG comprising a perfectly trimmed hexadecapolar fiber coil at a rate of 0.2°C/min temperature change.

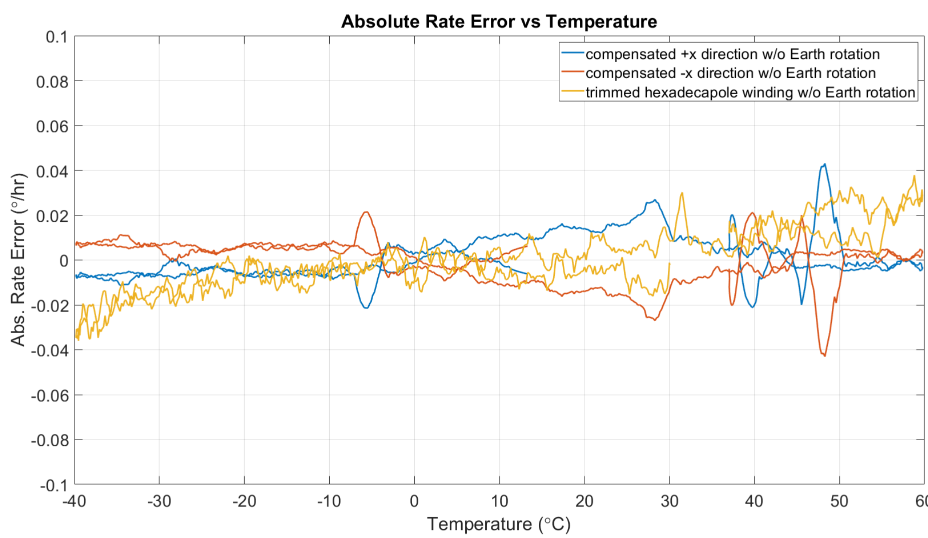

Figure 6.7: Compensated absolute rate errors in both directions compared with the result obtained from the IFOG comprising a perfectly trimmed hexadecapolar fiber coil at a rate of 0.2°C/min temperature change.

6.5 Experiments with Two Different Hexadecapolar Fiber Coils in Reverse Directions

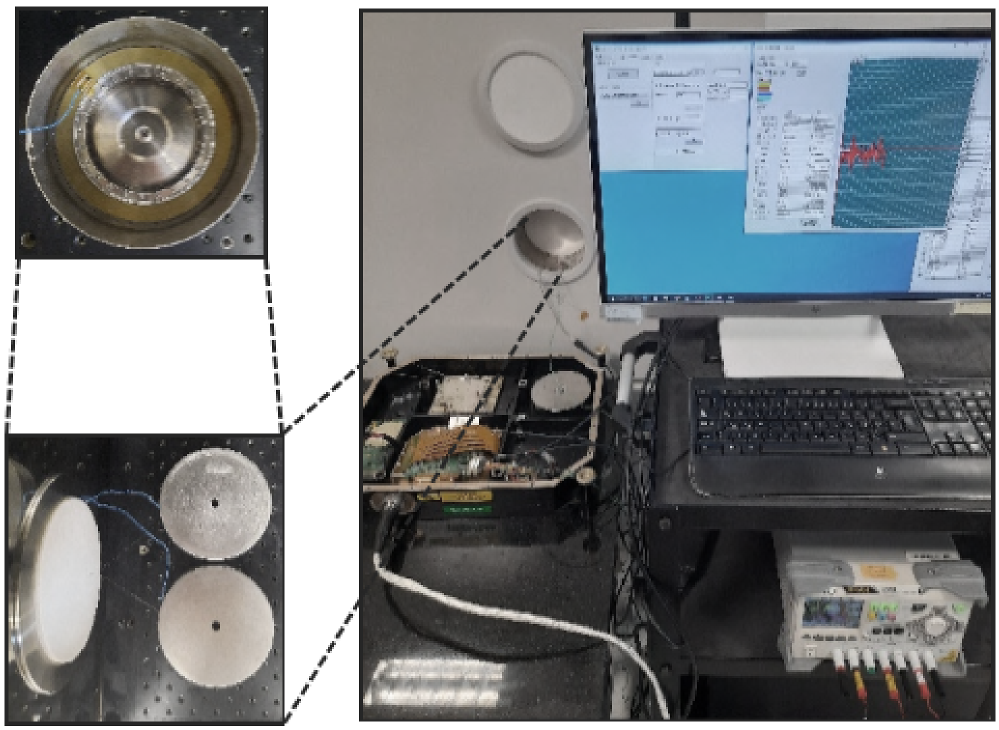

Figure 6.8: Photograph of the experimental setup.

In IFOG systems, it is not possible to simultaneously reverse the fiber coil axis horizontally. Therefore, a separate setup has been prepared to see if the presented phenomenon will still be valid when two different fiber coils, one of which is horizontally reversed, are used in the setup, as shown in Figure 6.8 and similarly as explained herein above. Then, the equations turn to:

$$\phi^{+x}_{totalC1} = \phi_{rotation} + \phi_{shupe_{C1}} \tag{6.4}$$

$$\phi^{-x}_{totalC2} = -\phi_{rotation} + \phi_{shupe_{C2}} \tag{6.5}$$

$$R_{C1,C2} = \phi_{shupe_{C1}} / \phi_{shupe_{C2}} \tag{6.6}$$

$$\phi^{+x}_{totalC1} + \phi^{-x}_{totalC2} = \phi_{shupe_{C1}} + \phi_{shupe_{C2}} \tag{6.7}$$

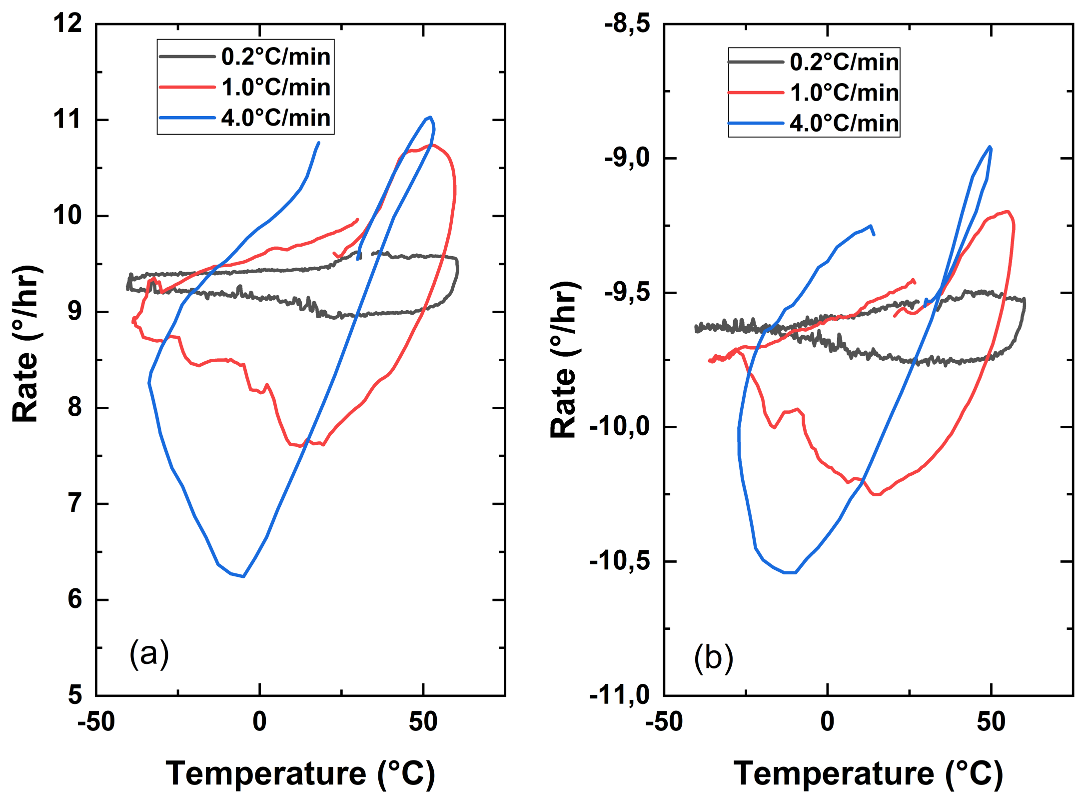

Figure 6.9: Rate vs. temperature graphs of the IFOGs comprising (a) the horizontally placed hexadecapolar fiber coil, (b) horizontally reversed placed hexadecapolar fiber coil at the rates of 0.2°C/min., 1°C/min., and 4°C/min. temperature change.

If the real rotation $\phi_{rotation}$ is known, the ratio $R_{C1,C2}$ between ϕ_{shupe_1} and ϕ_{shupe_2} can be easily found by using Eqs. (6.4), (6.5), (6.6). Here, two different IFOGs comprising hexadecapolar fiber coils were tested at 0.2°C/min., 1°C/min., and 4°C/min. rates of temperature change and the ratio $R_{C1,C2}$ is found to be 3.015, 3.003, and 3.024, respectively for each rate of temperature change, under the Earth rotation. This proves that the ratio of $R_{C1,C2}$ is constant for any rate of temperature change, even if two different fiber coils are used. The data obtained from the reverse axis are provided in Figure 6.9.

The uncompensated absolute rate errors are presented for one of the two different hexadecapolar fiber coils at 0.2°C/min. rate of temperature in Figure 6.10 and the compensated absolute rate error of the same IFOG is given in Figure 6.11. The comparison of the these two data is represented in Figure 6.12.

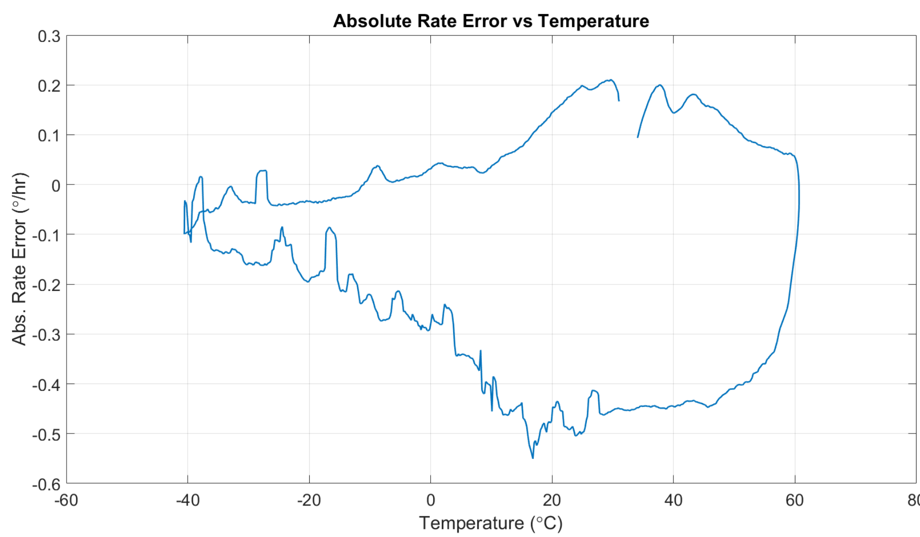

Figure 6.10: Absolute rate errors of the IFOG comprising the hexadecapolar fiber coil obtained at a rate of 0.2°C/min. temperature change.

The uncompensated absolute rate errors are presented for one of the two different hexadecapolar fiber coils at 1°C/min. rate of temperature in Figure 6.13 and the compensated absolute rate error of the same IFOG is given in Figure 6.14. The comparison of the these two data is represented in Figure 6.15.

The uncompensated absolute rate errors are presented for one of the two different

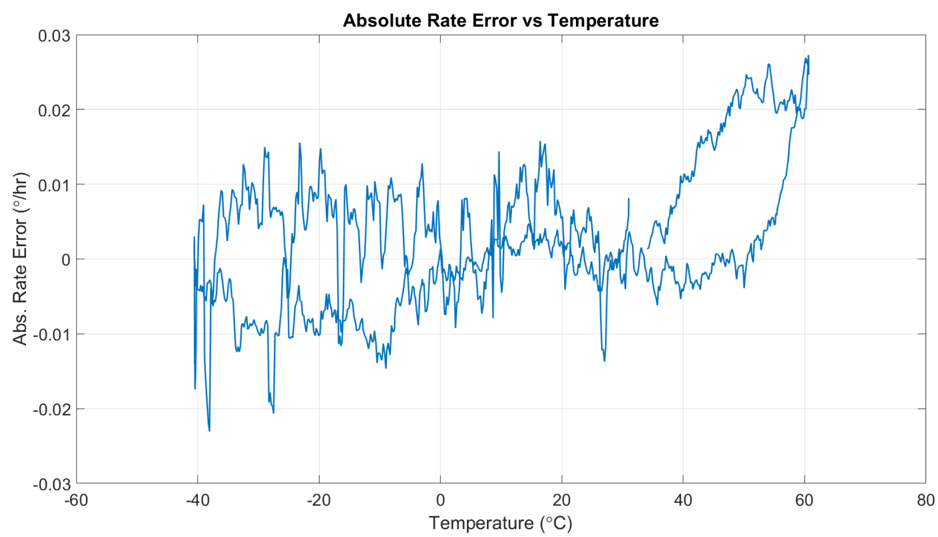

Figure 6.11: Compensated absolute rate error of the hexadecapolar fiber coil at a rate of a 0.2°C/min. temperature change.

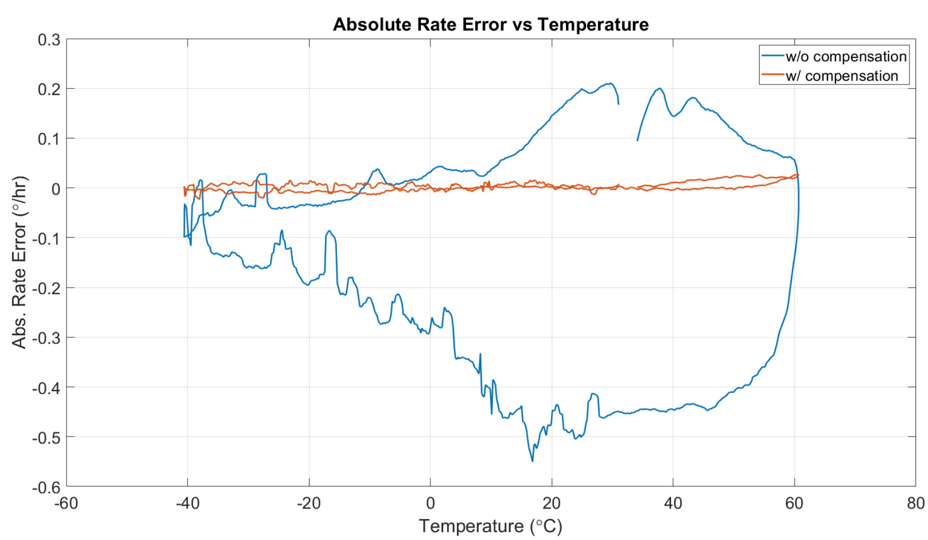

Figure 6.12: Comparison of the uncompensated and compensated absolute rate error of the hexadecapolar fiber coil at a rate of a 0.2°C/min. temperature change.

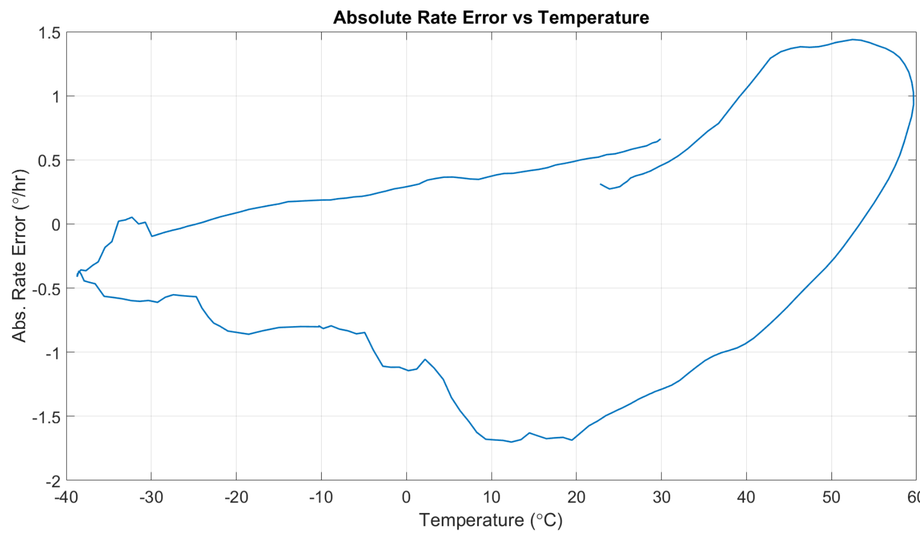

Figure 6.13: Absolute rate errors of the IFOG comprising the hexadecapolar fiber coil obtained at a rate of 1°C/min. temperature change.

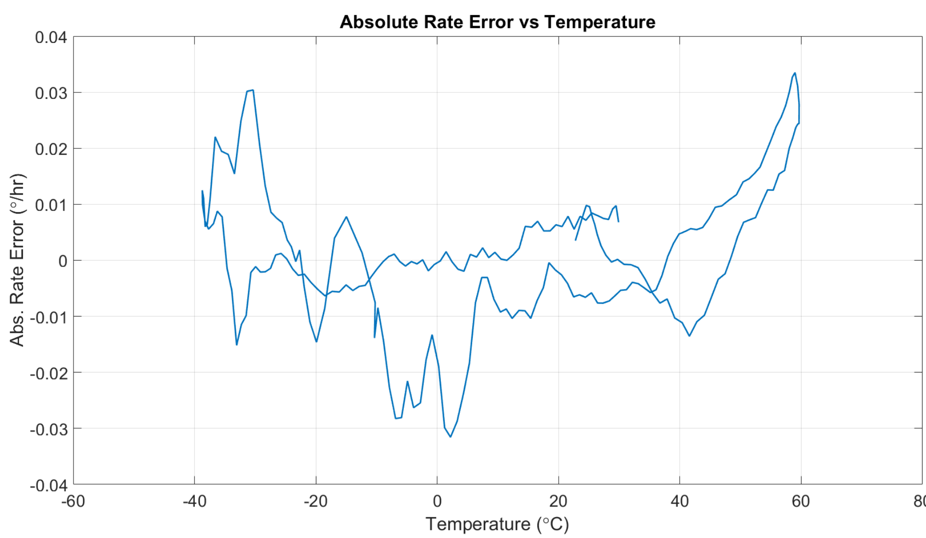

Figure 6.14: Compensated absolute rate error of the hexadecapolar fiber coil at a rate of a 1°C/min. temperature change.

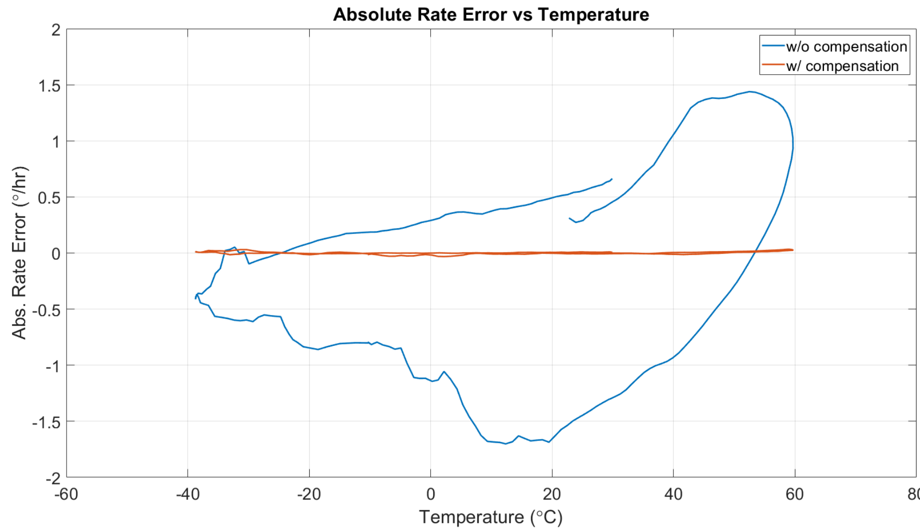

Figure 6.15: Comparison of the uncompensated and compensated absolute rate error of the hexadecapolar fiber coil at a rate of a 1°C/min. temperature change.

hexadecapolar fiber coils at 4°C/min. rate of temperature in Figure 6.16 and the compensated absolute rate error of the same IFOG is given in Figure 6.17. The comparison of the these two data is represented in Figure 6.18.

The comparison of the uncompensated absolute rate errors of the hexadecapolar fiber coil at the rates of 0.2°C/min., 1°C/min., and 4°C/min. temperature change is given in Figure 6.19.

The comparison of the compensated absolute rate errors of the hexadecapolar fiber coil at the rates of 0.2°C/min., 1°C/min., and 4°C/min. temperature change is given in Figure 6.20. The error rate increases with respect to the rate of temperature accordingly. However, the absolute rate error can be compensated down from $\pm 2^\circ/\mathrm{h}$ (as max. rate error) to $\pm 0.05^\circ/\mathrm{h}$ as shown in Figure 6.20 by using Eqs. (6.6), and (6.7).

The result obtained from the IFOG comprising the perfectly trimmed hexadecapolar fiber coil at a rate of a temperature change of 0.2°C/min. is also shown in Figure 6.21, and labeled as 0.2°C/min.*, for comparing the results.

The summary of the graphs are given in Figure 6.22 or the hexadecapolar fiber coil.

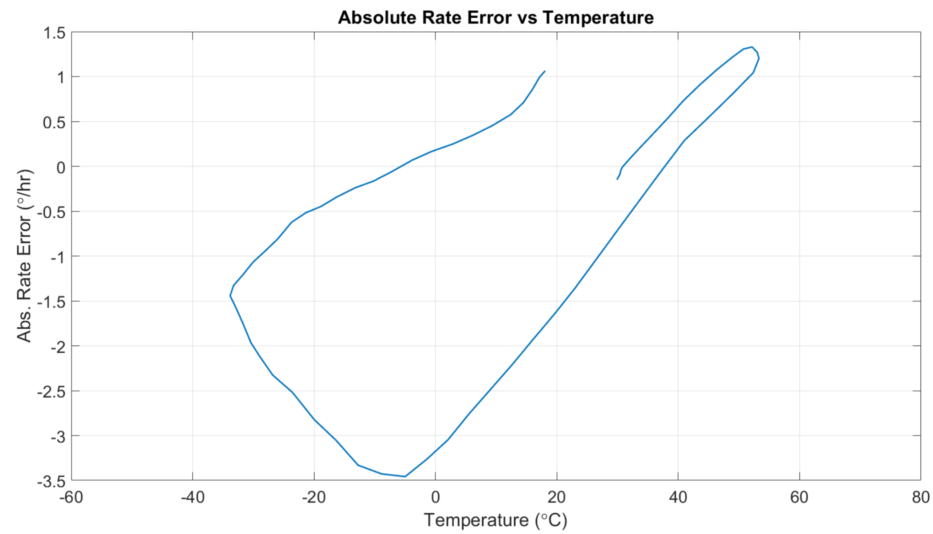

Figure 6.16: Absolute rate errors of the IFOG comprising the hexadecapolar fiber coil obtained at a rate of 4°C/min. temperature change.

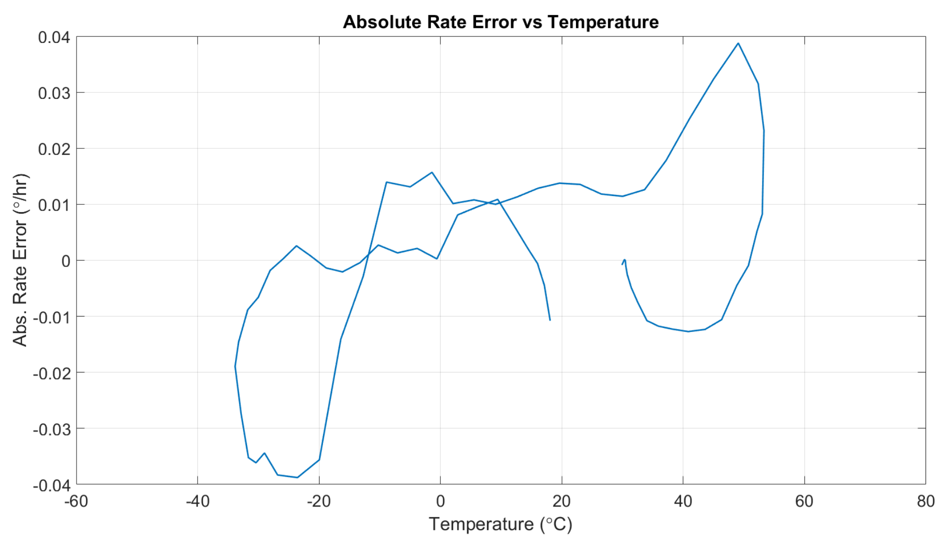

Figure 6.17: Compensated absolute rate error of the hexadecapolar fiber coil at a rate of a 4°C/min. temperature change.

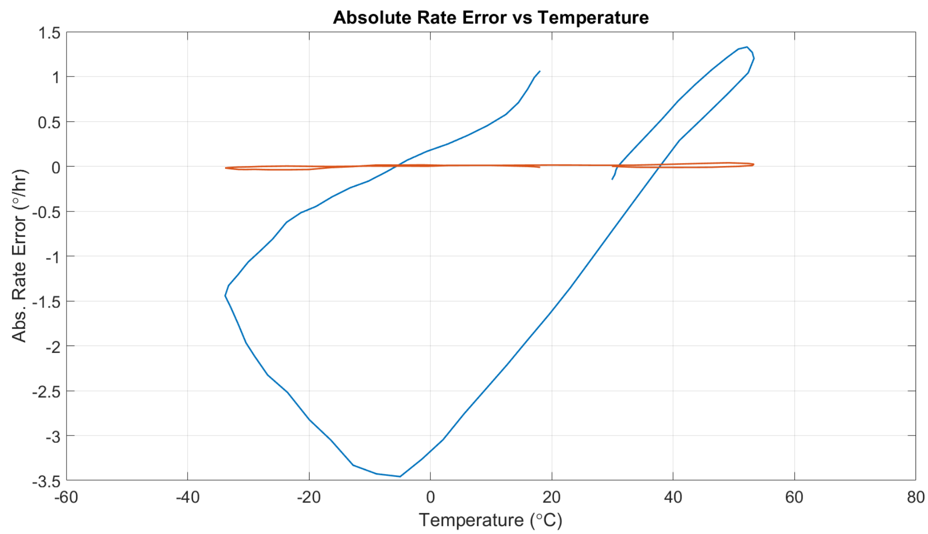

Figure 6.18: Comparison of the uncompensated and compensated absolute rate error of the hexadecapolar fiber coil at a rate of a 4°C/min. temperature change.

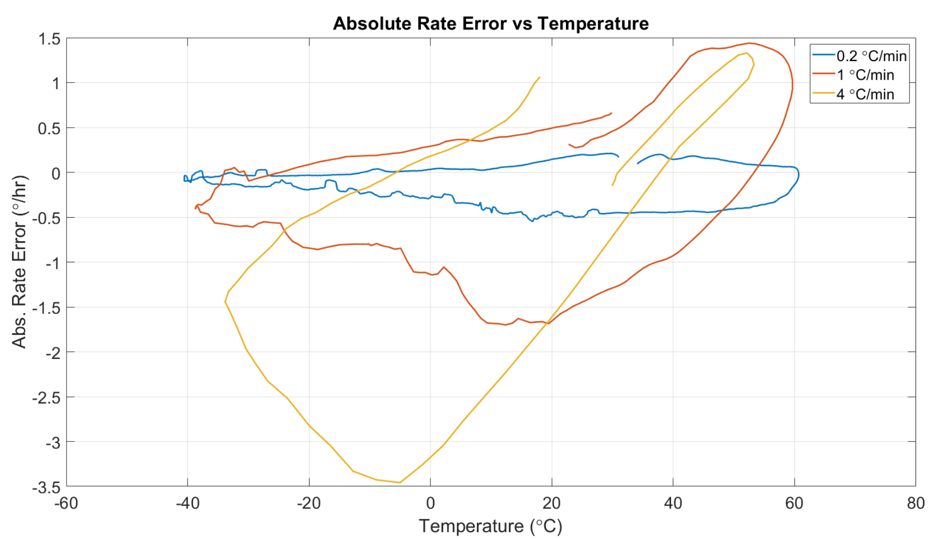

Figure 6.19: Comparison of the uncompensated absolute rate errors of the hexadecapolar fiber coil at the rates of 0.2°C/min., 1°C/min., and 4°C/min. temperature change.

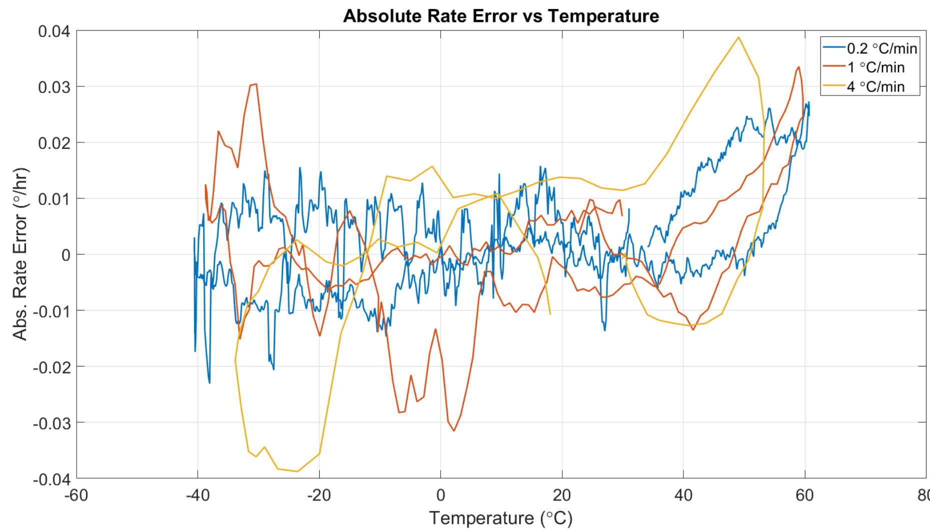

Figure 6.20: Comparison of the compensated absolute rate errors of the hexadecapolar fiber coil at the rates of 0.2°C/min., 1°C/min., and 4°C/min. temperature change.

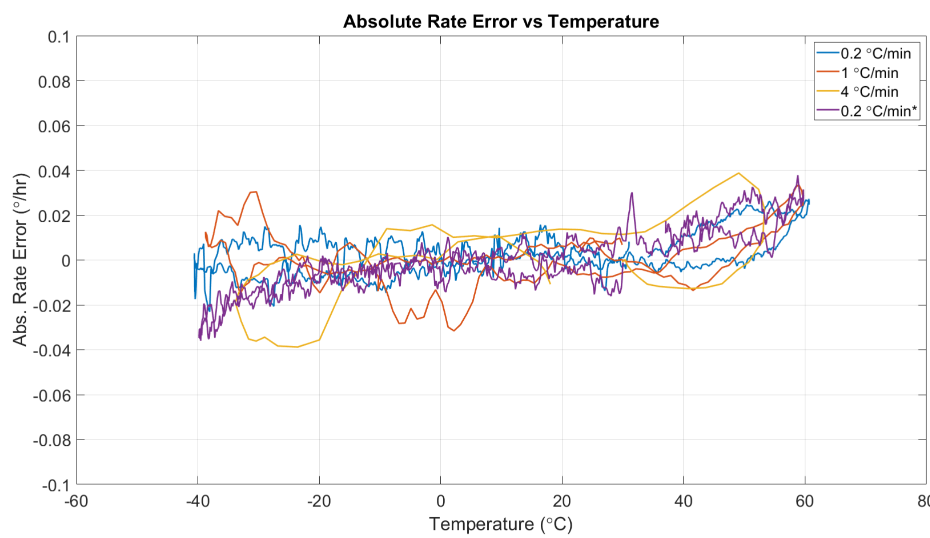

Figure 6.21: Compensated absolute rate errors of the hexadecapolar fiber coil at a rate of 0.2°C/min., 1°C/min., and 4°C/min. temperature change, respectively, compared with the result obtained from the IFOG comprising a perfectly trimmed hexadecapolar fiber coil at a rate of a 0.2°C/min. temperature change.

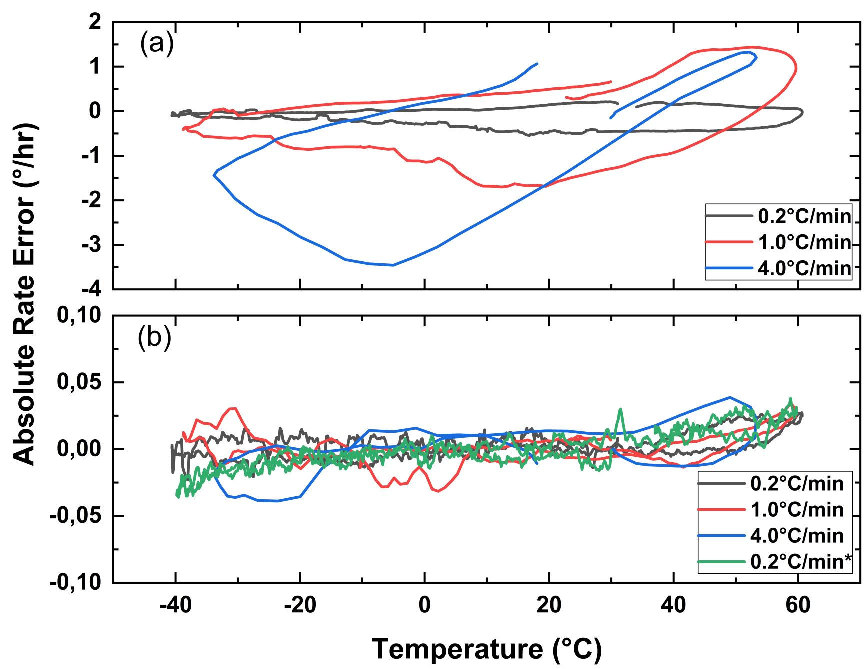

Figure 6.22: (a) Absolute rate errors of the IFOG comprising the hexadecapolar fiber coil obtained at a rate of 0.2°C/min., 1°C/min., and 4°C/min. temperature change, (b) compensated absolute rate errors of the hexadecapolar fiber coil, respectively, compared with the result obtained from the IFOG comprising a perfectly trimmed hexadecapolar fiber coil at a rate of a 0.2°C/min. temperature change.

6.6 Experiments with Hexadecapolar and Quadrupolar Fiber Coils: Elimination of the Symmetry Dependence of Fiber Coils

To prove the validity of the claim about the elimination of the symmetry dependence of the fiber coils, we used one fiber coil with a hexadecapole winding pattern from the previous setup and one different fiber coil wound with a quadrupole winding pattern that is known to be more sensitive to the Shupe effect. The ratios $R_{C1,C2}$ have also been calculated for these fiber coils and they were found to be 5.167, 5.203, and 5.189, for a 0.2°C/min., 1°C/min., and 4°C/min. rate of temperature change, respectively. The data obtained from the reverse axis are provided in Figure 6.23.

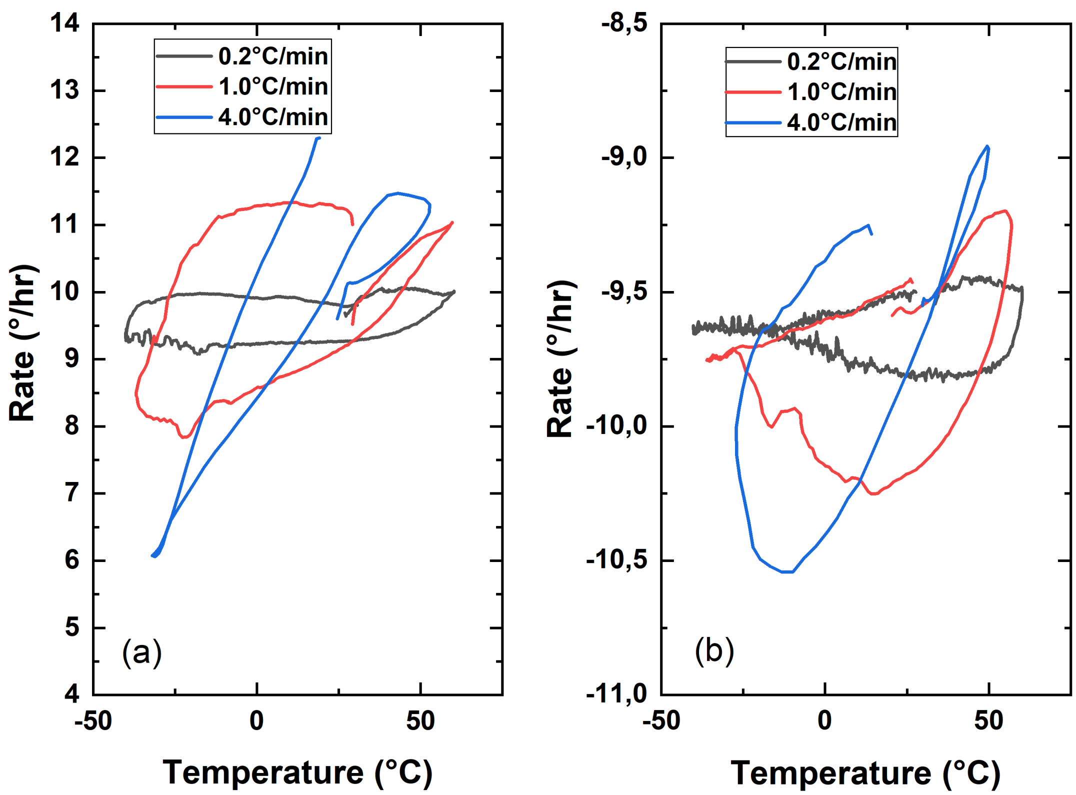

Figure 6.23: Rate vs. temperature graphs of the IFOGs comprising (a) the horizontally placed quadrupolar fiber coil, (b) horizontally reversed placed hexadecapolar fiber coil at the rates of 0.2°C/min., 1°C/min., and 4°C/min. temperature change.

The uncompensated absolute rate errors are presented for the quadrupolar fiber coil at 0.2°C/min. rate of temperature in Figure 6.24 and the compensated absolute rate error of the same IFOG is given in Figure 6.25. The comparison of the these two data is represented in Figure 6.26.

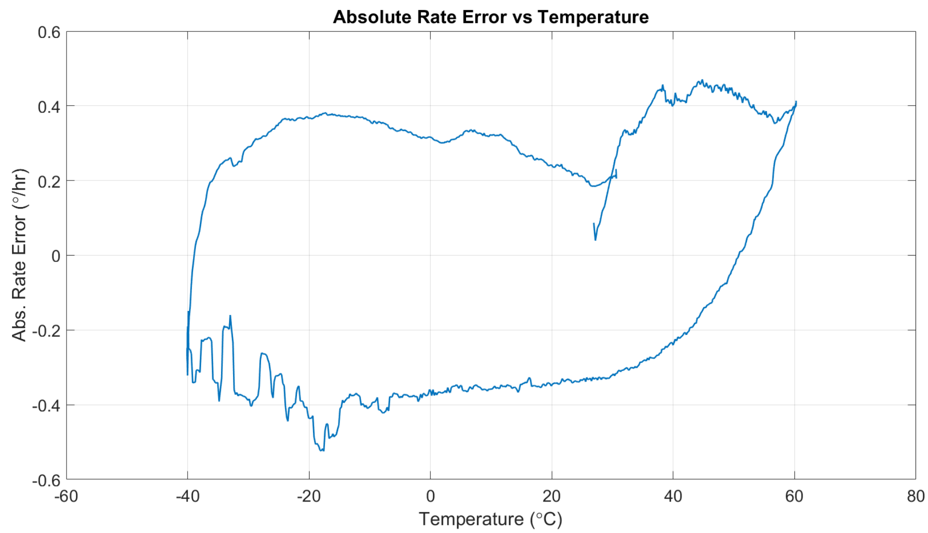

Figure 6.24: Absolute rate errors of the IFOG comprising the quadrupolar fiber coil obtained at a rate of 0.2°C/min. temperature change.

The uncompensated absolute rate errors are presented for one of the two different hexadecapolar fiber coils at 1°C/min. rate of temperature in Figure 6.27 and the compensated absolute rate error of the same IFOG is given in Figure 6.28.

The uncompensated absolute rate errors are presented for one of the two different hexadecapolar fiber coils at 4°C/min. rate of temperature in Figure 6.30 and the compensated absolute rate error of the same IFOG is given in Figure 6.31.

The comparison of the uncompensated absolute rate errors of the quadrupolar fiber coil at the rates of 0.2°C/min., 1°C/min., and 4°C/min. temperature change is given in Figure 6.34.

The comparison of the compensated absolute rate errors of the quadrupolar fiber coil at the rates of 0.2°C/min., 1°C/min., and 4°C/min. temperature change is given in Figure 6.34. The absolute rate error can be decreased from $\pm 3^\circ/\mathrm{h}$ (as max. rate error) to $\pm 0.05^\circ/\mathrm{h}$ after the compensation as shown in the same figure.

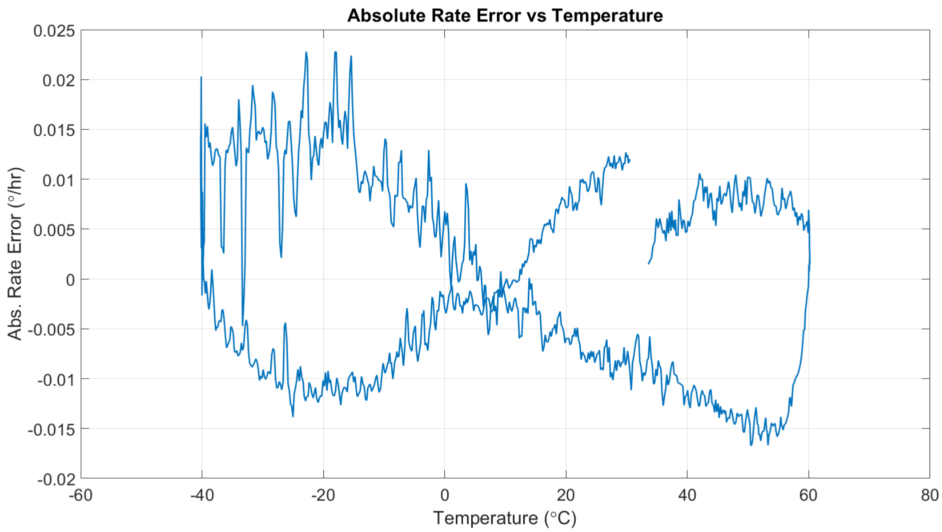

Figure 6.25: Compensated absolute rate error of the quadrupolar fiber coil at a rate of a 0.2°C/min. temperature change.

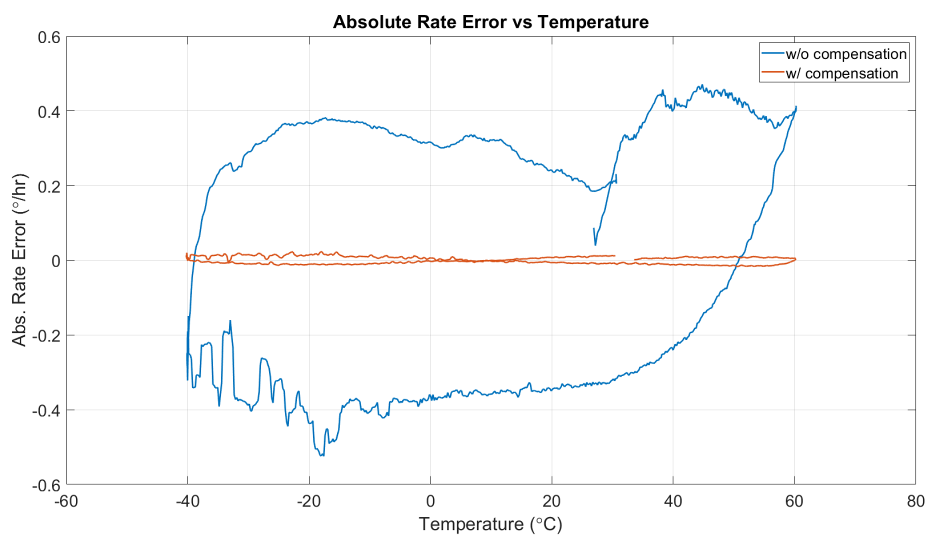

Figure 6.26: Comparison of the uncompensated and compensated absolute rate error of the quadrupolar fiber coil at a rate of a 0.2°C/min. temperature change.

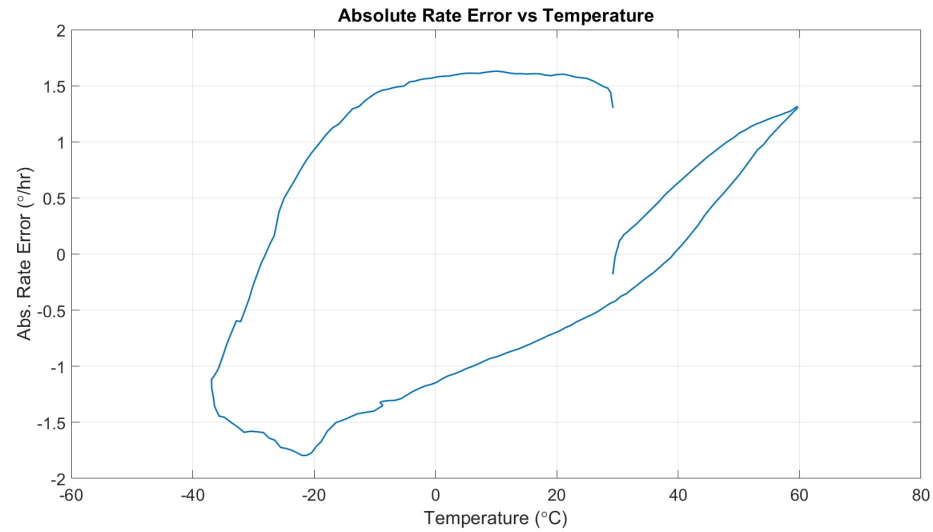

Figure 6.27: Absolute rate errors of the IFOG comprising the quadrupolar fiber coil obtained at a rate of 1°C/min. temperature change.

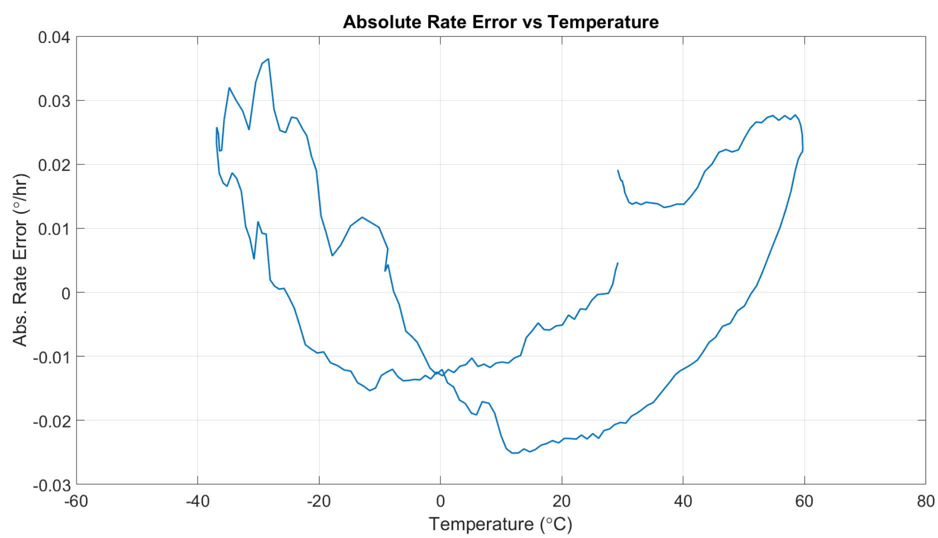

Figure 6.28: Compensated absolute rate error of the quadrupolar fiber coil at a rate of a 1°C/min. temperature change.

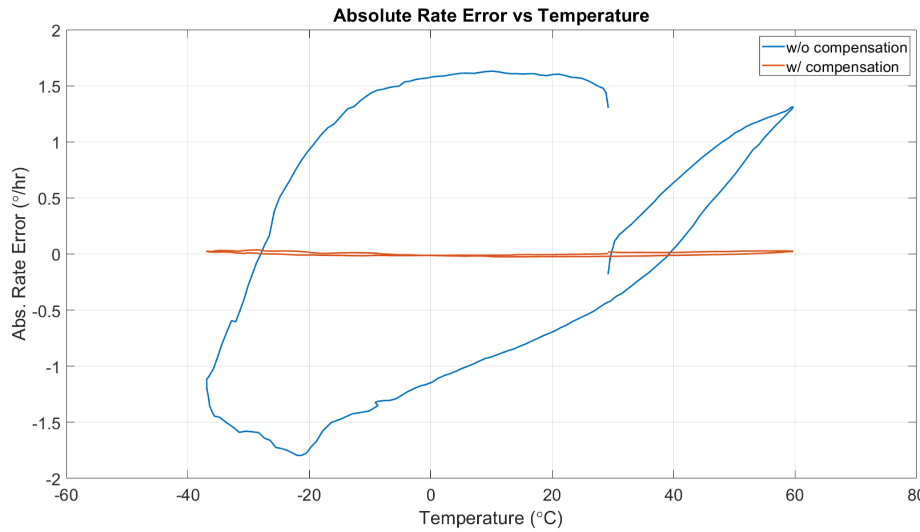

Figure 6.29: Comparison of the uncompensated and compensated absolute rate error of the quadrupolar fiber coil at a rate of a 1°C/min. temperature change.

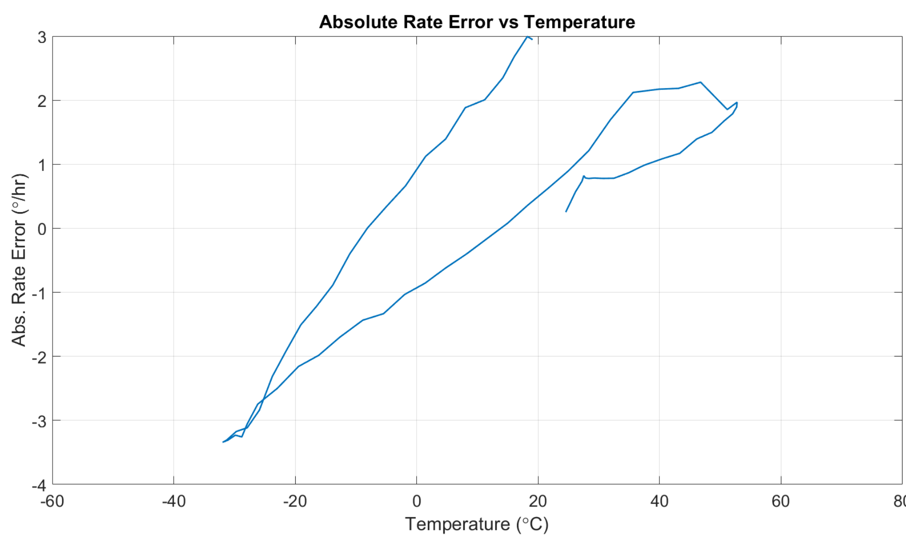

Figure 6.30: Absolute rate errors of the IFOG comprising the quadrupolar fiber coil obtained at a rate of 4°C/min. temperature change.

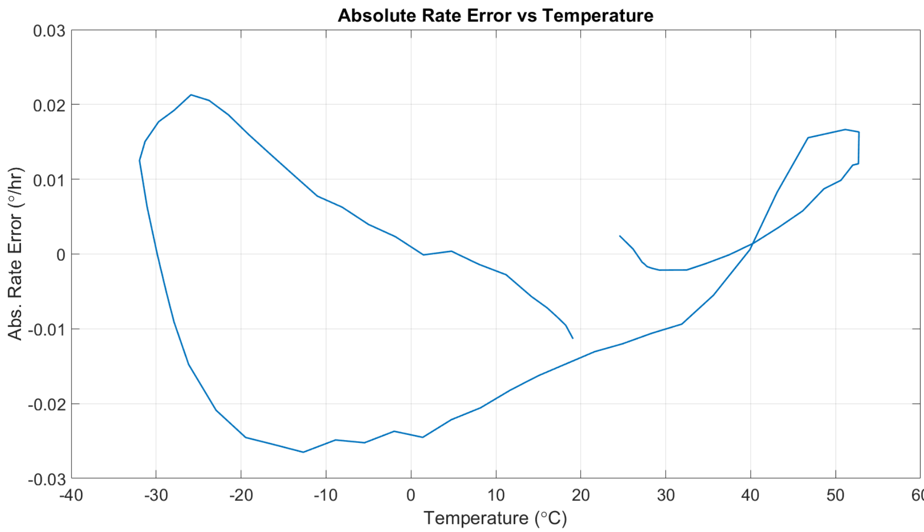

Figure 6.31: Compensated absolute rate error of the quadrupolar fiber coil at a rate of a 4°C/min. temperature change.

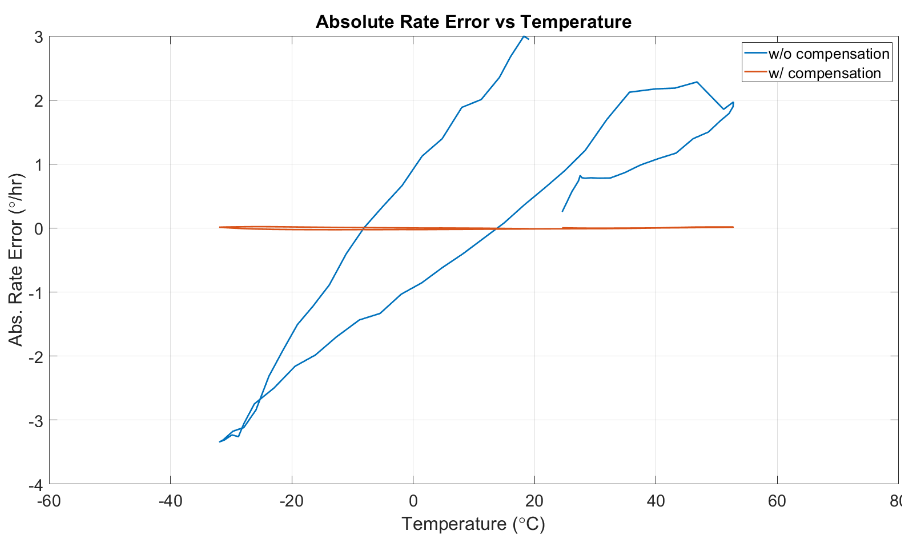

Figure 6.32: Comparison of the uncompensated and compensated absolute rate error of the quadrupolar fiber coil at a rate of a 4°C/min. temperature change.

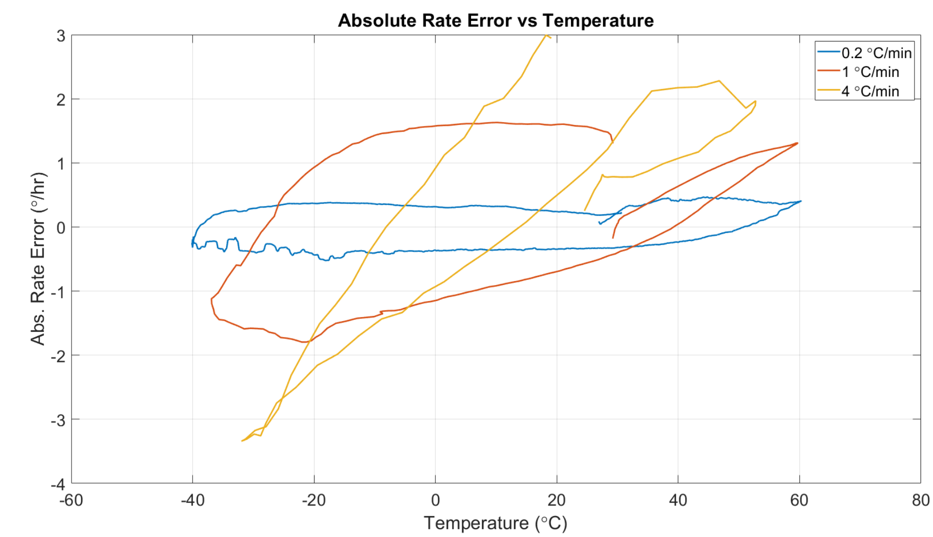

Figure 6.33: Comparison of the uncompensated absolute rate errors of the quadrupolar fiber coil at a rate of 0.2°C/min., 1°C/min., and 4°C/min. temperature change.

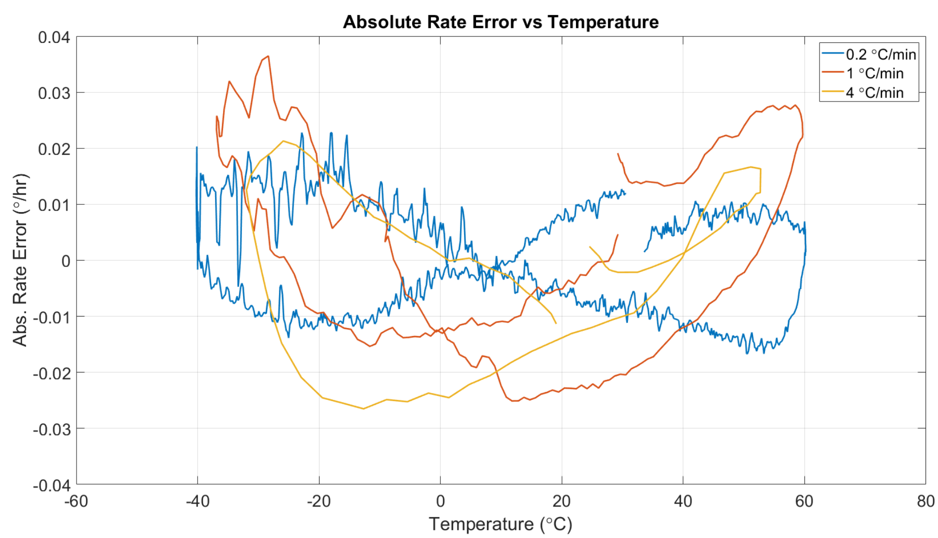

Figure 6.34: Comparison of the compensated absolute rate errors of the quadrupolar fiber coil at a rate of 0.2°C/min., 1°C/min., and 4°C/min. temperature change.

The result obtained from the IFOG comprising the perfectly trimmed hexadecapolar fiber coil at a rate of a temperature change of 0.2°C/min. is also shown in Figure 6.35, and labeled as 0.2°C/min.*, for comparing the results.

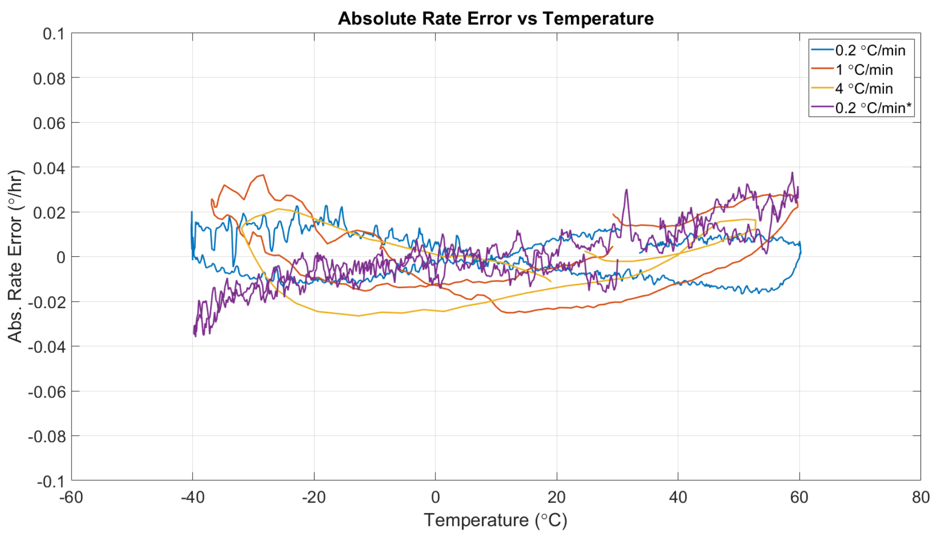

Figure 6.35: Compensated absolute rate errors of the quadrupolar fiber coil at a rate of 0.2°C/min., 1°C/min., and 4°C/min. temperature change, respectively, compared with the result obtained from the IFOG comprising a perfectly trimmed hexadecapolar fiber coil at a rate of a 0.2°C/min. temperature change.

The summary of the graphs are given in Figure 6.22 or the quadrupolar fiber coil.

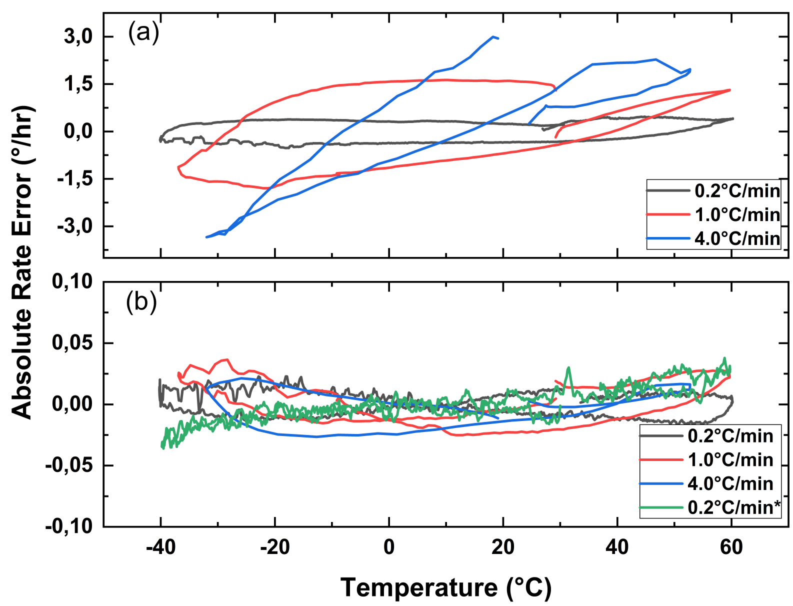

Figure 6.36: (a) Absolute rate errors of the IFOG comprising the quadrupolar fiber coil obtained at a rate of 0.2°C/min., 1°C/min., and 4°C/min. temperature change, (b) compensated absolute rate errors of the quadrupolar fiber coil, respectively, compared with the result obtained from the IFOG comprising a perfectly trimmed hexadecapolar fiber coil at a rate of a 0.2°C/min. temperature change.

6.7 Symmetry-Independent-Winding IFOG (SIW-IFOG)

Based on the agreement that we observed between the real and the compensated results, a new configuration that consists of four-axes, namely -x (as Shupe), +x, +y, and +z, is designed and a novel system called symmetry-independent-winding IFOG (SIW-IFOG) is proposed to compensate for the errors caused by the Shupe effect in Figure 6.37. The ratios for each different fiber coil pair $R_{S,X}$, $R_{S,Y}$, and $R_{S,Z}$ can be calculated by using Eqs. (6.4), (6.5), and (6.6). Then, we have a constant ratio between the real rate errors coming from the Shupe effect for each different fiber coil pair, such as:

$$R_{S,i} = \phi_{shupeS}/\phi_{shupe(i)} \tag{6.8}$$

where i represents the axes as X, Y, and Z according to the position of the gyroscope and the ratio $R_{S,i}$ is independent of the rate of temperature change as shown in Figure 6.22 and 6.36.

In the system, the ratio $R_{S,X}$ between CoilS (-x axis) and CoilX (+x axis) will be the checkpoint to calculate how much the real rate errors are coming from the Shupe effect. By adding these two total rates, -x (Eqn. (6.10)) and +x (Eqn. (6.11)), the real rotations will cancel each other out and the total real rate errors will emerge, as in Eqn. (6.12). The known ratio $R_{S,X}$ reveals the real rate errors for the +x and -x axes. In addition, when the real rate error is known for CoilS, by using the ratio for remaining axes, $R_{S,Y}$, and $R_{S,Z}$, the real rate errors can also be calculated for the y and z axes easily.

$$R_{S,X} = \phi_{shupeS}/\phi_{shupeX} \rightarrow known \tag{6.9}$$

$$\phi_{total}^{-x} = \phi_{rotation_{-x}} + \phi_{shupeS} \tag{6.10}$$

$$\phi_{total}^{+x} = \phi_{rotation_{+x}} + \phi_{shupeX} \tag{6.11}$$

$$\phi_{total}^{-x} + \phi_{total}^{+x} = \phi_{shupeS} + \phi_{shupeX} \tag{6.12}$$

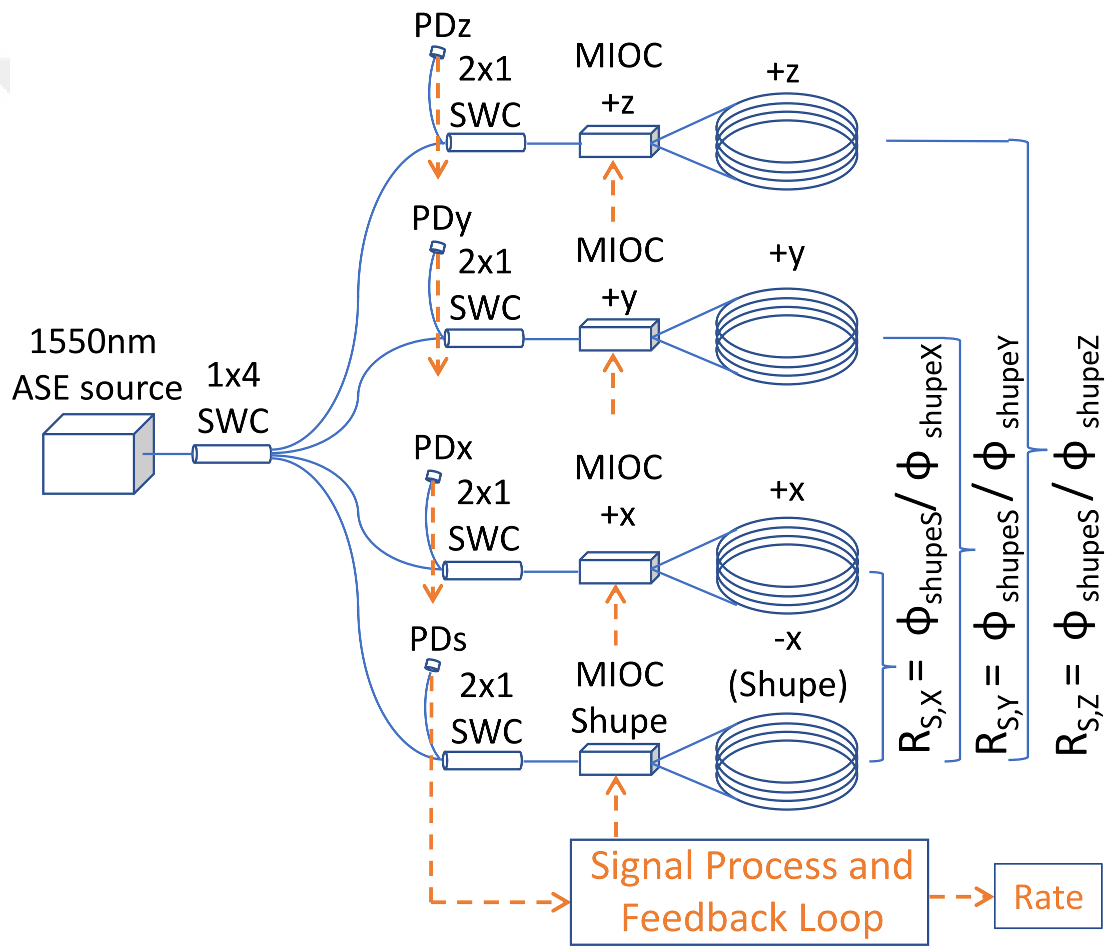

Figure 6.37: Schematics of the configuration of the symmetry-independent-winding IFOG (SIW-IFOG).

Chapter 7

Conclusion

In conclusion, starting from the studies aiming to understand the thermal effects that cause phase differences other than the Sagnac effect on different fiber coils, we experimentally showed the independence of the Shupe effect on the real rotation by simply repeating the test with a single hexadecapolar fiber coil in reverse directions. We experimentally calculated a ratio between the real rate errors of the two IFOGs comprising different hexadecapolar fiber coils with the help of the tests conducted at a different rate of temperature changes and showed that this ratio is constant for any rate of temperature change. We also reinforced our argument by repeating the test with a quadrupolar fiber coil that is known to be more sensitive to the Shupe effect in order to prove the claim about the elimination of the symmetry dependence of the fiber coil for the Shupe effect. Based on the outcomes of these studies, we proposed a novel configured complete system called SIW-IFOG that eliminates the winding symmetry dependence of the performance of the IFOGs and compensates the errors 40 times reduced for the hexadecapolar fiber coil and 60 times reduced for the quadrupolar fiber coil down to $\pm 0.05^{\circ}/\mathrm{h}$ that is caused by the Shupe effect. In future studies, the effectiveness of this new method will be examined for rate errors due to the Kerr effect as well as the Faraday effect under temperature change and vibration, which are independent of the direction of the real rotations.

Bibliography

[1] G. Sagnac, “L’éther lumineux démontré par l’effet du vent relatif d’éther dans un interféromètre en rotation uniforme,” *CR Acad. Sci.*, vol. 157, pp. 708–710, 1913.

[2] A. A. Michelson and H. G. Gale, “The effect of the earth’s rotation on the velocity of light, ii.,” *The Astrophysical Journal*, vol. 61, p. 140, 1925.

[3] A. H. Rosenthal, “Regenerative circulatory multiple-beam interferometry for the study of light-propagation effects,” *JosA*, vol. 52, no. 10, pp. 1143–1148, 1962.

[4] W. M. Macek and D. Davis Jr, “Rotation rate sensing with traveling-wave ring lasers,” *Applied Physics Letters*, vol. 2, no. 3, pp. 67–68, 1963.

[5] H. C. Lefevre, *The fiber-optic gyroscope*. Artech house, 2022.

[6] S. Ezekiel and G. E. Knausenberger, “Laser inertial rotation sensors,” tech. rep., SOCIETY OF PHOTO-OPTICAL INSTRUMENTATION ENGINEERS BELLINGHAM WA, 1978.

[7] W. Chow, J. Gea-Banacloche, L. Pedrotti, V. Sanders, W. Schleich, and M. Scully, “The ring laser gyro,” *Reviews of Modern Physics*, vol. 57, no. 1, p. 61, 1985.

[8] S. Yin, “The pennsylvania state university, university park, pennsylvania,” *Fiber Optic Sensors*, p. 177, 2002.

[9] H. C. LEFÈRE, “Fundamentals of the interferometric fiber-optic gyroscope,” *Optical review*, vol. 4, no. 1A, pp. 20–27, 1997.

[10] S. Yin, P. B. Ruffin, and T. Francis, *Fiber optic sensors*. CRC press, 2017.

[11] D. M. Shupe, "Thermally induced nonreciprocity in the fiber-optic interferometer," *Applied optics*, vol. 19, no. 5, pp. 654–655, 1980.

[12] K. Böhm, K. Petermann, and E. Weidel, "Sensitivity of a fiber-optic gyroscope to environmental magnetic fields," *Optics Letters*, vol. 7, no. 4, pp. 180–182, 1982.

[13] A. Ohno, S. Motohara, R. Usui, Y. Itoh, and K. Okada, "Development of fiber optic gyroscope with environmental ruggedness," in *Fiber Optic Gyros: 15th Anniversary Conf*, vol. 1585, pp. 82–88, SPIE, 1992.

[14] İ. F. Sağlar, "İnterferometrik fiber optik jiroskop," 2007.

[15] V. M. Passaro, A. Cuccovillo, L. Vaiani, M. De Carlo, and C. E. Campanella, "Gyroscope technology and applications: A review in the industrial perspective," *Sensors*, vol. 17, no. 10, p. 2284, 2017.

[16] H. C. Lefèvre, "The fiber-optic gyroscope, a century after sagnac's experiment: The ultimate rotation-sensing technology?," *Comptes Rendus Physique*, vol. 15, no. 10, pp. 851–858, 2014.

[17] Y. N. Korkishko, V. Fedorov, V. Prilutskii, V. G. Ponomarev, I. V. Morev, and S. M. Kostritskii, "Interferometric closed-loop fiber-optic gyroscopes," in *Third Asia Pacific Optical Sensors Conference*, vol. 8351, pp. 810–817, SPIE, 2012.

[18] A. Naji, B. A. Hamida, X. Cheng, M. A. Mahdi, S. Harun, S. Khan, W. Al-Khateeb, A. Zaidan, B. Zaidan, and H. Ahmad, "Review of erbium-doped fiber amplifier," *International Journal of the Physical Sciences*, vol. 6, no. 20, pp. 4674–4689, 2011.

[19] P. M. Becker, A. A. Olsson, and J. R. Simpson, *Erbium-doped fiber amplifiers: fundamentals and technology*. Elsevier, 1999.

[20] R. Hui and M. O'Sullivan, *Fiber-Optic Measurement Techniques*. Academic Press, 2022.

[21] E. Mejía-Beltrán, "Rare-earth doped optical fibers," *Selected topics on Optical Fiber Technology*, 2012.

[22] P. F. Wysocki, R. F. Kalman, M. J. Digonnet, and B. Y. Kim, “Comparison of 1.48-um and 980-nm pumping for er-doped superfluorescent fiber sources,” in *Fiber Laser Sources and Amplifiers III*, vol. 1581, pp. 40–58, SPIE, 1992.

[23] A. Lucero, J. Sulhoff, and J. Zyskind, “Comparison of 980-and 1480-nm-pumped amplifiers in multiwavelength systems,” in *Optical Fiber Communication Conference*, p. TuC2, Optica Publishing Group, 1995.

[24] J. Chang and M. Tan, “Experimental optimization of an erbium-doped superfluorescent fiber source for fiber optic gyroscopes,” *Journal of Semiconductors*, vol. 32, no. 10, p. 104007, 2011.

[25] J. Hecht, *Understanding lasers: an entry-level guide*. John Wiley & Sons, 2018.

[26] https://www.vpiphotonics.com/.

[27] E. Vostrikov, N. Kikilich, Y. Zalesskaya, A. Aleinik, M. Smolovik, I. Deyneka, and I. Meshkovskii, “Stabilisation of central wavelength of erbium-doped fibre source as part of high-accuracy fog,” *IET Optoelectronics*, vol. 14, no. 4, pp. 218–222, 2020.

[28] E. Vostrikov, N. Kikilich, Y. Zalesskaya, A. Aleinik, M. Smolovik, I. Deyneka, and I. Meshkovskii, “Stabilisation of central wavelength of erbium-doped fibre source as part of high-accuracy fibre optic gyroscopes,” *IET Optoelectronics*, vol. 15, no. 6, pp. 287–293, 2021.

[29] J. Chen, N. Ding, Z. Li, and W. Wang, “Enhanced environmental performance of fiber optic gyroscope by an adhesive potting technology,” *Applied Optics*, vol. 54, no. 26, pp. 7828–7834, 2015.

[30] T. Andac, “Optik fiber icin bir temizleme ve yapistirici uygulama aparati,” Turkish Patent and Trademark Office, TR201910878B, 2019.

[31] T. Andac, “Bir yapistirici uygulama aparati,” Turkish Patent and Trademark Office, TR202021883B, 2020.

[32] T. Andac, “Optik fiber icin bir yapistirici uygulama aparati,” Turkish Patent and Trademark Office, TR202021576B, 2020.

[33] T. Andac, “Fiber optik sarim icin bir makara,” Turkish Patent and Trademark Office, TR202010982B, 2020.

[34] N. J. Frigo, “Compensation of linear sources of non-reciprocity in sagnac interferometers,” in *Fiber Optic and Laser Sensors I*, vol. 412, pp. 268–271, SPIE, 1983.

[35] Z. Zhang and F. Yu, “Quantitative analysis for the effect of the thermal physical property parameter of adhesive on the thermal performance of the quadrupolar fiber coil,” *Optics express*, vol. 25, no. 24, pp. 30513–30525, 2017.

[36] R. P. Goettsche and R. A. Bergh, “Trimming of fiber optic winding and method of achieving same,” June 18 1996. US Patent 5,528,715.

[37] Z. Li, Z. Meng, T. Liu, and X. S. Yao, “A novel method for determining and improving the quality of a quadrupolar fiber gyro coil under temperature variations,” *Optics Express*, vol. 21, no. 2, pp. 2521–2530, 2013.

[38] M. R. Albert and G. E. Phetteplace, “Computer models for two-dimensional steady-state heat conduction,” *US Army Corps of Engineers*, 1983.

[39] J. Nayak, “Fiber-optic gyroscopes: from design to production,” *Applied Optics*, vol. 50, no. 25, pp. E152–E161, 2011.

[40] H. C. Lefèvre, “The fiber-optic gyroscope: Challenges to become the ultimate rotation-sensing technology,” *Optical Fiber Technology*, vol. 19, no. 6, pp. 828–832, 2013.

[41] H. C. Lefevre, “The fiber-optic gyroscope: actually better than the ring-laser gyroscope?,” in *OFS2012 22nd International Conference on Optical Fiber Sensors*, vol. 8421, pp. 63–70, SPIE, 2012.

[42] A. Yertutanol, Ö. Akçaalan, S. Öğüt, E. Özbay, and A. Ceylan, “Fiber-optic gyroscope for the suppression of a faraday-effect-induced bias error,” *Optics Letters*, vol. 46, no. 17, pp. 4328–4331, 2021.

[43] S. Mile, “Octupole winding pattern for a fiber optic coil,” *European Patent: 2075535A2*, 2009.

[44] M. Chomát, “Efficient suppression of thermally induced nonreciprocity in fiber-optic sagnac interferometers with novel double-layer winding,” *Applied optics*, vol. 32, no. 13, pp. 2289–2291, 1993.

[45] Y. Wang, X. Wu, B. Liu, and J. Ma, “Design and fabrication of high precision optical fiber coil based on temperature error model,” in *Optical Precision Manufacturing, Testing, and Applications*, vol. 10847, pp. 127–132, SPIE, 2018.

[46] W. Hong, X. Hu, Z. Zang, P. Zhang, S. Lou, B. Huang, Y. Li, and M. Zhang, “Accurate measurement and enhancement of fiber coil symmetry,” *Applied Optics*, vol. 62, no. 16, pp. E109–E118, 2023.

[47] Y. Zhang, Z. Gao, Y. Zhang, and L. Yang, “Method of reducing thermal-induced errors of a fiber optic gyroscope by adding additional winding layers,” *Applied Optics*, vol. 59, no. 8, pp. 2462–2467, 2020.

[48] D. He, Y. Wu, Y. Li, Z. Zhang, C. Peng, and Z. Li, “Stability improvement enabled by four-state modulation in dual-polarization fiber optic gyroscopes,” *Optics Communications*, vol. 452, pp. 68–73, 2019.

[49] Y. Chen, Y. Cao, L. Zhu, Y. He, W. Wang, H. Huang, X. Ma, and Z. Li, “Suppression of effects of temperature variation by high-order frequency modulation in large fiber-optic gyroscopes,” *Applied Physics Letters*, vol. 122, no. 14, 2023.

[50] N. Song, X. Xu, Z. Zhang, F. Gao, and X. Wang, “Advanced interferometric fiber optic gyroscope for inertial sensing: A review,” *Journal of Lightwave Technology*, 2023.